Chapter 1

ELECTRON TRANSPORT AND CONFINING POTENTIALS IN SEMICONDUCTOR NANOSTRUCTURES

J. Smoliner, G. Ploner

Institut für Festkörperelektronik und Mikrostukturzentrum der TU-Wien, Floragasse 7, A-1040 Vienna, Austria

Contents

1. INTRODUCTION

Before nanofabrication processes became available, the fundamental electronic properties of semiconductor devices were independent of their geometrical size. Through nanofab-

Handbook of Nanostructured Materials and Nanotechnology, edited by H.S. Nalwa
Volume 3: Electrical Properties

ISBN 0-12-513763-X/$30.00

rication, however, the geometrical dimensions of a semiconductor device can be made smaller than any of the other characteristic lengths of the electron system, such as the mean free path or the Fermi wavelength. Consequently, the device geometry is expected to influence the fundamental device and transport properties, which has made the investigation of the electronic properties of nanostructured systems a continuously growing field of solid-state research. Together with advances in molecular beam epitaxy (MBE) growth, nanofabrication allows for so-called "band structure engineering" in the vertical and lateral directions suitable for the design of semiconductor devices of almost any desired properties.

In the very beginning of nanofabrication, quantum wire structures were suggested to provide efficient semiconductor lasers, because the artificial confinement of carriers in the active region of a nanolaser was expected to give a better performance [1, 2] than a bulk system. After that, the electronic properties of the wires themselves and their possible use for device applications became the center of worldwide activities [3]. In 1985, Luryi and co-workers [4] were the first to report a quantum wire device with negative transconductance, and it was demonstrated that this kind of quantum device is interesting for practical applications, for example, as field effect transistors [5]. With forthcoming advances in nanotechnology, the idea of an "artificial atom" or quantum dot became realizable and a topic of great interest. As ohmic contacts to quantum dots are difficult to establish, the first investigations of quantum dots concentrated on optical properties such as size effects in the absorption spectra [6] and the exciton dynamics [7]. Later tunneling spectroscopy [8, 9] was established as the genuine method for the investigation of the electronic transport properties of quantum dot structures [10].

After the presence of size quantization effects and quantum interference phenomena in wires and dots was demonstrated in the early experiments, further investigations revealed numerous other features that were partially not predicted by theoretical considerations, such as the quantized conductance in ballistic quantum wires [11, 12] or the quenching of the quantum Hall effect in strong magnetic fields [13, 14].

An artificially imposed lateral potential modulation is expected to induce a miniband structure similar to that obtained by MBE-grown perpendicular superlattices. Lateral surface superlattices (LSSLs) provide the possibility of creating artificial crystals made of quantum dot "atoms." Because the electron mean free path in these LSSLs extends over many periods, they are expected to reveal interesting quantum or band structure effects that are not accessible in conventional crystal lattices [15]. In particular, the evolution of the band structure in magnetic fields is expected to display several interesting features [16]. Indeed, the experiments performed on one-dimensional (1D) and two-dimensional (2D) LSSLs in a perpendicular magnetic field revealed a wealth of additional structure in the magnetoresistance, which has been shown, however, to be due to a geometrical commensurability between the electron's cyclotron orbit and the periodic potential landscape [17–21]. For details on these so-called (magnetic) *commensurability oscillations*, see Section 5.

LSSLs were also investigated by tunneling experiments using a coupled quantum well system and equilibrium tunneling spectroscopy [22] (see Section 6). Tunneling spectroscopy principally offers the interesting possibility of studying electron transfer between systems of different dimensionality, for example, using a 2D gas as the emitter and a system of quantum wires [23] or dots [24] as the collector electrode. The tunneling characteristics give rather direct information on the Fourier transforms of the low-dimensional electron wave functions. Moreover, it turns out that the results obtained in the simulation of tunneling spectra are very sensitive to the actual shape of the potential, which brings us to the main motivation for writing this review.

1.1. Aim of This Review

While writing this chapter, it became clear that the lack of space and time as well as the huge amount of material published in the field of nanostructured systems makes it necessary to restrict the material presented here to several characteristic topics, selected with

regard to a few guiding aspects. The main emphasis in this chapter will be put on the role of the confining potential in low-dimensional systems. We will discuss the extent to which the confinement potential has a direct influence on the obtained results of lateral and vertical transport experiments, which serve as standard characterization methods for nanostructures. It will be shown how the different transport methods can be used to obtain a consistent picture of the shape and magnitude of confinement potentials and related parameters. Furthermore, in writing this review, we wanted to give the beginning experimentalist in the field some basic idea of the phenomena typically encountered in a transport investigation of low-dimensional systems and how the observed features will allow him or her to estimate the various sample parameters necessary for a detailed knowledge of the systems under investigation.

From the preceding discussion, it is clear that the present review will be far from giving a complete overview on all the transport investigations performed on nanostructured systems in the past decade. As a major omission, we only mention the transport experiments in the ballistic regime. One reason for this is the fact that the topics of interest in the ballistic regime have only marginally to do with the major guiding aspect of this review, that is, the confinement potential and its direct influence on various transport properties. Another reason is, of course, that this transport regime has been extensively reviewed previously (see, e.g., the excellent review articles by Beenakker and van Houten [25, 26], covering the developments up to the year 1991) and that an in-depth account of the recent progress in this field deserves a review of its own.

We would just like to mention some of the outstanding experimental achievements in this field, such as the study of the phase correlation behavior of electronic matter waves in semiconductor devices by ballistic transport experiments [27, 28]. Some other highlights include a modification of Young's double-slit experiment for ballistic electrons [29], as well as the experimental proof that lateral tunneling through a quantum dot is at least a partially coherent process [30], which was achieved with an extremely sophisticated device structure. Until very recently, the observation of ballistic transport phenomena was possible only in very short and narrow constrictions, the so-called quantum point contacts. Recent progress in the fabrication techniques of quantum wires and dots such as, for example, cleaved edge overgrowth [31, 32], however, has made it possible to create long conducting channels exhibiting the phenomena characteristic of ballistic transport [33, 34]. This allows an experimental test of several theoretical predictions on the behavior of one-dimensional systems of interacting electrons (Luttinger liquid state) [35, 36]. Considerable progress has also been made in adapting suitable fabrication processes for narrow channels on very high mobility 2D electron gases at relatively large distances below the sample surface [34, 37]. This led to the first experimental evidence of specifically one-dimensional electron–electron interaction effects such as a theoretically predicted [38] zero-field spin polarization in short and narrow constrictions [39].

We also do not discuss fabrication techniques in great detail. This is partly due to the fact that the complexity of the transport investigations makes highly specialized solutions necessary. Almost any new fundamental experiment uses innovations and improvements especially conceived for its special purposes. The very fundamental fabrication principles in the nanotechnology of low-dimensional systems, however, were already reviewed earlier. Some basic references on these topics can be found in [25, 40, 72] and, of course, the literature cited therein.

This chapter is divided into three main parts. In the first part (Sections 2 and 3), a survey of the basic electronic properties of low-dimensional systems is given, including the discussion of some simple numerical methods for self-consistent calculations in one and two dimensions. The second part (Sections 4 and 5) mainly deals with magnetotransport in quantum wires and lateral surface superlattices with an emphasis on the experimental determination of fundamental wire parameters and on methods to gain information on the actual shape of the confining potential. The third part (Sections 6 and 7) is dedicated to

tunneling phenomena in low-dimensional systems. The systems and experiments reviewed in this last part are also selected under the aspect to which extent they allow access to potential parameters and/or the shape of the corresponding wave functions. Because in the theoretical apparatus underlying the analysis of tunneling phenomena the notation is not as unified in the literature as in the conventional magnetotransport sector, we decided to use the same notation as in the original articles in all cases where model calculations are discussed. This makes the description of the formalism somewhat incoherent but facilitates the direct reference to the cited articles.

2. QUANTIZED STATES IN LOW-DIMENSIONAL SYSTEMS

Low-dimensional electron systems are commonly defined by lateral potentials artificially imposed on the two-dimensional electron gas (2DEG) situated at the interface of a modulation-doped semiconductor heterostructure. Throughout this chapter, we shall focus on results obtained using the GaAs–AlGaAs system. Several methods exist to create a lateral modulation of the effective potential at the heterointerface, which all use advanced lithographic or crystal growing techniques. For details of nanostructure fabrication and nanolithographic techniques, see [25, 40, 41] and the references cited therein.

The common starting point in the study of the electronic properties of low-dimensional systems is provided by confining the electrons of a 2DEG into narrow electron lines through an additional nanofabrication process. In case the lines are sufficiently narrow, lateral size quantization effects will occur and quasi one-dimensional electron systems, so-called quantum wires, are established. A typical quantum wire sample, fabricated by laser holography and subsequent wet chemical etching, is shown in Figure 1.

To analyze the electronic properties of a quantum wire, we consider the electrons as independent particles moving in a confining potential $V(x, z)$. Here $V(x, z)$ describes the joint influence of the confinement in the growth (z) direction and the lateral confinement in the x direction induced by nanolithographic patterning. The latter is thought to leave only the y direction for free motion of the electrons. This one-particle point of view ignores the presence of correlations resulting from the Coulomb interaction between different electrons and summarizes the effects of electron–electron interactions by an average global contribution to the potential. The problem is often simplified further by assuming that the confining potential $V(x, z)$ can be decomposed into a sum of two independent contributions $V(x, z) = V(z) + V(x)$, where the first term is due to the confinement at the heterointerface and the second term accounts for the lateral potential modulation. It will be shown later that this treatment is not quite correct but it can be used in many situations as a good approximation to understand the results obtained in various experimental situations. This approximation also allows the separation of the motion in the growth (z) direction

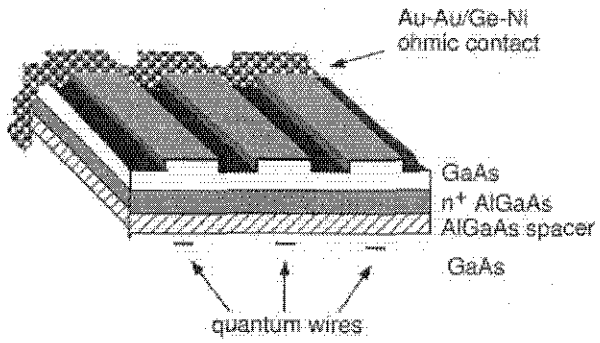

Fig. 1. Schematical view of a typical multiple quantum wire sample, which was fabricated by laser holography and subsequent wet chemical etching.

from the one-particle Schrödinger equation describing the confined electrons by a separation ansatz $\Psi(x, y, z) = \Phi(x, y)\varphi(z)$, where $\varphi(z)$ corresponds to the ground state of the underlying 2DEG with energy E_z^{2D}. Higher subbands in the z direction are not considered here, because commonly only the lowest subband is occupied in typical high-mobility GaAs–AlGaAs heterostructures. Within the effective mass approximation, this leaves us with the equation

$$H\Phi = \left(\frac{P_x^2}{2m^*} + \frac{P_y^2}{2m^*} + V(x)\right)\Phi = E^{1D}\Phi \tag{1}$$

which gives the quantized states in the quantum wire and also the corresponding energy levels. The bottom of the 2D subband E_z^{2D} is commonly taken as the zero point of the energy scale and all quantization energies are given relative to this origin.

In general, the confining potential $V(x, z)$, or $V(x)$ if the x and z dependence have been separated, has to be determined from a self-consistent solution of the Schrödinger and Poisson equations. In the following sections, we will summarize the simplest methods for such self-consistent calculations, which can be used to analyze the electronic properties of quantum wires and quantum dots. To give some insight into the physics of quantum-confined motion and to introduce several notions used in nanostructure physics, we also show how the actual confining potential can be approximated by simple and analytically tractable functions. From the self-consistent calculations, it will become evident that these approximations are often sufficient to describe the experimental data, but not always and not under all conditions.

2.1. Electrons in One-Dimensional Potentials

As stated before, we describe a one-dimensional electron system by a Schrödinger equation of the form

$$H\Phi = \left(\frac{P_x^2}{2m^*} + \frac{P_y^2}{2m^*} + V(x)\right)\Phi = E\Phi \tag{2}$$

Because the motion along the wire axis in the y direction is assumed to be free, one can use the following factorized form of the wave function:

$$\Phi(x, y) = \frac{1}{\sqrt{L}}\exp(ik_y y)\,\psi(x) \tag{3}$$

where L is the wire length. Inserting this wave function into the Schrödinger equation shows that the energy eigenvalues of the laterally confined electrons are quantized into subbands according to

$$E_n(k_y) = E_n + \frac{\hbar^2 k_y^2}{2m^*} \tag{4}$$

To determine the 1D subband energies E_n, it is necessary to know the shape of the lateral confining potential $V(x)$. There are several ways to model $V(x)$ in a more or less realistic way. The two most familiar examples for analytical model potentials are the square-well potential

$$V(x) = \begin{cases} 0 & \text{if } -W/2 \leqslant x \leqslant W/2 \\ \infty & \text{otherwise} \end{cases} \tag{5}$$

where W is the wire width, and the parabolic potential

$$V(x) = \tfrac{1}{2}m^*\omega_0^2 x^2 \tag{6}$$

It turns out [23] that these two are the limiting forms of the more general Woods–Saxon model potential, known from the shell model of atomic nuclei [42]:

$$V(x) = V_{\text{mod}}\left[\frac{1}{1+\exp\left(\frac{\alpha(w/2-x)}{w}\right)} + \frac{1}{1+\exp\left(\frac{\alpha(w/2+x)}{w}\right)}\right] - V_{\text{min}}$$
$$V_{\text{min}} = V_{\text{mod}}\left[\frac{2}{1+\exp(\alpha/2)}\right] \tag{7}$$

Depending on the parameter α, the Woods–Saxon potential interpolates between an approximately parabolic form ($\alpha = 8$) and an approximately square-well form ($\alpha = 200$). For intermediate values of α, it develops a flat bottom, which, as we shall see later, is necessary to describe quantum channels defined by a split-gate geometry at relatively high electron densities (or low gate voltages).

2.2. Parabolic Confinement

It is very instructive to consider a parabolic confinement in more detail for several reasons. First, it allows a completely analytical treatment of quantum wires in a magnetic field, and, second, it turns out that in many cases this simple model describes the actual situation reasonably well. It is, therefore, a useful tool for the analysis of magnetotransport data.

We now assume that a quantum wire is extended in the y direction and described by a lateral confining potential of the form of Eg. (6). From the beginning, we include the additional influence of a magnetic field applied in the z direction, which we describe as usual within the Landau gauge by a vector potential $\mathbf{A} = B(0, x, 0)$. The corresponding Schrödinger equation for a single electron state reads

$$-\frac{\hbar^2}{2m^*}\left[\frac{\partial^2}{\partial x^2} + \left[\frac{\partial}{\partial y} - \frac{ieB}{\hbar}x\right]^2\right]\Phi(x,y) + \frac{1}{2}m^*\omega_0^2x^2\Phi(x,y) = E\Phi(x,y) \tag{8}$$

Together with Eq. (3), using $\omega_c = eB/m^*$ for the cyclotron frequency and introducing the center coordinate $x_0 = \hbar k_y/m^*\omega_c = \hbar k_y/eB$, one obtains

$$\left[-\frac{\hbar^2}{2m^*}\frac{\partial^2}{\partial x^2} + \frac{1}{2}m^*\omega_c^2(x-x_0)^2 + \frac{1}{2}m^*\omega_0^2x^2\right]\psi(x) = E\psi(x) \tag{9}$$

A simple quadratic substitution transforms this equation into the Schrödinger equation for a shifted harmonic oscillator

$$\left[-\frac{\hbar^2}{2m^*}\frac{\partial^2}{\partial x^2} + \frac{1}{2}m^*\omega^2\left(x-\tilde{x}_0\right)^2 + \frac{\hbar^2}{2m^*}k_y^2\frac{\omega_0^2}{\omega^2}\right]\psi(x) = E\psi(x) \tag{10}$$

where we used $\omega^2 = \omega_0^2 + \omega_c^2$ and a new, magnetic field–dependent center coordinate

$$\tilde{x}_0 = x_0\frac{\omega_c^2}{\omega^2} = \frac{\hbar k_y\omega_c}{m^*\omega^2} \tag{11}$$

The solutions to this equation are the well-known harmonic oscillator functions $\psi_n(\sqrt{m\omega/\hbar}(x-\tilde{x}_0))$ with $\psi_n(x) \equiv (\sqrt{\pi}2^n n!\sqrt{m\omega/\hbar})^{-1/2}\exp(-x^2/2)\,H_n(x)$. $H_n(x)$ denotes the nth Hermite polynomial. The corresponding energy eigenvalues are given by

$$E_n(k_y) = \hbar\omega\left(n+\frac{1}{2}\right) + \frac{1}{2}\frac{\hbar^2k_y^2}{m_{\text{eff}}(B)} \qquad n = 0, 1, 2, \ldots \tag{12}$$

Here, we have used the abbreviation $m_{\text{eff}}(B) = m^*\omega^2/\omega_0^2$ for the magnetic field–dependent effective mass. In zero magnetic field, the lateral parabolic confinement gives rise to equidistant 1D subbands $E_n(k_y) = \hbar\omega_0(n+\frac{1}{2}) + \frac{1}{2}\hbar^2k_y^2/m^*$ whose dispersion is parabolic and determined by the electron effective mass m^*. In nonzero magnetic field, the subbands are still equally spaced but with a field-dependent subband spacing $\hbar\sqrt{\omega_0^2+\omega_c^2}$ and

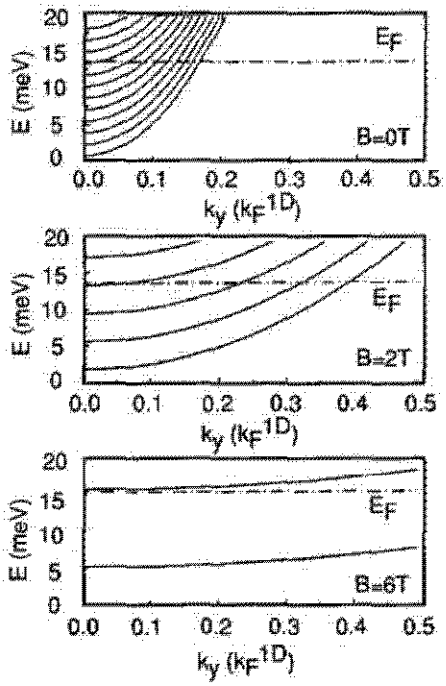

Fig. 2. Dispersion relation of a typical quantum wire plotted for three different magnetic fields.

a dispersion that becomes increasingly flat with increasing B. This behavior is due to the influence of $m_{\text{eff}}(B)$ and is illustrated in Figure 2, where the dispersion of these so-called magnetoelectric hybrid levels is drawn for three different magnetic fields.

The figure nicely visualizes that with increasing magnetic field strength, fewer and fewer subbands remain occupied for a given Fermi level E_F. This *magnetic depopulation* of 1D subbands gives rise to an oscillatory structure in the magnetoresistance. Its use for the determination of wire parameters such as the energy spacing and the electron density will be discussed later in detail.

Note the difference to the corresponding situation in purely 2D systems. In this case, the magnetic field quantizes the energy levels into *dispersionless* Landau levels at energies $\hbar\omega_c(n + \frac{1}{2})$. The group velocity of electrons in a Landau level is zero, which classically corresponds to the fact that electrons are forced on circular cyclotron orbits by the magnetic field. An analogous correspondence of the magnetoelectric hybrid states to classical orbits can be used to explain the persistence of a nonzero group velocity in a parabolic quantum wire at finite magnetic fields. As has been pointed out by Beenakker et al. [43], every point on a quantum mechanical dispersion relation can be related to a corresponding classical orbit. This is illustrated on the left-hand side of Figure 3, which shows the allowed energy values of a particle moving classically under the influence of a perpendicular magnetic field in a quantum channel described by a square-well confining potential. The (X, E) phase space shown in the figure is divided into four different sections by the two parabolas defined according to $(x_0 \pm W/2)^2 = R_c^2 = 2mE/(eB)^2$. Here, R_c is the cyclotron radius and x_0 is the center of the classical cyclotron orbit, whose quantum mechanical counterpart is the center coordinate appearing in Eqs. (10) and (11). Each section corresponds to one of the cases where the cyclotron orbit of the particle interacts with one, two, or none of the side walls. Those classical cyclotron orbits that do not interact with the wire walls correspond to undisturbed Landau levels and would be situated on completely flat sections of the dispersion relation, as shown on the right-hand side of Figure 3. Those orbits that interact with both walls (traversing orbits) correspond to magnetoelectric hybrid levels and

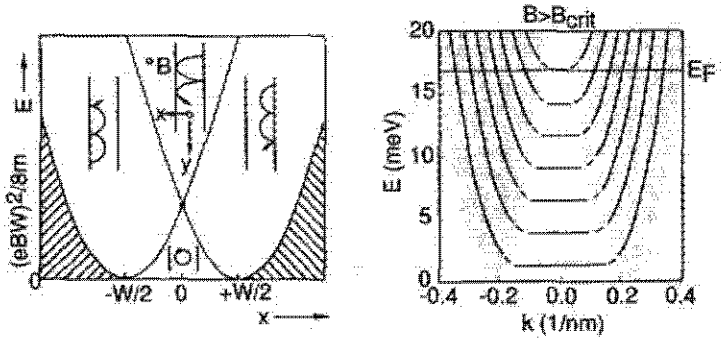

Fig. 3. Left: Possible combinations of kinetic energy and cyclotron orbit center in a narrow channel of width W, when specular boundary scattering dominates. The shaded area is forbidden. The four sections delimited by the two parabolas correspond to different types of classical orbits. Right: Dispersion relation $E(k)$ calculated for $W = 200$ nm and $B = 1.5$ T by applying the Bohr–Sommerfeld quantization condition to the classical trajectories shown on the left. The shaded areas indicate the parabolas drawn on the left-hand side of the figure. (Source: Reprinted with permission from [25].)

those orbits interacting with only one side wall of the wire (skipping orbits) correspond quantum mechanically to so-called edge states. It is clear that in each real quantum channel the dispersion relation should develop flat regions at high magnetic fields. This is when the spatial extension of the wave function, which corresponds to the classical cyclotron diameter, is substantially smaller than the effective wire width. The parabolic model potential describes this situation only in an approximate fashion since the curvature of the dispersion relation [(Eq. (12)] becomes very small at high magnetic fields but never completely flat as for a Landau level. This is due to the fact that any flat sections in the potential landscape are missing and even at very high magnetic fields there will be some net interaction of the electron orbit with the side walls of the channel.

Finally, it is interesting to note that any value X for the center coordinate of a classical cyclotron orbit (on the left-hand side of Fig. 3) corresponds directly to a particular state k_y in the dispersion relation (on the right-hand side of Fig. 3) by means of the relation $\hbar k = -eBX$. X can be interpreted as the classical equivalent to the center coordinate x_0 introduced in Eq. (9). Hence, in some sense, the dispersion relation shows the energy of a confined electron as a function of its lateral position in the wire.

3. BASIC METHODS FOR SELF-CONSISTENT CALCULATIONS IN ONE AND TWO DIMENSIONS

The model potentials described in the previous section are helpful for a qualitative and also quantitative interpretation of many experimental situations. However, as simple as they are, they need some justification from more realistic calculations taking into account an appropriately chosen distribution of impurities or the electric fields created by the gate on top of the sample. A realistic calculation should also account for the fact that, in response to the externally applied potentials, the electron gas will change its equilibrium configuration and thereby modify the effective confinement. In other words, a fully *self-consistent* treatment of the Schrödinger and Poisson equations has to be performed. From an experimentalist's point of view, such calculations will often be numerically too expensive to allow an efficient comparison with a particular experimental situation. However, these self-consistent calculations provide a lot of useful information about the corresponding sample parameters, such as the effective confinement width, the electron density, or the potential amplitude as a function of gate voltages or other external parameters. With this knowledge,

it is then possible to choose an appropriately tailored model potential that is numerically more tractable and that can be used to fit the experimental data. For this reason, some of the very basic methods for a self-consistent description of confining potentials are introduced in the following. We also reproduce some numerical results that are obtained for the most frequently encountered experimental situations.

Concerning the methodical part, we will restrict ourselves to the simple Hartree approximation and ignore all many-body corrections and scattering processes. Moreover, magnetic fields are not considered explicitly throughout this section. We disregard these topics in order to give a simple and ready-to-use exposition of the numerical and analytical details intended as a basis for quick first-principles calculations that any experimentalist might be interested in. Those readers who are interested in more theoretical details are referred to [44–47]. From more recent work, we mention [48, 49] and, in particular, the efficient numerical simulation methods of electron states in quantum wires presented by Kerkhoven et al. [50].

The organization of this section is as follows. First, we describe a simple and straightforward discretization method and some practical details of the numerical solution of the Schrödinger and Poisson equations in one dimension. Then we discuss how self-consistency is achieved numerically and how the corresponding procedure can be simplified by using the Thomas–Fermi approximation. The latter takes the electron response to an external potential into account without referring to an explicit solution of the Schrödinger equation. Finally, a simple way to solve two-dimensional problems self-consistently is presented together with some results on the potential shape in quantum wires defined by shallow etching and the split-gate techniques.

3.1. Self-Consistent Treatment of One-Dimensional Problems

3.1.1. Solving Schrödinger's Equation

In the following discussion, we assume that the problem of a laterally confined electron gas can be treated in a one-particle approximation and that the contributions to the potential in the x and z directions can be separated as outlined previously. To solve the Schrödinger equation for an arbitrary potential in one dimension, a simple finite-difference method can be used, which is sufficient for many problems. For this purpose, the stationary Schrödinger equation is written in discretized form as

$$-\frac{\hbar^2}{2m^*}\frac{D_i\Psi}{\delta_i^2} + V_i\Psi_i = E\Psi_i \tag{13}$$

with

$$D_i\Psi = (\Psi_{i+1} - 2\Psi_i + \Psi_{i-1}) \qquad \text{and} \qquad \delta_i = x_{i+1} - x_i \tag{14}$$

where i denotes the discretization index, δ_i is the spacing between the mesh points, V_i is the value of the confining potential at point i, and E is the energy of the eigenstates. The total number of grid points in the x direction is N. For simplicity, a constant effective mass is assumed in the following. The wave functions are assumed to vanish at the boundaries of the mesh ($\Psi_0 = 0$, $\Psi_{N+1} = 0$). This allows us to transform Eq. (13) into a symmetric band matrix problem, where the elements of the Hamiltonian matrix $\mathbf{H}$ are given by

$$H_{k,k} = +\frac{\hbar}{m^*}\frac{1}{\delta_k^2} + V_k \tag{15}$$

and

$$H_{k,k+1} = H_{k+1,k} = -\frac{\hbar^2}{2m^*}\frac{1}{\delta_k^2} \qquad \text{for } k = 1, \ldots, N-1 \tag{16}$$

All other elements of **H** are zero. To calculate the eigenstates and eigenvectors of the matrix, any standard numerical software can be used. Later, we shall discuss some results that were obtained using EISPACK [51] routines, which simultaneously yield both the eigenvectors and the energy eigenvalues of the problem. Note that the EISPACK routines are reasonably fast on a conventional personal computer, even if a 1-Å resolution is used on a 200-nm-wide system (2000 mesh points).

3.1.2. Solving the Poisson Equation

In the following discussion, we consider a quantum wire with the axis of free motion along the y direction. The translational invariance along y reduces the problem of calculating the confinement potential to the calculation of any arbitrary cut through the potential landscape in the x direction. The total electrostatic potential in the quantum wire is determined by the distribution of charged donors (in the case of a wire defined by etching) or the distribution of electric fields (for a split-gate wire), on the one hand, and by the spatial distribution of the free electrons, on the other hand. In the following, we consider the case of an etched wire, whose confinement is determined by some spatial modulation of the donor distribution with no external electric fields being applied.

A simple and numerically effective way to solve the one-dimensional Poisson equation is obtained, if the spatial region in which the electrostatic problem is to be solved is split into N intervals with a piecewise-constant charge density. We denote the charge density in the nth interval by the constant ρ_n, where ρ_n is composed of the contributions of the ionized donors in the structure and the electrons in the conducting regions. Because, in general, both will depend on temperature, we can write

$$\rho_n = e\left[N_D^*(x,T) - n(x,T)\right] \tag{17}$$

where $N_D^*(x,T)$ is the temperature-dependent density of ionized donors and $n(x,T)$ is the local electron density in the nth interval with $x_n \leqslant x \leqslant x_{n+1}$. Any residual acceptor concentrations or holes are ignored in this consideration. If we further assume a piecewise-constant dielectric constant ε_n, the Poisson equation on the nth interval reads

$$\frac{\partial^2 \varphi_n}{\partial x^2} = -\frac{e\rho_n}{\varepsilon_n \varepsilon_0} \tag{18}$$

where φ denotes the electrostatic potential. Integration yields the following quadratic expression for the electrostatic potential in the nth interval:

$$\varphi_n = -\frac{e\rho_n}{\varepsilon_n \varepsilon_0}\frac{(x-x_n)^2}{2} + c_n(x-x_n) + d_n \tag{19}$$

where c_n and d_n are integration constants. To calculate c_n and d_n, we define $x_0 = 0$ and introduce, for simplicity, the following boundary conditions:

$$\begin{aligned} \varphi_0(x_0) &= 0 \\ \left.\frac{\partial \varphi}{\partial x}\right|_{x=0} &= F \end{aligned} \tag{20}$$

That is, the potential is chosen to be zero at $x = 0$, whereas an electric field F of any desired value can be present at this point. These boundary conditions can be chosen arbitrarily without restricting the generality of the described procedure. The preceding boundary conditions lead to recursion relations for the coefficients d_n and c_n. As starting values, they give $d_0 = 0$ and $c_0 = F$ and, if we require the potential values in adjacent intervals to match at each intersection x_{n+1},

$$\varphi_n(x_{n+1}) = \varphi_{n+1}(x_{n+1}) \tag{21}$$

and the same for the displacement

$$\varepsilon_n \left.\frac{\partial \varphi_n}{\partial x}\right|_{x=x_{n+1}} = \varepsilon_{n+1} \left.\frac{\partial \varphi_{n+1}}{\partial x}\right|_{x=x_{n+1}} \tag{22}$$

we get the following recursive relations for c_{n+1} and d_{n+1}:

$$d_{n+1} = -\frac{e\rho_n}{2\varepsilon_n \varepsilon_0}(x_{n+1} - x_n)^2 + c_n(x_{n+1} - x_n) + d_n \tag{23}$$

and

$$c_{n+1} = -\frac{e\rho_n}{\varepsilon_{n+1}\varepsilon_0}(x_{n+1} - x_n) + \frac{\varepsilon_n c_n}{\varepsilon_{n+1}} \tag{24}$$

Having discretized the Schrödinger and Poisson equations in this way, it is now easy to obtain a self-consistent solution of these two equations by carrying out the usual Hartree iteration scheme, which will be summarized later.

3.1.3. Self-Consistency

To obtain a self-consistent solution of the Poisson and Schrödinger equations, one chooses, as a first step, an initial spatial electron distribution. It may, in principle, be of any shape provided that the integrated electron density equals the predefined one-dimensional electron density in the quantum wire: $\int n(x, T)^{\text{it}=1}\, dx = n^{1\text{D}}$. Here, the superscript it denotes an iteration index; it = 1 denotes the first iteration step. In practice, $n(x, T)^{\text{it}=1}$ is chosen to have some "realistic" shape, given by, for example, the Gaussian distribution function, which will accelerate the convergence of the iteration procedure. The Poisson equation, solved with the initial density $\rho(x)^{\text{it}=1} = e(N_{\text{D}}^{*}(x, T) - n(x, T)^{\text{it}=1})$, now gives the starting configuration of the electrostatic potential, $\varphi^{\text{it}=1}(x)$. The so-obtained potential is then inserted into the Schrödinger equation, whose solution yields a first approximation for the wave functions, and eigenenergies. With these wave functions, the local electron density in the wire can be expressed as

$$n(x, T) = \sum_{i=1}^{N} n_i(T)\left|\psi_i(x)\right|^2 \tag{25}$$

where N denotes the number of occupied subbands and $n_i(T)$ is the temperature-dependent number of electrons per unit length (in the y direction) in each 1D subband. At finite temperature, the Fermi distribution entering into the $n_i(T)$ (see the following discussion) extends to infinite energy. The cutoff number N of subbands used in the sum is, therefore, determined by the required numerical accuracy.

For a given total 1D electron density $n^{1\text{D}}$ in the quantum wire, $n_i(T)$ is obtained from the relation

$$n_i(T) = \int_0^{\infty} g_i^{1\text{D}}(E) f(E - E_{\text{F}})\, dE \tag{26}$$

where $g_i^{1\text{D}}(E)$ is the one-dimensional density of states in the ith 1D subband, $f(E - E_{\text{F}})$ is the Fermi distribution function, and E_{F} is the Fermi energy in the quantum wire.

For zero temperature, the previous equation simplifies to

$$n_i(T = 0\ \text{K}) = \int_0^{E_{\text{F}}} g_i^{1\text{D}}(E)\, dE \tag{27}$$

Because most of the transport investigations on quantum wires are carried out at liquid helium temperatures or below, the assumption of zero temperature in the calculation will be a valid approximation. It can immediately be seen that $n_i(T)$ cannot be calculated directly

because this would require knowledge of the Fermi energy. The Fermi energy itself, however, depends on n^{1D} and the calculated subband energies. Consequently, to obtain $n_i(T)$, one first has to calculate the Fermi energy from the implicit relation

$$n^{1D} = \sum_i n_i(T) = \sum_i \int_0^{E_F} g_i^{1D}(E - E_i)\, dE \tag{28}$$

where, again, $T = 0$ K is assumed. The summation is carried out over all occupied subbands. The outlined procedure yields a local electron density $n(x, T)$, which can now be inserted into the next iteration step. In practice, however, it is not simply $n(x, T)$ that is used, but rather a linear combination of $n(x, T)^{it=1}$ and $n(x, T)$:

$$n^{it=2}(x, T) = (1 - \alpha) n^{it=1}(x, T) + \alpha n(x, t) \tag{29}$$

with the so-called mixing parameter $\alpha \in [0, 1]$. Using this mixing trick, the iteration is repeated until the resulting potential and electron distribution are left unchanged by consecutive iterations. The mixing relation of Eq. (29) is introduced because the self-consistent calculation scheme tends to be unstable. Frequently, the position of the center of the self-consistently calculated potential [and, consequently, that of the charge distribution $\rho(x)$] starts to oscillate about its equilibrium value during the iteration process. Equation (29) serves to damp these oscillations and to achieve fast convergence. Increasing the value of α, in principle, reduces the number of iterations but increases the risk of oscillations. The optimum choice of α depends on the investigated system, but usually α will be of order 0.2 for reasonably fast convergence.

3.1.4. Thomas–Fermi Approximation

In more complex situations, particularly in the field of real device simulation, the solution of the Schrödinger equation becomes numerically very expensive. Therefore, there is a need for approximation methods that take the response of the electron gas to an externally applied potential efficiently into account. A particularly simple approximation scheme is provided by the well-known Thomas–Fermi approach [52–55]. It was originally conceived to make the problem of many electron atoms tractable. In this context, it serves to estimate the local charge density in the atom without invoking a solution of the Schrödinger equation for all energy levels.

Consider a uniform electron gas in some external potential $\varphi_{ext}(x)$, which can be due to the space charge distribution created by charged donors or to externally applied electric fields. The electrons will change their configuration in response to $\varphi_{ext}(x)$, thereby creating an effective potential $\varphi(x, T)$ that will, in general, be temperature dependent even if φ_{ext} is not. In the Thomas–Fermi approach, it is assumed that $\varphi(x, T)$ originates in a spatially varying electron density $n(x, T)$ that is in thermal equilibrium with the local value of the effective potential. Taking the requirements of Fermi statistics into account, this means that the electron density can be written as

$$n(x, T) = \int_0^\infty g(E)\left[1 + \exp\left\{\left(E - E_F - e\varphi(x, T)\right)/k_B T\right\}\right]^{-1} dE \tag{30}$$

where $g(E)$ is the density of states in the semiconductor. The preceding equation is then evaluated as

$$n(x, T) = N_c(x, T) F_{1/2}\left(\left(E_F + e\varphi(x, T)\right)/k_B T\right) \tag{31}$$

where $N_c = 2[m^*(x) k_B T/(2\pi\hbar^2)]^{3/2}$, $m^*(x)$ is a piecewise-constant effective mass, and $F_{1/2}$ is the Fermi–Dirac integral conventionally defined by

$$F_\alpha(\eta) = \frac{1}{\Gamma(\alpha + 1)} \int_0^\infty \xi^\alpha \left[1 + \exp(\xi - \eta)\right]^{-1} d\xi \tag{32}$$

Γ symbolizes the Gamma function. Now, to apply these considerations to a quantum wire, one identifies the external potential $\varphi_{\text{ext}}(x)$ with the potential formed by a fixed space charge resulting from ionized donors, separated from the active region of the wire by a spacer layer. This would be a typical situation for etched quantum wires, but the following considerations also apply to split-gate structures if the proper boundary conditions are chosen. As before, z denotes the growth direction, y is the direction of the wire axis, and x is the direction of the lateral confinement produced by the nanofabrication process. Using Eq. (31) for the electron density in the presence of $\varphi_{\text{ext}}(x)$, one may write the Poisson equation in the following way:

$$\nabla\big[\varepsilon_0\varepsilon(x)\nabla\varphi(x,T)\big] = -\rho(x,T) = -e\big[N_{\text{D}}^{*}(x,T) - n(x,T)\big] \tag{33}$$

Here, $\rho(x,T)$ is the total charge density, $\varepsilon(x)$ is the spatially varying dielectric constant, and $N_{\text{D}}^{*}(x,T)$ is the concentration of ionized donors. Equation (33) already contains the response of the system of conduction electrons to the external potential without requiring the Schrödinger equation to be solved. The price that has to be paid for this convenience is that the Poisson equation now becomes a nonlinear differential equation. It can be solved numerically, using an iteration method similar to the one described previously: One assumes a piecewise-constant charge density $N_{\text{D}}^{*}(x,T)$ and starts with some initial distribution of electrons from which a potential $\varphi(x,T)$ is calculated using the Poisson equation. Then, the iteration step in Eq. (29), which previously required the solution of the Schrödinger equation, is now replaced by simply inserting $n(x,T)$ obtained from the Thomas–Fermi approach. Again, the procedure is repeated until the calculated potential becomes stationary. We refer the reader to [56–58] for more details.

3.2. Self-Consistent Calculations in Two Dimensions

3.2.1. Discretization Scheme and Boundary Conditions

Until now, all considerations and calculations were based on the assumption that the confining potential for narrow electron channels at a GaAs–AlGaAs interface can be separated into two independent components, one describing the approximately triangular potential well at the heterointerface and the other giving the lateral confinement induced by nanofabrication. The numerical problem was then reduced to the solution of equations that only depended on the x coordinate. We now relax this assumption and consider the unrestricted two-dimensional problem. This will enable a more realistic view of the "true" shape of the confining potential. Furthermore, it will become clear that the separation of the potential components underlying the simple models discussed at the beginning of this chapter has to be used with some care.

The principal procedure for the solution of the two-dimensional problem is analogous to that used in the one-dimensional case. As in the preceding section, we start by giving a particularly simple discretization method for the Schrödinger equation. Although there are many advanced methods to solve the Schrödinger equation numerically (see, e.g., [59, 60]), the finite-difference scheme described later [61] will, because of its simplicity, prove to be particularly helpful in any first-principles analysis of commonly encountered experimental situations.

In the two-dimensional Schrödinger equation

$$-\frac{\hbar^2}{2m^*}\left(\frac{\partial^2}{\partial x^2} + \frac{\partial^2}{\partial y^2}\right)\Psi(x,z) + V(x,z)\Psi(x,z) = E\Psi(x,z) \tag{34}$$

where $V(x,z)$ now describes the joint influence of the electric field at the heterostructure interface and the lateral nanostructuring process, we replace the differential quotients by finite differences just as in the preceding section:

$$-\frac{\hbar^2}{2m^*}\left(\frac{D_i\Psi}{\delta_i^2} + \frac{D_j\Psi}{\delta_j^2}\right) + V_{i,j}\Psi_{i,j} = E\Psi_{i,j}$$

with

$$D_i\Psi = (\Psi_{i+1,j} - 2\Psi_{i,j} + \Psi_{i-1,j})$$

and

$$D_j\Psi = (\Psi_{i,j+1} - 2\Psi_{i,j} + \Psi_{i,j-1}) \tag{35}$$

Here, $\delta_i = x_{i+1} - x_i$ and $\delta_j = z_{j+1} - z_j$ are the mesh spacings in the x and z directions, respectively. One now performs an index transformation and defines a new index $k = (i-1)N_j + j$, where N_i and N_j are the number of mesh points in the x and z directions. This gives

$$\frac{\hbar^2}{2m^*}\left(\frac{\Psi_{k+N_j} - 2\Psi_k + \Psi_{k-N_j}}{\delta_i^2} + \frac{\Psi_{k-1} - 2\Psi_k + \Psi_{k+1}}{\delta_j^2}\right) + V_k\Psi_k = E_k\Psi_k \tag{36}$$

where k runs in the interval between 1 and $N = N_iN_j$. As boundary conditions, one again assumes vanishing wave functions at the borders of the mesh: $\Psi_0 = 0$, $\Psi_{N+1} = 0$. This transforms the eigenvalue equation into a symmetric band matrix problem, where the elements of the Hamiltonian matrix $\mathbf{H}$ are now given by

$$\begin{aligned} H_{k,k} &= +\frac{\hbar^2}{m^*}\left(\frac{1}{\delta_i^2} + \frac{1}{\delta_j^2}\right) + V_k \\ H_{k,k-N_j} &= H_{k-N_j,k} = -\left(\frac{\hbar^2}{2m^*\delta_i^2}\right) \\ H_{k,k+1} &= H_{k+1,k} = \begin{cases} 0 & \text{if } k = nN_j \text{ and } 1 \leqslant n \leqslant N \\ -\left(\frac{\hbar^2}{2m^*\delta_j^2}\right) & \text{otherwise} \end{cases} \end{aligned} \tag{37}$$

All other elements of $\mathbf{H}$ are zero. Once again, one obtains a practical discretization of the Schrödinger equation, which can easily be implemented on a personal computer using standard numerical algorithms for the solution of the resulting sets of linear equations. Later, some results will be shown that were obtained using the same EISPACK routines already mentioned in the context of the one-dimensional self-consistent calculations.

The next important step is the discretization of the Poisson equation. Usually, it is not reasonable to discretize and to solve both the Poisson and the Schrödinger equations in the whole discretization range because the electronic wave functions are expected to contribute only in the vicinity of the heterostructure interface. To achieve high accuracy and to reduce computation times, the Schrödinger equation is, therefore, solved only on a subset of the Poisson mesh. An example of this gives Figure 4, which shows the two discretization meshes used for a self-consistent simulation of a shallow etched quantum wire. As shown in this figure, the Schrödinger equation is solved only in the nonetched regions of the sample and there only in the area immediately adjacent to the heterostructure interface. The rest of the sample is assumed to be totally depleted. The two-dimensional Poisson equation can be solved on a rectangular mesh using the so-called simultaneous overrelaxation method [62]. As in the one-dimensional case, we assume zero temperature and define a local charge density

$$\rho(z,x) = N^*(z,x) + n^{1D}(z,x) \tag{38}$$

which consists of the contribution $N^*(z,x)$ of the ionized donors and the local electron concentration $n^{1D}(z,x)$. The discretized 2D Poisson equation can then be written in the following matrix form:

$$a_{i,j}\varphi_{i+1,j} + b_{i,j}\varphi_{i-1,j} + c_{i,j}\varphi_{i,j+1} + d_{i,j}\varphi_{i,j-1} + e_{i,j}\varphi_{i,j} = \frac{e\delta_j\delta_j\rho_{i,j}}{\varepsilon\varepsilon_0} \tag{39}$$

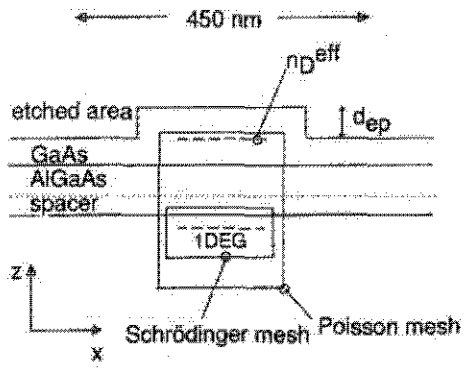

Fig. 4. Typical choice of the Schrödinger and Poisson mesh for a shallow etched quantum wire. A typical discretization grid for the solution of the Schrödinger equation often encountered in the literature consists of 51 × 51 points. (Source: Reprinted with permission from [61].)

Here, i counts the mesh points in the x direction, j those in the z (growth) direction, and δ_i, δ_j are the mesh spacings in the two directions. $\rho_{i,j}$ and $\varphi_{i,j}$ are the values of the charge density and the electrostatic potential at the point (i, j), respectively. The elements of the matrices **a**, **b**, **c**, **d**, and **e** in Eq. (39) are $a_{ij} = b_{ij} = c_{ij} = d_{ij} = 1$ and $e_{ij} = -4$ at the inner mesh points. To define them at the boundary of the mesh, one introduces suitable electrostatic boundary conditions. In the next subsection, several results of calculations using to the outlined method will be discussed. There, Neumann boundary conditions (zero electric field) are used on three sides of the underlying mesh (see Fig. 4). To fix the potential scale, Dirichlet conditions are used at the upper side. Note that, for simplicity, one assumes a position-independent dielectric constant ε in Eq. (39). This is a good approximation for quantum wires fabricated on GaAs–AlGaAs heterostructures, because there is little difference in the relative dielectric constants of GaAs and AlGaAs.

Self-consistency of the numerical solutions for the wave functions, energy levels, and the potential shape are now obtained in the same way as described for the one-dimensional case. Starting with an arbitrary electron distribution $n^{1D}(x, z, T)$, one first calculates the corresponding electrostatic potential. From this, a first approximation to the subband energies and wave functions is obtained. The electrons are then distributed among their energy levels taking the 1D form of the density of states into account. In most cases, zero temperature can be assumed for simplicity. The resulting new electron distribution $n(x, z, T)^{it=i}$ is again mixed with $n(x, z, T)$ using a weighting factor α ($\alpha = 0, \ldots, 1$) according to

$$n^{it=i+1}(x, z, T) = (1 - \alpha)n^{it=i}(x, z, T) + \alpha n(x, z, T) \tag{40}$$

The new value of $n(x, z, T)^{it=i+1}$ is then used in the subsequent iteration for the Poisson equation.

3.2.2. *Some Numerical Results*

In the following, some examples for self-consistently calculated confinement potentials of quantum wires are given. They serve as an illustration for the calculation methods outlined previously and will also indicate the limits of validity of the assumptions made previously, namely on the approximation of confining potentials by simple analytical functions and on the separate treatment of the confinement in lateral and growth direction.

Figure 5 shows the confinement potential obtained from a solution of the two-dimensional Poisson–Schrödinger (PS) model for a wire fabricated by shallow etching on a GaAs–AlGaAs heterostructure. Figure 4 shows the parametrization of the system used in the numerical calculation. The etching process, which removes a layer of thickness d_{ep}

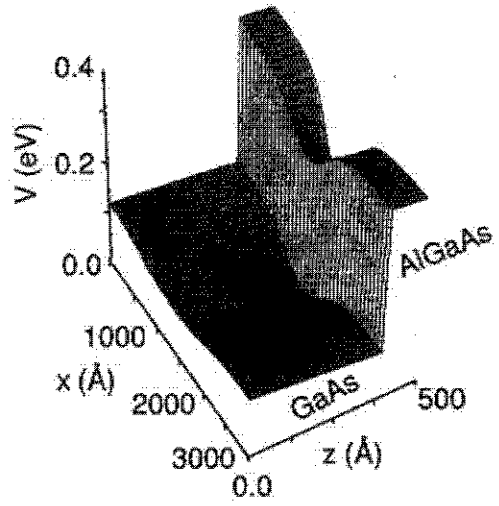

Fig. 5. Three-dimensional view of a quantum wire potential. The vertical potential step is the conduction band offset at the interface of the GaAs and the AlGaAs. For clarity, only a subset of the Poisson mesh is shown.

from the GaAs cap, induces a lateral modulation of the density of charged donors. Because the exact distribution of the donors and the surface states is not known exactly, it is modeled by a sheet of positively charged donors with thickness δ_z, positioned at $z = d_{ep}$. The profile of the charge distribution n_D^{eff} is assumed to be constant in the z direction and to be correlated with the profile of the free carrier distribution in the wire itself. This can be formally expressed as

$$n_D^{eff}(y, z = d_{ep}) = \frac{1}{\delta_z} \int n_s^{1D}(y, z)\, dz \tag{41}$$

To accelerate the convergence of the calculation, a Broyden algorithm [63, 64] can be used. The self-consistent solution is then obtained typically after 15 iterations with average changes in the subband energies of less than 0.1 meV between the iteration steps. Note that the discretization grid of the PS model has to be fine enough to resolve all the extrema of all wave functions involved in the calculation of the charge density.

From the shape of the potential, it is obvious that it is not possible to separate the contributions of the z confinement from that of the x confinement over the entire integration region. However, within the range of the corresponding wave functions, the relation between the two contributions may be "linearized" and their separation can be considered to be a good approximation in many cases.

A common way to give a one-dimensional representation of the results of a two-dimensional calculation is to perform a cut through the potential profile at the maximum of the electron charge density $n_s^{1D}(y, z)$, as shown in Figure 6. This also allows us to decide what form an analytical model potential should have in order to give a fair approximation of the self-consistently calculated potential. Figure 6 reveals that, in the case of shallow etched quantum wires, the self-consistent confinement potential has a sinusoidal shape. The small oscillations superimposed on the sine potential of Figure 6 are due to small local variations in the self-consistently calculated electron density. Note that the situation shown in Figure 6 is typical for a relatively high electron density, which occurs, for example, after illumination. The Fermi level is located near the upper edge of the potential modulation and the highest lying of the eight occupied subbands are situated in the nonparabolic part of the potential.

Note also that there is a considerable "offset" in the zero-point energy, that is, a large energetic distance between the conduction band bottom and the lowest subband. This offset

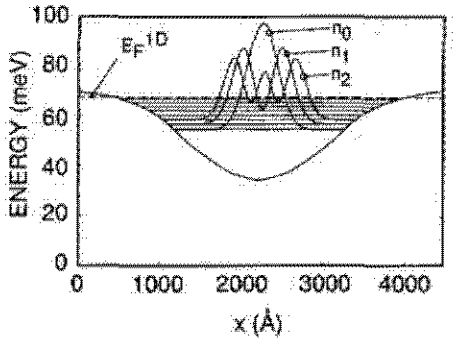

Fig. 6. Cut through a quantum wire potential at the total charge density maximum. The 1D subband energies and the squared wave functions of the lowest three subbands are also shown. (Source: Reprinted with permission from [61].)

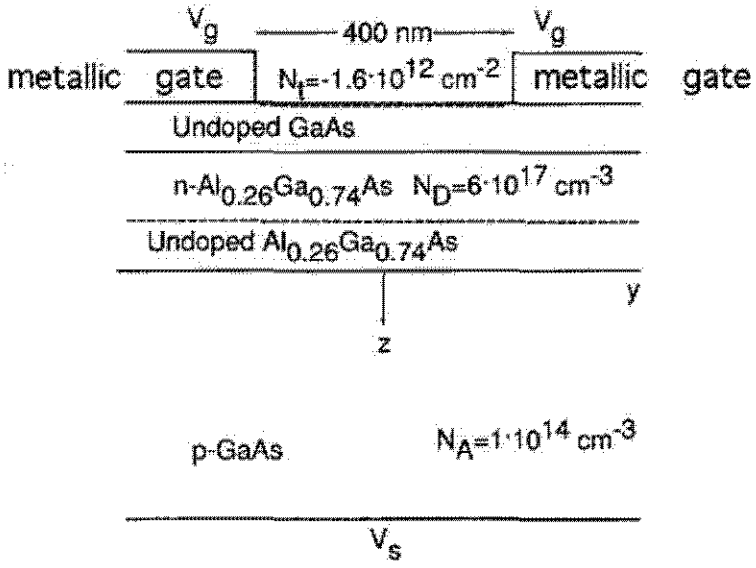

Fig. 7. Sample geometry and sample parameters for a typical split-gate wire fabricated on a GaAs–AlGaAs heterostructure. (Source: Reprinted from [44], with permission of Elsevier Science.)

reflects the position of the lowest occupied subband of the underlying 2D electron gas, which is the zero point for the superposed quantization into 1D subbands. (Fermi energies considered later on will generally not be given with respect to the conduction band bottom but with respect to the bottom of the lowest 2D subband.) This is another manifestation of the fact that the x and z components of the total confining potential cannot be considered separately. It is another interesting feature of the calculated results that the spatial extension of the wave functions corresponding to the highest occupied subbands can even exceed the geometrical width of the wire structure (which is on the order of 200 nm in Fig. 6).

In the case of low electron densities, the overall cosine shape of the confinement potential is conserved. However, the Fermi level and the occupied subbands are then located near the bottom of the potential where it may be well approximated by a parabolic shape.

We now compare these results to those obtained from self-consistent calculations performed for a split-gate geometry. The corresponding sample structure is depicted in Figure 7. In contrast to the shallow etching method, the lateral confinement is now induced by the external voltage applied to metallic gates on top of the GaAs–AlGaAs heterostructure.

The main advantage of the split-gate geometry is the possibility of tuning the confinement strength. This allows us to change the behavior of the confined electron system from effectively two dimensional to strongly confined one dimensional. Self-consistent wire potentials for the split-gate geometry of Figure 7 are shown in Figure 8 for various values of the gate voltage. The corresponding charge density distributions are reproduced in Figure 9.

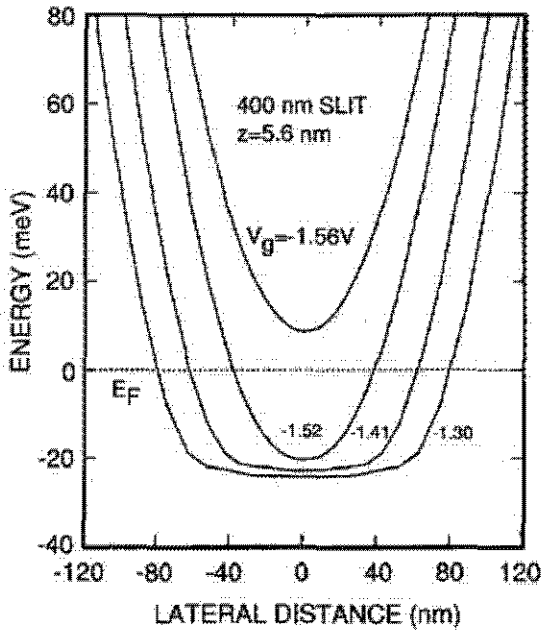

Fig. 8. Self-consistently calculated potential for a quantum wire in split-gate geometry. The potential is plotted for $z = 56$ Å below the GaAs–AlGaAs interface and for four different gate voltages. (Source: Reprinted from [44], with permission of Elsevier Science.)

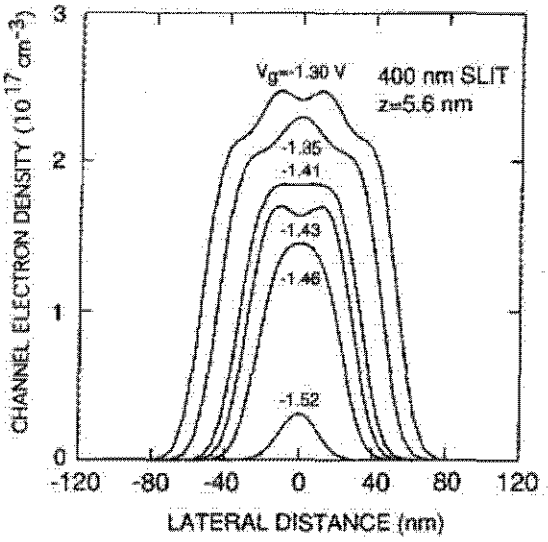

Fig. 9. Self-consistently calculated electron density for a quantum wire in split-gate geometry. The electron density is plotted for different gate voltages. (Source: Reprinted from [44], with permission of Elsevier Science.)

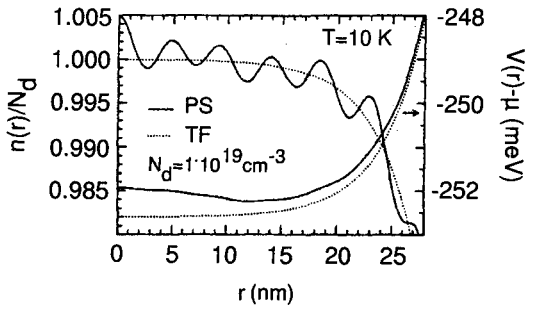

Fig. 10. Self-consistently calculated potential and charge distribution of a cylindrical quantum wire. The dotted lines are the results obtained through the Thomas–Fermi (TF) approximation; the solid lines are obtained through a self-consistent solution of the Schrödinger and Poisson equations. (Source: Reprinted with permission from [54]. © 1992 American Physical Society.)

Figure 8 reveals the main qualitative difference between the split-gate and the shallow etching geometry: For low electron density, both cases yield an approximately parabolic potential, whereas, at higher electron densities, the split-gate potential develops a flat bottom. The electron density plotted in Figure 9 shows several oscillations, which, in fact, reflect the structure of the corresponding 1D wave functions. The position and the amplitude of these oscillations depend on the gate voltage, which nicely reflects the increasing number of occupied subbands as the gate bias is lowered.

3.2.3. Thomas–Fermi Approximation in Two Dimensions

In the last paragraph of this section, we take a brief look at the application of the Thomas–Fermi (TF) approximation to two-dimensional problems. In principle, there is no difference to the one-dimensional case considered earlier, except for the number of independent variables. We, therefore, restrict the following discussion to a comparison of the results generated by the TF and PS approaches in Figure 10. The figure shows the potential and the local charge density as a function of the radius for a cylindrical, homogeneously doped quantum wire [54]. Dotted lines represent the Thomas–Fermi results; solid lines correspond to a fully self-consistent solution of the Poisson and Schrödinger equations. As discussed previously and as also seen in the figure, the PS approach leads to oscillations in the electron density, which are not revealed by the TF approximation. This is because the latter yields some kind of "average" behavior of the electron density and the confinement potential. The difference between the two approaches will become weaker when the number of occupied subbands or the temperature increases. In general, the Poisson–Schrödinger results are expected to approach the Thomas–Fermi results, as soon as the energy spacing between the occupied subbands becomes smaller than $k_B T$.

3.3. Three-Dimensional Modeling of Quantum Dots

In this section, we give a very brief survey on the self-consistent treatment of quantum dots without going into great detail. For the reader particularly interested in this subject, we give a short list of references, which may serve as a starting point for finding more detailed information on this topic.

There are mainly three obvious possibilities for calculating the electronic properties of quantum dots: As a first approximation, again a one-dimensional model potential such as, for example, an anharmonic oscillator potential suggests itself (Luban et al. [65]) for the simulation of electronic properties of a quantum dot nanostructure. As a next step, one might consider a circular symmetric "quantum disk" system. This implies the use of cylinder coordinates and, consequently, the solution of a two-dimensional Schrödinger equation

using the methods described in the previous sections. Finally, and also numerically most challenging, is a fully self-consistent simulation in three dimensions. The first to do this were Kumar et al. [66], who calculated the electron states of a quantum dot including the presence of a magnetic field. Recently, fully self-consistent calculations became more important because of progress in nanofabrication and the need for a three-dimensional (3D) device simulator for practical applications. The interested reader is referred to the work of Udipi et al. [67] for a model of lateral quantum dots on silicon and Scholze et al. [68] for various other aspects of device simulation.

The case of a circular dot geometry has been intensively investigated during the past years. The most popular examples of this are pillar-shaped double-barrier resonant tunneling diodes with diameters in the nanometer range, the dot being formed in the well between the barriers. The intensive work on these systems was performed mainly at Texas Instruments (see, e.g., [55]) and was motivated by two major aspects. First, the increasing scale of integration in commercial devices strongly requires this kind of calculation and, second, nanostructured double-barrier resonant tunneling diodes (DBRTDs) are useful for certain applications that require ultralow power consumption. The efforts in this field aim at the conception of a nanodevice simulation tool capable of calculating current–voltage characteristics from the given fabrication parameters. The computer simulations always employ the Thomas–Fermi approximation to keep the computational expense reasonably low. It should be noted, however, that the calculation of IV characteristics requires not only the self-consistent treatment of confinement potentials but also the calculation of tunneling currents. Therefore, scattering processes have to be included [69] for realistic simulations, which is a topic that we have completely omitted in the preceding discussion. Pioneering work in this field was done by Frensley [70] and Luban and Luscombe [71]. Detailed accounts on the problems and methods encountered in nanodevice simulation can be found in their work and in the other references given in the context of the Thomas–Fermi approximation.

4. TRANSPORT SPECTROSCOPY OF QUANTUM WIRES

In the following, we discuss the magnetotransport properties of quantum wires in the diffusive transport regime. We shall focus on those phenomena that provide a more or less direct access to those quantum wire properties directly related to the confinement potential, such as the subband spacing or the wire width. The standard example for an experiment yielding the subband spacing is the magnetic depopulation measurement. A second example that has only recently been shown to be suitable for the subband spectroscopy on quantum wires is the observation of the magnetophonon resonance at elevated temperatures. In the interpretation of the experimental results, the confinement will be approximated by simple and frequently used model potentials, as they are suggested by the self-consistently calculated results introduced in the preceding chapter. We shall discuss the limits of the validity of these approximations and also outline a method that gives direct information on the shape of the actual potential from the comparison of high- and low-temperature magnetoresistance measurements. Several other phenomena exhibited in a magnetoresistance experiment, such as the suppression of backscattering in a magnetic field or the weak localization effect, are also considered. They provide additional information on several characteristic lengths important for the characterization of long quantum channels in the diffusive regime. The particular magnetoresistance "anomalies" occurring in lateral surface superlattices and their use for the determination of potential parameters will be discussed in the subsequent chapter.

According to the objective of this chapter, ballistic transport phenomena are completely neglected in the following. This is mainly because the phenomena typically examined in this regime, in general, do not rely strongly on a detailed knowledge of the properties

of confinement potentials. The reader who is especially interested in a review on ballistic transport is referred to the excellent articles by Beenakker and van Houten [25], van Houten et al. [26], Timp [72], or the textbook of Datta [73] as well as the references cited therein.

4.1. Magnetic Depopulation Experiments

4.1.1. Determination of Subband Energies

The "classic" method to gain information on the confining potential in quantum wires and, in particular, on the energy spacing of the 1D subbands is the so-called magnetic depopulation measurement [74–76]. It exploits the particular features of the low temperature ($T \leqslant 4.2$ K) longitudinal magnetoresistance of a quantum wire sample with a magnetic field applied in the growth direction of the underlying heterostructure. As already mentioned earlier, the magnetic field enlarges the energetic separation of the 1D subband edges and, therefore, the number of occupied subbands is successively reduced with increasing magnetic field. This is shown in Figure 11, where the magnetic field–dependent density of states of a one-dimensional system is plotted for three different magnetic fields. The position of the Fermi level E_F is defined through the electron density in the quantum wire and also depends on the magnetic field strength.

As shown in Section 1, the energy dispersion for a parabolic confinement potential in a perpendicular magnetic field is given by

$$E_n(k_y) = \hbar\omega\left(n + \frac{1}{2}\right) + \frac{1}{2}\frac{\hbar^2 k_y^2}{m_{\text{eff}}(B)} \qquad n = 0, 1, 2, \ldots \tag{42}$$

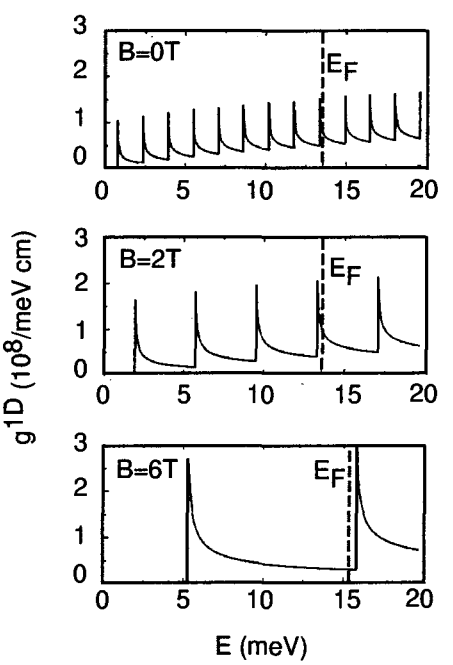

Fig. 11. One-dimensional density of states according to Eq. (43) plotted for magnetic fields of $B = 0$ T, 2 T, and 6 T, respectively. Because constant carrier density is assumed, the position of the Fermi level is dependent on the magnetic field. The density of states is calculated for the ideal case of absent lifetime broadening of the magnetoelectric hybrid levels. As shown by Berggren et al. [75], realistic assumptions for the lifetime broadening leave the main qualitative features of the magnetic depopulation process unchanged. The lifetime broadening in a magnetic field is found to be strongly dependent on the wavevector component k_y.

The density of states for a particular subband is given by the expression

$$g_n^{1D}(E) = \frac{1}{\pi}\left(\frac{dE}{dk_y}\right)^{-1} = \frac{\sqrt{2m_{\text{eff}}(B)}}{\pi\hbar}\frac{1}{\sqrt{E-\hbar\omega(n+1/2)}} \tag{43}$$

If we sum this expression over all N occupied subbands, we obtain

$$g^{1D}(E) = \frac{\sqrt{2m_{\text{eff}}(B)}}{\pi\hbar}\sum_{n=0}^{N}(E-E_n)^{-1/2}\Theta(E-E_n) \tag{44}$$

which is plotted in Figure 11. The density of states at the Fermi energy oscillates as a function of magnetic field and gives rise to an oscillating impurity scattering time. A semi-quantitative way to see this is to consider the scattering from a set of dilute impurities in first-order perturbation theory. If the scattering potential is delta function like with a strength V_0 it can be shown that [77]:

$$\tau^{-1} = \frac{\pi}{\hbar}g^{1D}(E_F)c_{\text{imp}}V_0^2 \tag{45}$$

Here, c_{imp} denotes the sheet concentration of impurities. At low temperatures, impurity scattering may be considered to be the dominant contribution to the resistivity. The magnetic depopulation effect will, therefore, manifest itself in the oscillatory behavior of the semiclassical magnetoresistivity $\rho_{xx} \propto \tau^{-1} \propto g^{1D}(E_F)$.

To reveal the oscillatory structure in the magnetoresistance, it is advantageous to consider arrays of identical quantum wires. For a single quantum wire, the low-field magnetic depopulation oscillations may be obscured by the so-called aperiodic conductance fluctuations (for an introduction to this topic, see, e.g., [25]). This quantum interference effect originates in the large-phase coherence length in a mesoscopic electron system and it is averaged out if an ensemble of quantum wires is investigated.

Several methods for the fabrication of such arrays of quantum wires have been successfully applied. The simplest possible sample layout consists of a two-terminal configuration where an array of quantum wires is extended between two large contacts. To get rid of the contact resistance, one may evaporate a metal gate on top of the wire array intended for the application of a small modulation voltage [78]. This sample geometry is shown in Figure 12a.

The magnetoresistance is then measured using a lock-in technique and gives the resistance of only those regions covered by the modulating gate. The influence of the contact resistance is thereby effectively eliminated. A variation of this method was used by Brinkop et al. [79, 80, 119]. Their fabrication principle exploits a modified split-gate technique to create the wire array as indicated schematically in Figure 12b. In contrast to the sample

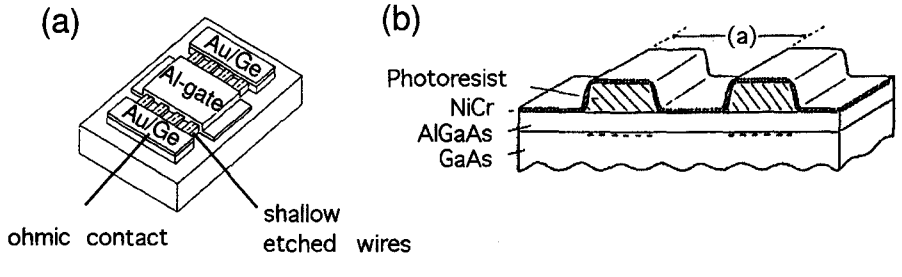

Fig. 12. Two different fabrication principles for arrays of parallel quantum wires. (a) Wires fabricated by laser holography and shallow etching. The top Al gate serves as a modulation electrode for lock-in measurements intended to eliminate the contribution of the contact resistance. (b) A Ni/Cr gate evaporated over nanostructured photoresist stripes. This modified split-gate geometry allows one to tune the confinement strength. (Source: Part b reprinted with permission from [119]. © 1989 American Physical Society.)

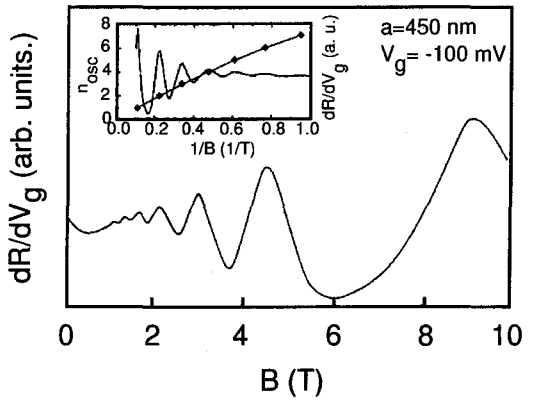

Fig. 13. Derivative of the magnetoresistance with respect to the modulated gate voltage V_g, measured for an array of quantum wires. The sample layout is shown in Figure 12a. The period of the shallow etched grating was 450 nm. The inset shows the same data plotted as a function of the inverse magnetic field together with a Landau plot of the corresponding magnetoresistance maxima.

shown in Figure 12a, where the confinement is achieved by shallow etching, the purpose of the gate in this configuration scheme is twofold. First, it produces the 1D confinement and, second, it serves as a modulating gate for contact resistance elimination. For the purpose of spectroscopic investigations, it furthermore provides an effective grating coupler for far-infrared radiation (see [79]). This sample configuration has the advantage of supplying quantum wires with a *tunable* confinement strength.

Figure 13 shows a typical magnetoresistance trace obtained for a sample structure as depicted in Figure 12a, using a modulated gate voltage to eliminate the contact resistance [78]. A minimum occurs whenever the Fermi level is shifted across the bottom of the highest occupied magnetoelectric subband, where a sharp maximum in the density of states is followed by a region of minimal density of states (DOS). If a running subband index n_{osc} is assigned to each minimum and the index n_{osc} is plotted against the inverse magnetic field position of the corresponding minimum in R_{xx}, a fan chart or so-called Landau plot is obtained (cf. the inset of Fig. 13). The characteristic feature in this plot, which demonstrates the presence of a 1D confinement, is the deviation from linearity at low magnetic fields. This behavior can be understood from Eq. (42), which describes the subband energies in a parabolic confinement potential. For the subband edge ($k_y = 0$) of the nth subband, Eq. (42) yields $E_n(B) = \hbar\sqrt{\omega_c^2 + \omega_0^2}(n + \frac{1}{2})$. For large magnetic fields, ω_0 may be neglected and the resulting dependence of n_{osc} on B^{-1} is linear. This is the well-known behavior of the Shubnikov–de Haas oscillations observed in the magnetoresistance of unstructured 2DEGs. The presence of the lateral confinement characterized by the additional frequency ω_0 becomes visible only when it is at least of the same order of magnitude as the cyclotron frequency. For those magnetic fields where this is the case, the relation between n_{osc} and $1/B$ is no longer linear. This is the general signature of lateral confinement in narrow channels, no matter what the actual shape of the confining potential is [74, 81].

It is instructive to analyze the $n_{\mathrm{osc}}(B^{-1})$ dependence in terms of a parabolic confinement potential [75] because this allows the analytical treatment of the magnetic depopulation effect and provides a particularly simple way to determine wire parameters from an actual measurement. The situation encountered in a magnetic depopulation experiment is depicted in Figure 14, which shows the energy of the magnetoelectric subband edges as a function of B. Whenever the Fermi level crosses the edge of the highest occupied magnetoelectric hybrid subband, that is, whenever $E_F = N\hbar\omega(B)$, a minimum in the magnetoresistance is observed. Because the 1D electron density in the channel is constant, the

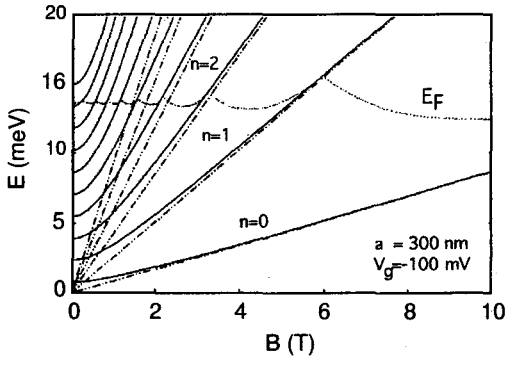

Fig. 14. Dependence of the magnetoelectric subband energy on magnetic field strength, calculated for a parabolic confinement with $\hbar\omega_0 = 1.57$ meV. The dashed–dotted lines show the corresponding behavior of the Landau levels in an unstructured 2DEG. Also shown is the oscillating Fermi energy, calculated for a 1D carrier density of $n_{1D} = 5.68 \times 10^6$ cm^{-1}. n is the subband index.

Fermi level oscillates with increasing magnetic field. From the 1D carrier density at zero temperature

$$n_{1D} = \int_0^{E_F} g^{1D}(E, B)\, dE \tag{46}$$

one obtains, together with Eq. (44) and $E_F = E_N$,

$$n_{1D} = \frac{2}{\pi}\sqrt{\frac{2m^*}{\hbar}}\,\frac{\omega^{3/2}}{\omega_0}\sum_{n=0}^{N} n^{1/2} \tag{47}$$

This finally leads to the following relation between the index N of the highest occupied subband and the magnetic field position of the corresponding magnetic depopulation minimum in R_{xx}:

$$B_N = \frac{m^*}{\hbar e}\sqrt{\left[\frac{\pi\hbar n_{1D}\hbar\omega_0}{\sqrt{8m^*\sum_{n=0}^{N} n^{1/2}}}\right]^{4/3} - (\hbar\omega_0)^2} \tag{48}$$

If this relation is fitted to the experimentally determined Landau plot, N plays the role of the previously introduced n_{osc}. As fit parameters, one obtains the subband spacing $E_0 = \hbar\omega_0$ and the 1D carrier density n_{1D}. The latter is related to the approximately linear behavior of the $n_{osc}(1/B)$ plot for high-magnetic-field values [75], which is obtained by replacing in Eq. (47) ω by ω_c:

$$N \approx \frac{m^*/e}{(2m^*\hbar)^{1/3}}\left(\frac{3\pi}{4} n_{1D} E_0\right)^{2/3}\frac{1}{B_N} \tag{49}$$

In the preceding section, we have seen that in the case of quantum channels defined by a split-gate geometry the confining potentials as obtained from self-consistent calculations have the shape of a Woods–Saxon potential with a flat bottom. Only for very narrow channels or at quite low electron densities does the potential assume an approximately parabolic form [44]. In the case of quantum wires defined by the shallow etching method, the self-consistent calculations showed that the effective potential felt by the electrons is of a sinusoidal shape [61]. It is again for relatively low electron densities that the electronic wave functions are concentrated near the bottom of the sinusoidal potential where it is well described by a parabola. Only in these cases will the parabolic model and the described fitting procedure be able to reproduce the experimental depopulation data and give results

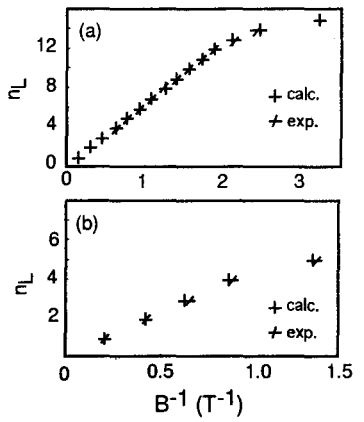

Fig. 15. Experimental and calculated sublevel index n_L versus the inverse magnetic field positions of the resistance minima for two different samples. The theoretical values are calculated under the assumption of a square-well potential and fitted to the experimental points with the channel width and the 1D carrier density as fit parameters. (a) Wide channel (estimated width and carrier density are 378 nm and 1.16 nm^{-1}, respectively). (b) Narrow channel (162 nm, 0.38 nm^{-1}). The wide-channel sample is well described by a square-well potential. The parabolic approximation is found to give better results for the narrow channel (cf. [75]), but turned out not to be suitable for a description of the wide-channel experiment. (Source: Reprinted with permission from [81].)

for channel width and electron density that are in good agreement with independently estimated values.

The second strongly simplified model potential, the square well, does not lend itself to as simple an analytical treatment as the parabolic potential. Rundquist [81] applied a numerical fitting procedure to describe wide and narrow channels defined by the split-gate geometry using a square-well confinement potential. As expected, the square-well model is able to describe wide channel experiments where the parabolic model does not give convincing results and vice versa (cf. Fig. 15, where the experimental results are plotted together with a numerical fit of the results with a square-well model). However, even in the simple case of a square well, the fitting procedure becomes numerically very expensive and is not easily implemented in routine investigations.

Another model potential used to approximate the flat bottom potential of split-gate wires at high electron densities (or, alternatively, low gate voltages) is given by $V(x) = (m^*\omega_0^2/2)(|x| - t/2)^2$ for $|x| \geqslant t/2$ and zero otherwise. It has been investigated in Wentzel, Kramers, Brillouin (WKB) approximation by Berggren and Newson [76]. The use of this potential in the numerical analysis of an experimental situation requires one additional fit parameter, namely the width t of the flat potential section. If, in addition, a modulating gate configuration is used for the magnetoresistance measurement, a phase shift in the dR_{xx}/dV_G traces has also to be taken into account, which requires adding a further unknown parameter B_{offset} to the positions of the magnetic depopulation minima. Altogether, one thus needs four fit parameters for the analysis of the Landau plot. The so obtained values of E_0 and n_0 are questionable in particular when the Landau plot consists of only a few data points.

4.2. Magnetosize Effects and Weak Localization in Quantum Wires

4.2.1. Magnetosize Effects

A useful quantity for the characterization of quantum channels is the electrical width W, which can be estimated from several independent effects in the magnetic field and temperature dependence of the sample resistance. The values extracted for W allow us to

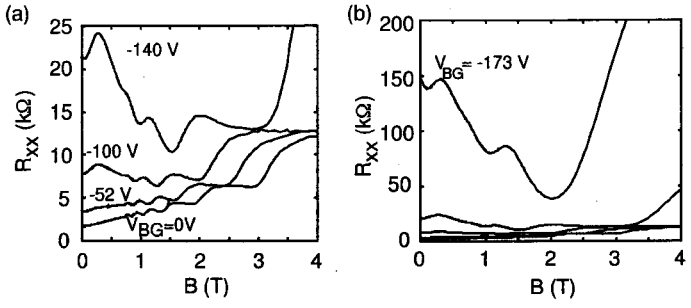

Fig. 16. Low-temperature ($T = 2$ K) magnetoresistance of an array of shallow etched quantum wires, measured with different back-gate voltages applied to the substrate. At low back-gate voltages, the behavior of the system corresponds to a modulated 2D gas. At higher gate voltages, the Fermi level is reduced below the modulation potential amplitude and typical 1D features are observed, such as the large magnetosize peak at $B = 0.27$ T and the negative differential magnetoresistance caused by a suppression of 1D weak localization at $B \leqslant 0.1$ T. The pronounced negative differential magnetoresistance superimposed on the depopulation oscillations at $V_G \geqslant -100$ V is due to the suppression of backscattering by a magnetic field (cf. Fig. 17). The -173-V trace has been drawn separately for clarity (b). The squeezed traces at the bottom of part b are the same curves as in part a.

cross-check whether a model potential used in the analysis of magnetic depopulation experiments is well suited to describe the experimental situation.

Figure 16 shows two-terminal magnetoresistance traces for an array of quantum wires fabricated by laser holography and shallow etching. The etching is very shallow in this case such that without additional measures only a periodic potential modulation is superimposed on the 2DEG. The results of Figure 16 were obtained without application of a modulating front-gate voltage and, therefore, contain the contribution of the contact resistance which, however, is small in this case. The electron density was reduced by applying a negative back-gate voltage on the substrate side of the sample. In this way, the Fermi energy becomes gradually smaller than the amplitude of the potential modulation, eventually leading to a system of well-separated quantum wires. The magnetoresistance traces depicted in the figure clearly show the evolution of two magnetoresistance phenomena typical for narrow electron channels in the diffusive transport regime: magnetosize effects and weak localization.

We first consider magnetosize effects. With increasing back-gate voltage, that is, increasing confinement of the electrons to 1D channels, a magnetoresistance peak evolves at about 0.3 T. This so-called *magnetosize peak* has been shown by Thornton et al. [82, 83] to be due to *diffuse* scattering from the channel walls of electrons moving on cyclotron orbits. It can be shown that this effect can be explained by purely classical arguments and that the presence of diffuse boundary scattering is an essential prerequisite for the observation of a magnetosize peak. Note that the mean free path of the electrons has to be large enough that boundary scattering contributes appreciably to the total wire resistance. The situation is depicted schematically in Figure 17, which shows two classical electron trajectories at two different field strengths [25]. For field strengths where the cyclotron radius is of the order of $R_c \approx W/2$ (Fig. 17a, W is an effective wire width), the probability for electron backscattering is considerably larger than in the case of $R_c \ll W/2$ (Fig. 17b), provided that the scattering from the channel boundaries is predominantly diffuse. The reduction of backscattering for $R_c \ll W/2$ is also responsible for the negative differential magnetoresistance observed in the field range beyond the magnetosize peak for the most strongly confined channels in Figure 16.

As has been found experimentally by Thornton et al. [82], the magnetic field position B_{ms} of the magnetosize peak can be related to the effective width W_{eff} of the quantum wire by $W_{eff} \approx 0.55 R_c^{ms}$, where $R_c^{ms} = \hbar k_F / e B_{ms}$. It is not straightforward to give an unambiguous meaning to the effective wire width W_{eff} obtained from the magnetosize peak.

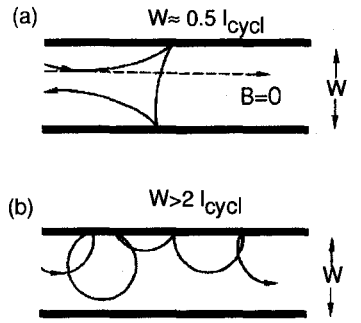

Fig. 17. Classical cyclotron trajectories in a narrow channel with diffuse side-wall scattering, illustrating the origin of the magnetosize peak. (a) If the cyclotron radius (l_{cycl}) is near the indicated value, diffuse side-wall scattering can reverse the motion of an electron, leading to an enhanced resistance. (b) At higher magnetic fields, backscattering is suppressed and the resistance is reduced below the zero-field value. (Source: Reprinted with permission from [25].)

The definition of W_{eff} depends on the underlying model potential. Even if a particular model has been chosen, there are several possibilities to define W_{eff}. Consider as an example the parabolic confinement potential. One way to define W_{eff} is to take the distance between the turning points of the classical motion at the Fermi energy:

$$W_{\text{eff}} = \frac{2\hbar k_{\text{F}}}{m\omega_0} \tag{50}$$

(ω_0 is the confining frequency). An alternative definition is given by $W_{\text{eff}} = n_{1\text{D}}/n_{2\text{D}}$. $n_{1\text{D}}$ can, for example, be estimated from the approximately linear section of the Landau plot. If one starts from Eq. (47), replaces the summation over ν by an integration, and takes into account that in the limit of high magnetic fields $\omega \approx \omega_{\text{c}}$, one obtains

$$n_{1\text{D}} \approx \frac{4}{3\pi\omega_0 m^*}\sqrt{\frac{2}{\hbar}}(eBN)^{3/2} \tag{51}$$

This formula describes a situation analogous to the depopulation of pure Landau levels in a two-dimensional electron system. Taking the corresponding relation between the Landau level index N and the sheet electron density of the underlying 2DEG:

$$n_{2\text{D}} = \frac{e}{\pi\hbar}NB \tag{52}$$

one obtains, as a final result for W_{eff},

$$W_{\text{eff}} = 2\pi\left[\frac{2\hbar}{3\pi m^*\omega_0}\right]^{2/3} n_{1\text{D}}^{1/3} \tag{53}$$

Note that the application of Eq. (50) or Eq. (53) implicitly assumes that the overall sheet electron density $n_{2\text{D}}$ is not affected by the nanofabrication process, which will be the case only for relatively wide channels. In general, the lateral confinement will raise the conduction band bottom also in ungated or nonetched regions of the quantum wire (cf. Fig. 8).

Several other definitions for effective wire widths are possible. They rely, for example, on the lateral extension of the wave function in the Nth magnetoelectric hybrid level [84]. All these definitions give values for W_{eff} that differ from each other, but nevertheless allow one to estimate the correct order of magnitude. A comparison of W_{eff}, as obtained from a model potential, with the experimentally determined value therefore allows one to decide if the applied model gives reasonable results.

It should be emphasized that not every quasi one-dimensional system will display a magnetosize maximum. For wires defined by split gates, for example, it was shown by

Thornton et al. [82] that the confining electric field gives relatively smooth side walls and the boundary scattering is predominantly specular. A magnetosize maximum is, therefore, only weakly established or completely missing. One, therefore, has to resort to alternative methods for the independent determination of the wire width, one of which will be briefly outlined in the following discussion.

4.2.2. *Weak Localization and Interaction Correction to the One-Dimensional Conductivity*

In Figure 16b, a magnetoresistance trace for very high applied back-gate voltage is shown. The number of subbands is now considerably reduced because of the low remaining electron density. At very low magnetic fields ($\leqslant$0.1 T), the differential magnetoresistance is seen to be negative for these strongly confined wires. The effect is also observed in a less pronounced form in the 140-V trace of Figure 16a and is attributed to the *suppression of* 1*D weak localization* by a magnetic field. Note that this effect has nothing to do with the reduced backscattering observed beyond the magnetosize peak ($B > 0.3$ T). In the following, we sketch only the very basic idea underlying the phenomenon of weak localization and indicate briefly how its investigation may serve as a tool for the determination of relevant wire parameters. A detailed and clear account of the physics of weak localization can be found in [25] and the references cited therein. Our very brief introductory argumentation follows closely the exposition at the beginning of Section 6 of [25].

Weak localization is assumed to occur in the diffusive transport regime because of the phase coherence of electron waves that are propagating or elastically backscattered by an impurity. It can be shown that elastic impurity scattering does not affect the phase coherence length l_ϕ and that, in order to achieve phase randomization, inelastic scattering events are necessary [72, 85]. Bergmann [86] has given an intuitive interpretation of the quantum mechanical weak localization effect. Its treatment within the framework of the path integral formalism, which forms the basis of this qualitative interpretation, is discussed in some detail in [87]. Consider an electron propagating along a narrow channel from a starting point $\mathbf{r}$ to the point $\mathbf{r}'$. Quantum mechanically, one may assign a probability amplitude A_i to each path (labeled by an index i) the electron can take between the two points. The probability of finding the electron at $\mathbf{r}'$ after a time t is then given by the absolute square of the coherent sum of these amplitudes

$$P(\mathbf{r}, \mathbf{r}', t) = \left|\sum_i A_i\right|^2 = \sum_i |A_i|^2 + \sum_{i \neq j} A_i A_j^* \tag{54}$$

If a sequence of elastic scattering events is considered that brings an electron back to its starting point, $\mathbf{r}$ and $\mathbf{r}'$ coincide and the preceding sum is taken over closed Feynman paths. It may then be split up into a sum over time-reversed pairs of amplitudes A^+ and A^-, assigned to clockwise and counterclockwise propagation along the same closed path. Because of time reversal symmetry, the two amplitudes are equal and if they are added coherently, they give a probability for returning to the starting point (after several phase-conserving elastic scattering events) of $|A^+ + A^-|^2 = 4|A|^2$. Without phase coherence, if scattering gives rise to a purely classical diffusive motion, the squared probabilities have to be added noncoherently. This would give for the same process a classical return probability of $2|A|^2$. In other words, quantum mechanical phase coherence yields a return probability that is twice the probability of the corresponding classical noncoherent diffusion process. It may, therefore, be expected that this will give rise to an additional contribution to the conductivity of a low-dimensional semiconductor system, which exhibits quite large phase coherence lengths at low temperatures. This contribution has to be added to the classically obtained result

$$g_{1D} = g_{\text{Boltzmann}} + \delta g_{1D}^{\text{loc}} \tag{55}$$

where the sign of δg_{1D}^{loc} will be *negative*, because an enhanced *return* probability reduces the resulting conductivity.

On the other hand, if a weak magnetic field is applied, time reversal symmetry is broken. There will be appreciable flux through any closed electron trajectory, which gives rise to an Aharonov–Bohm like phase shift acquired along the corresponding Feynman paths. This phase shift will be different for clockwise and counterclockwise propagation along the closed paths. Different possible orbits will enclose different flux and after averaging over all possible closed trajectories (or Feynman paths) phase coherence will be destroyed at sufficiently large magnetic fields. This, consequently, leads to an effective suppression of the weak localization corrections to the 1D conductivity. It has been shown by Altshuler and Aronov [88] (see also [25, 89, 90]) that this magnetic field dependence of the weak localization effect can be taken into account by adding to the 1D conductivity a term of the form

$$\delta g_{loc}^{1D} = -\frac{e^2}{\pi\hbar}\left(\frac{1}{l_\phi^2} + \frac{W^2}{3l_m^4}\right)^{-1/2} \qquad \text{for } l_m, l_\phi \gg W \gg l \tag{56}$$

Here, W is the width of the channel, l is the mean free path, $l_m = \sqrt{\hbar/eB}$ is the magnetic length, and $l_\phi = \sqrt{D\tau_\phi}$, where D denotes the diffusion constant, is the phase coherence length. A first-principles justification of Eq. (56) can be found in the review article of Beenakker and van Houten [25].

The preceding relation is derived under two assumptions. First, the magnetic length l_m has to be larger than the effective width of the channel; otherwise, the localization is of a 2D nature. This requirement is usually well established at the low magnetic fields for which the suppression of weak localization is observed. The second condition requires that the width W be larger than the electronic mean free path l, which is usually not the case for the conventional high-mobility GaAs–AlGaAs samples used to study the effect. It has been shown by Beenakker and van Houten [90] that in the opposite regime $l \gg W$ one has to take into account the effects of boundary scattering on the phase accumulated along a closed trajectory enclosing a magnetic flux (flux cancellation effect). Equation (56) has then to be replaced by

$$\delta g_{loc}^{1D} = -\frac{e^2}{\pi\hbar}\left(\left[\frac{1}{l_\phi^2} + \frac{W^2}{3l_m^4}\right]^{-1/2} - \left[\frac{1}{l_\phi^2} + \frac{W^2}{3l_m^4} + \frac{2}{l^2}\right]^{-1/2}\right) \tag{57}$$

The weak localization correction turns out to be much weaker in the case of an unstructured 2DEG (which also finds its expression in the W dependence of δg_{loc}^{1D}), so that the negative magnetoresistance at low field becomes more and more pronounced as the 1D confinement becomes stronger. This is what is observed in parts a and b of Figure 16, where a pronounced negative differential magnetoresistance is observed only for the highest back-gate voltages and, hence, the narrowest channels.

The magnetic field dependence of the weak localization correction can be exploited to obtain wire parameters such as the width W and the phase coherence length l_ϕ. One simply fits one of the expressions Eq. (56) or Eq. (57), chosen appropriately to the sample geometry, to a plot of $G(B) - G(0) = 1/R_{xx}(B) - 1/R_{xx}(0)$ versus magnetic field, using W and l_ϕ as adjustable parameters. This is done in a field range where $l_m > W$ and the suppression of weak localization is clearly observed in the magnetoresistance. This method was applied for the first time by Thornton et al. [91] for a 15-μm-long channel defined by a split gate on top of a GaAs–AlGaAs heterojunction. We reproduce their results, obtained for various temperatures below 1 K, in Figure 18. The solid curves are fitted according to Eq. (56). It has been discussed if the "dirty metal" expression Eq. (56) for δg_{loc}^{1D} is suitable in this case, because the estimated mean free path is larger than the channel width. However, the extracted values for the different characteristic lengths give a more or less consistent picture, if one assumes that the damage induced by the electron beam lithography [74] has led to a

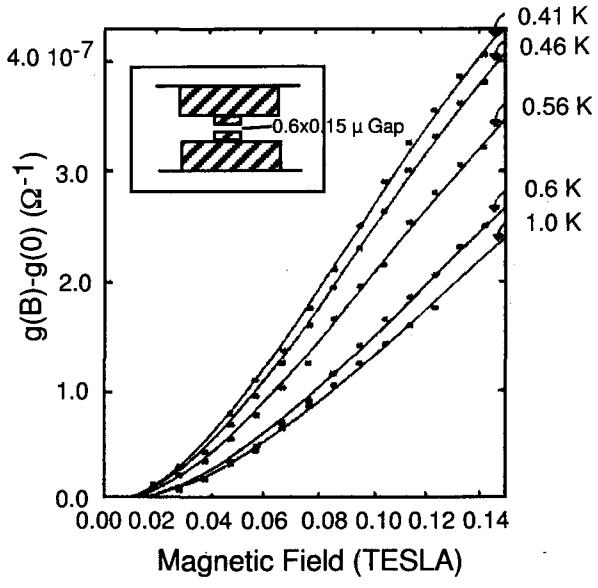

Fig. 18. Difference of magnetoconductance and zero-field conductance for a split-gate wire, measured at different temperatures. The sample geometry is shown in the inset. The solid lines stem from a two-parameter fit according to Eq. (56). (Source: Reprinted with permission from [91]. © 1986 American Physical Society.)

drastic reduction of the mean free path in the wire, compared to the value of the unstructured 2DEG. The values for the phase coherence length l_ϕ (200 nm or below) found from the fits shown in Figure 18 together with the condition $l_\phi \gg l$ underlying Eq. (56) would be consistent with a mean free path that certainly is not reduced below the estimated width of 50 nm, but could have reached the same order of magnitude.

An example of the application of the correct expression Eq. (57) to the low-field magnetoresistance in short and narrow channels defined by the shallow etching technique can be found, for example, in [92].

For the sake of completeness, it should be mentioned that there is another correction to the Boltzmann–Drude conductivity g_0 that is due to electron–electron interactions. Because both the weak localization and the interaction effects are relatively weak, they may to first order be taken into account as additive corrections to g_0:

$$g_{1D} = g_0 + \delta g_{1D}^{loc} + \delta g_{e-e} \tag{58}$$

The interaction correction has been estimated to be [93]:

$$\delta g_{e-e} = -\alpha \frac{e^2}{\pi\hbar}\sqrt{\frac{\hbar D}{2k_B T}} \tag{59}$$

which is valid if the thermal length $\sqrt{\hbar D/k_B T} < W$. α is a coupling constant that depends on the electron density and on the screening length in the system under consideration. Its magnitude is usually of order unity and in the commonly encountered experimental situations its sign is positive [25]. Electron–electron interactions thus reduce the conductivity of a narrow channel. The localization correction can be easily distinguished from the interaction correction in a magnetic field. As is obvious from Eq. (56) or Eq. (57), the former is completely suppressed already at very weak fields, whereas the latter is almost unaffected in this field regime. Theoretical considerations indicate that there is a small contribution to δg_{e-e} which is also sensitive to weak magnetic fields. But the main contribution to the conductivity correction reveals its magnetic field dependence only in strong fields. Usually, the weak-field-dependent part of δg_{e-e} is neglected, which makes the distinction between

the two corrections feasible [94]. If one wishes, one may use the T dependence of the interaction correction, determined from the magnetoconductance after subtraction of the weak localization correction, to estimate the diffusion constant D of the narrow channel [74, 91].

4.3. Magnetophonon Resonances in Quantum Wires

In 1961, Gurevich and Firsov [95] discovered that the quantization into Landau levels at high magnetic fields should lead to resonant longitudinal-optical (LO) phonon scattering of electrons between these equidistant Landau levels. As the LO phonons are assumed to be dispersionless in the interesting k-space region, resonant scattering between Landau levels is expected whenever the phonon energy equals an integer number of Landau levels:

$$\hbar\omega_{\mathrm{LO}} = N\hbar\omega_{\mathrm{c}} \tag{60}$$

This so-called magnetophonon effect has been shown to result in an oscillatory behavior of the magnetoresistance at temperatures high enough to ensure a sufficient population of the phonon states (usually at $T \geqslant 100$ K). Since then, magnetophonon resonances (MPRs) have been observed in a variety of semiconductor systems (for a review of the work until 1975, see [96]). In the bulk, MPRs have become a standard method for the determination of effective masses [97, 98] and proved to be a useful tool for the investigation of the conduction band nonparabolicity in ternary compounds for temperatures up to 400 K [99, 100]. After the first detection of MPRs in 2D systems [101], a wealth of phenomena was investigated also in 2D electron gases using the magnetophonon effect. Besides the determination of effective masses, an important subject that could be investigated using the magnetophonon effect in 2DEGs was the influence of the reduced dimensionality on the electron-phonon interaction [102–104].

As discussed previously, in quantum wires the energy spacing of magnetoelectric hybrid levels does not only depend on the magnetic field strength, but also on the 1D subband spacing induced by the lateral confinement. If, for example, parabolic confinement is assumed, the energy levels are calculated according to $E_n(B) = \hbar\omega(n + \frac{1}{2}) = \hbar\sqrt{\omega_{\mathrm{c}}^2 + \omega_0^2}(n + \frac{1}{2})$. This leads to a modification of the magnetophonon resonance condition Eq. (60) where now $\hbar\omega$ has to be used instead of $\hbar\omega_{\mathrm{c}}$. As a consequence, the magnetic field positions of the magnetophonon resonances should be shifted to slightly lower fields compared to the 2D case. Because this shift depends on the subband energy $\hbar\omega_0$, it is expected that MPRs can be used for subband spectroscopy of 1D quantum channels.

After a brief résumé of the relevant theoretical work on MPRs in quantum wires, it will be shown in the following that MPRs are indeed useful for the experimental determination of 1D subband energies. The obtained results for the sublevel spacings turn out to be different from the values extracted from low-temperature magnetic depopulation investigations. We discuss the reasons for this difference and show that it gives direct qualitative information on the shape of the wire potential.

4.3.1. Magnetophonon Resonances in Quantum Wires: Theory

The first theoretical investigation of MPRs in quasi one-dimensional electron systems was performed by Vasilopoulos et al. [105]. To determine the contribution to the magnetoconductivity due to electron-LO phonon scattering, they started from a quantum transport equation of the form

$$\sigma_{xx} = \frac{e^2}{2k_{\mathrm{B}}TV_0}\sum_{\zeta,\zeta'}\langle n_\zeta\rangle\big(1 - \langle n_{\zeta'}\rangle\big)W_{\zeta,\zeta'}\big(\langle\zeta|y|\zeta\rangle - \langle\zeta'|y|y\zeta'\rangle\big)^2 \tag{61}$$

which follows from a modification of the formalism developed to describe the magnetophonon effect in 2D systems [106]. Here, $\langle n_\zeta\rangle$ denotes the Fermi–Dirac distribution

function, y is the coordinate along the wire axis, and $W_{\zeta,\zeta'}$ is the usual Fröhlich-type transition probability between the two states ζ and ζ'. The $|\zeta\rangle$ denote the one-particle states of the 1D confined electrons. For their calculation, it is assumed that the confinement in the growth direction can be separated from the lateral confinement and that the latter is well described by the usual harmonic oscillator potential. The z component $\varphi_0(z)$ of the wave function is approximated by the well-known Fang–Howard trial functions $\varphi_0(z) = b_0^{3/2} z \exp(-b_0 z/2)$. Thus,

$$\langle r|\zeta\rangle = \psi_n\left(\sqrt{m\omega/\hbar}(x-\bar{x})\right) 1/\sqrt{L} \exp(ik_y y)\varphi_0(z)$$

where the harmonic oscillator functions, given in the paragraph following Eq. (11), have been used.

It turns out that in the case of relatively weak confinement ($\omega_0 < \omega_c$) σ_{xx} may be calculated analytically. The LO phonon–mediated magnetoconductivity consists of a contribution falling off monotonically with increasing B and an additional oscillatory part σ_{xx}^{osc}, which is given by [105]:

$$\sigma_{xx}^{\text{osc}} \propto \left(\frac{\omega_c}{\omega}\right) \frac{N_s^{1D}\tilde{l}_B^2}{k_B T \hbar\omega} \frac{\cos(2\pi\omega_{LO}/\omega) - \exp(-2\pi\Gamma_N/\hbar\omega)}{\cosh(2\pi\Gamma_N/\hbar\omega) - \cos(2\pi\omega_{LO}/\omega)} \tag{62}$$

A plot of this relation is shown in Figure 19. The total magnetoconductivity, including the monotonic part, is obtained from Eq. (62) by replacing the numerator $\cos(2\pi\omega_{LO}/\omega) - \exp(-2\pi\Gamma_N/\hbar\omega)$ by $\sinh(2\pi\Gamma_N/\hbar\omega)$. ω is again the combined "renormalized" frequency $\omega = \sqrt{\omega_0^2 + \omega_c^2}$, Γ_N is the magnetic field–dependent width of the Nth magnetoelectric hybrid level. $\tilde{l}_B^2 = \hbar/m^*\omega$ is a modified magnetic length and, finally, ω_{LO} is the frequency of the LO phonons, which is assumed to be given by its bulk value.

In the case of weak confinement the oscillatory part of the magnetoconductivity is thus described by a series of exponentially damped cosine oscillations just as it is well known from the magnetophonon theory in the bulk and in 2D systems [107, 108]. Whenever the resonance condition $\hbar\omega_{LO} = \nu\hbar\omega$ with integer ν is satisfied, a maximum in the magnetoconductivity is observed (cf. Fig. 19). The main effect of a weak 1D confinement on the magnetoconductance is thus simply a shift of the resonant maxima in σ_{xx} to smaller magnetic fields as compared to the resonance condition [Eq. (60)], valid for bulk and 2D systems.

This first investigation of the 1D magnetophonon effect has been followed by several improvements of the theory, mainly concerning the extension to the case of arbitrary confinement strength. Mori et al. [109] pointed out that, in the case of strong confinement, the influence of the confining potential on the electron motion may not be neglected. Employing a Green's function approach to the general Kubo formula and using the same parametrization of the confinement as before, they were able to show that, in addition to the weak confinement expression already given by Vasilopoulos et al. [105], there is a second, qualitatively different contribution to the 1D magnetoconductance. To understand the difference between the two contributions, one may resort to a simple classical picture. Consider a wide, weakly confined quantum wire. In sufficiently strong magnetic fields, a considerable part of the electrons will be in Landau level–like states. Classically, they are localized on circular cyclotron orbits. LO phonon scattering will lead to hopping motion between these localized orbits and, therefore, to an enhancement of the electron mobility. This is why maxima occur at resonance in the magnetoconductance as indicated in Figure 19. On the other hand, if the confinement is strong and the wire narrow, a considerable fraction of electrons will be in edge states corresponding to skipping orbits propagating along the wire. The LO phonons will scatter electrons off their propagating modes, thereby reducing their mobility. This is expected to lead to resonant minima in the magnetoconductance. In Figure 20, the second derivative of σ_{xx}, calculated according to the model of Mori et al. [109], is plotted for the two cases of low and high confinement energy.

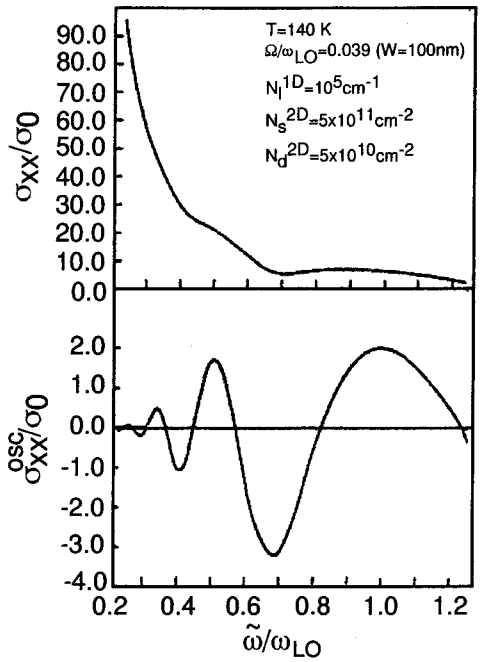

Fig. 19. Top: Magnetoconductivity in units of $\sigma_0 = e^2/hk_{\mathrm{LO}}$ as a function of the combined frequency ω ($=\tilde{\omega}$ in the figure). The parameters used in the calculation are also shown. Ω is the confining frequency of the parabolic potential; $N_{\mathrm{d}}^{2\mathrm{D}}$ is the depletion charge density, needed for the calculation of Γ_N. Bottom: Oscillatory part $\sigma_{xx}^{\mathrm{osc}}$ according to Eq. (62). (Source: Reprinted with permission from [105]. © 1989 American Physical Society.)

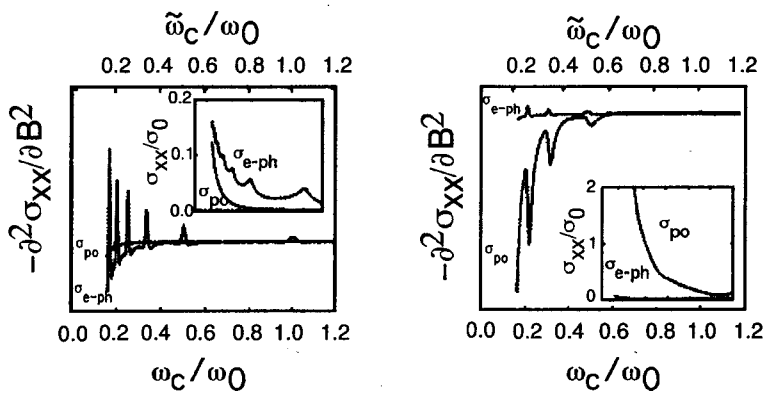

Fig. 20. Calculated second derivative of the two contributions to the magnetoconductivity for weak (left) and strong (right) confinement. σ_{po} denotes the contribution corresponding to the skipping motion of electrons along the wire boundaries, $\sigma_{\mathrm{e-ph}}$ is due to electrons without interaction with the channel boundaries. The traces are calculated for $T = 100$ K, a level broadening Γ of 1 meV, and a confining frequency of the parabolic potential of 1 meV (left) and 5 meV (right). The insets show the corresponding underived quantities in units of $\sigma_0 = ne^2/\alpha\omega_0 m^*$, α being the Fröhlich coupling constant. In the figure, ω_0 is the LO phonon frequency, ω_{c} is the cyclotron frequency, and $\tilde{\omega}_{\mathrm{c}}$ is again the combined frequency of the magnetoelectric hybrid levels. (Source: Reprinted with permission from [109]. © 1992 American Physical Society.)

These results have been confirmed theoretically by Ryu and O'Connell [110, 111], who used a different quantum transport approach [112] to describe the influence of resonant LO phonon scattering on the magnetoconductance. Their model calculations also assume a parabolic confinement potential and again give two contributions to the magnetoconduc-

tivity, the first being almost identical to the result of Vasilopoulos et al. [105]. The second term was attributed to a "nonhopping" contribution to the electron conduction, which is qualitatively reminiscent of Mori's skipping orbit motion term.

4.3.2. Magnetophonon Resonances in Quantum Wires: Experimental Results

Regarding the nature of the magnetic depopulation experiments discussed previously and the methods of calculating the subband spacing from the resulting Landau plots, it is clear that it is necessary to have a sufficient number of occupied subbands in order to obtain reliable results for E_0 and n_{1D}. It is the main advantage of the magnetophonon method of subband spectroscopy that the number of occupied subbands is largely irrelevant for its application. It is, therefore, a transport characterization technique for quantum wires with low carrier densities or relatively large subband spacing. It could even be used to characterize quantum channels in or at least very near to the quantum limit where only one 1D subband is occupied (provided, of course, the subband spacing is substantially smaller than $\hbar\omega_{LO}$).

However, it has been shown experimentally [103] and theoretically [108] in the case of MPRs in 2D systems that the oscillation amplitude of the magnetoresistance strongly depends on various scattering mechanisms such as scattering from charged donor impurities. These scattering mechanisms influence the broadening of the Landau levels or magnetoelectric hybrid levels in 2D and 1D, respectively. The experimental results [113, 114] indicate that if the influence of charged donors is reduced by low total doping and large spacer layers of the underlying heterostructures, a much more pronounced magnetoresistance oscillation is obtained at high temperatures. Consequently, the low-density regime is the natural field of application of the magnetophonon effect for the characterization of quantum wires both because this regime is not readily accessible to magnetic depopulation measurements and because the magnetophonon effect is more easily resolved. On the other hand, one has to be aware of the considerable amount of unwanted scattering sources that are introduced by any nanofabrication process. The shallow etching method, in particular, introduces considerable side-wall roughness in the narrow channels. This, in turn, will reduce the amplitude of the high-temperature magnetoresistance oscillations and be disadvantageous for their resolution.

For this reason the following experiments discussed briefly were conducted on a set of quantum wires obtained by very shallow etching on a low density, high mobility heterostructure. The most prominent features of the sample material used in the experiments are the low integral doping and the relatively wide spacer layer. Due to these features very shallow etching is sufficient to obtain appreciable 1D confinement, keeping the amount of sidewall roughness within tolerable limits. Some details of the sample structure are given in the caption of the following Figure 21. This figure shows a set of typical magnetoresistance traces, recorded at $T = 100$ K and revealing pronounced oscillatory structure due to the magnetophonon effect.

Figure 22 shows two examples of the oscillatory part of the magnetoresistance ΔR_{osc}, which were obtained from similar data as those shown in Figure 22 after subtraction of a monotonous background resistance. The lower trace corresponds to a sample (labeled "1" in the following), where slightly deeper etching is done in comparison to sample "2". The two samples are otherwise identical. The $R(B)$ traces shown in Figure 21 were obtained for sample "2". Note that for the more shallow wires of sample "2" the oscillation amplitude is almost an order of magnitude greater than for sample "1". On the other hand, the oscillation of sample "1" does not seem considerably broadened as compared to the ΔR_{osc} of the other sample. The most interesting feature of the traces of Figure 22 is that they seem to be "phase-shifted" with respect to each other.

This phase shift together with the large reduction of the oscillation amplitude observed for sample "1" indicates that for the more strongly confined wires of this sample one en-

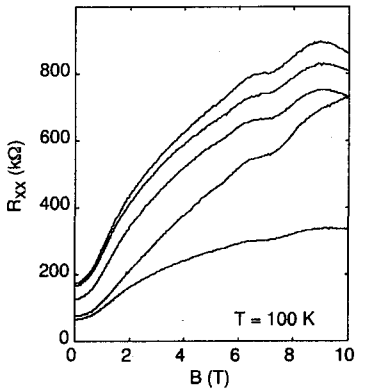

Fig. 21. Typical magnetoresistance data measured on an array of shallow etched quantum wires at $T =$ 100 K. The various traces correspond to sample "2" for different electron densities (see text). The underlying heterojunction consists of 100 Å GaAs cap undoped, followed by 300 Å $Al_{0.4}Ga_{0.6}As$, doped to 2×10^{18} cm^{-3}, and 600 Å undoped $Al_{0.4}Ga_{0.6}As$ spacer.

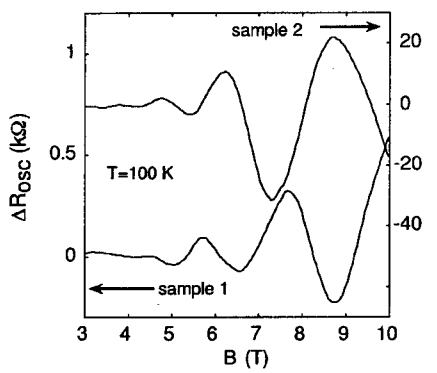

Fig. 22. Oscillatory part of the magnetoresistance ΔR_{osc} plotted for two different samples. The curves are obtained after subtraction of the monotonic background from the $R(B)$ traces, some examples of which are shown in Figure 21. Sample "1" (bottom curve) was slightly deeper etched than sample "2" (top curve). This slight increase of the etching depth leads to a reduction of the oscillation amplitude by almost an order of magnitude as well as to a drastic "phase shift" of the oscillation. Note the different y-axis scales valid for the two traces.

counters a situation where there is a crossover between the two transport regimes discussed in the previous section. For sample "1" scattering off skipping orbits seems to be the dominant source that influences the magnetoresistance. Therefore one observes resistance *maxima* at resonance whereas the other sample "2" displays minima at resonance. It turns out that this assumption leads to a consistent explanation of the features of ΔR_{osc} observed in Figure 22.

To analyze the experimental data quantitatively, one assumes a parabolic confinement $V(x) = \frac{1}{2}m^*\omega_0^2 x^2$ for the quantum wire. Again, x is the direction perpendicular to the wire and m^* is the electron effective mass (frequently called the *polaron mass* in the context of MPR). In a perpendicular magnetic field, the bottoms of the magnetoelectric hybrid levels are quantized according to $E(B) = \hbar\omega_{\text{eff}}(n + \frac{1}{2})$ with $\hbar\omega_{\text{eff}} = \sqrt{(\hbar\omega_c)^2 + E_0^2}$ and $E_0 = \hbar\omega_0$ being the 1D subband spacing.

As discussed before, one assumes that the weak confinement case is valid for sample "2". The resonance condition

$$N\hbar\omega_{\text{eff}} = \hbar\omega_{\text{LO}} \tag{63}$$

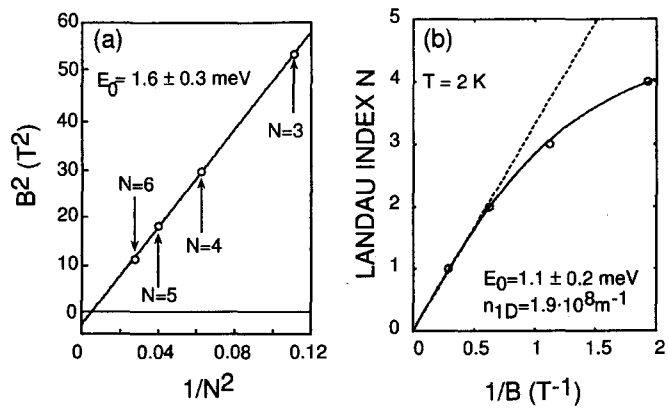

Fig. 23. (a) Plot of the squared magnetic field position of the resonance minima in $\Delta R_{\rm osc}$ versus $1/N^2$, obtained from the data shown in Figure 22 for sample "2". The corresponding value of the subband spacing obtained from the intersection of the resulting straight line with the B^2-axis is 1.6 meV. (b) Landau Plot obtained from magnetic depopulation data for the same sample and electron density as in (a). The solid line represents a fit using a harmonic oscillator model, which gives a subband spacing of 1.1 meV.

thus applies to the minima in the magnetoresistance oscillation $\Delta R_{\rm osc}$ [109]. For sample "1" this condition is related to the resonant maxima in $\Delta R_{\rm osc}$.

Using $E_{\rm LO} = \hbar\omega_{\rm LO}$, this resonance condition may be rewritten as follows:

$$B^2 = \left(\frac{m^*}{e\hbar}\right)^2 \frac{E_{\rm LO}^2}{N^2} - \left(\frac{m^*}{e\hbar}\right)^2 E_0^2. \tag{64}$$

According to this equation, the B^2 values, corresponding to the resonant extrema in $\Delta R_{\rm osc}$, plotted versus $1/N^2$ should lie on a straight line. Its slope is a measure of the effective mass of the confined electrons, whereas its intersection with the B^2-axis is proportional to the squared subband spacing E_0. It should be emphasized that this simple relationship is only valid if the confining potential can be approximated by the harmonic oscillator form given above.

Figure 23a shows the positions of the resonant minima in $\Delta R_{\rm osc}$ taken from the upper curve in Figure 22 (corresponding to sample "2"). The solid straight line stems from a fit of the data according to Eq. (64), using the LO phonon energy for bulk GaAs, $E_{\rm LO} = 36.6$ meV. The simple parabolic model potential is seen to describe the experimental data quite well. As parameters of the fit one obtains a magnetophonon effective mass of $(0.069 \pm 0.007)m_e$ and a subband spacing E_0 of (1.6 ± 0.3) meV. The value for E_0 can now be compared to the corresponding low temperature value, obtained from a magnetic depopulation measurement on the same sample at $T = 2$ K. The resulting Landau plot is shown in Figure 23b. The deviation of the plot from a straight line clearly shows the 1D behavior of the laterally confined electrons. The solid line interpolates between calculated points fitted to the data according to the model of Berggren et al. [75] (see Section 4.1.1), which also assumes a parabolic confinement potential. The resulting subband spacing is $E_0 = (1.1 \pm 0.2)$ meV, which is somewhat smaller than the corresponding high temperature subband energy.

When one changes the carrier density of the quantum wires, for example by illuminating the samples with a red light emitting diode, one obtains the subband spacing as a function of the 1D carrier density as shown in Figure 24. Solid circles correspond to data obtained from an analysis of the MPR signal of sample "1". Open diamonds represent the same data for sample "2". The open circles were obtained from magnetic depopulation experiments on sample "2". Figure 21 shows a set of typical magnetoresistance traces measured for varying carrier density of sample "2". To arrive at the plot of Figure 24 the electron density

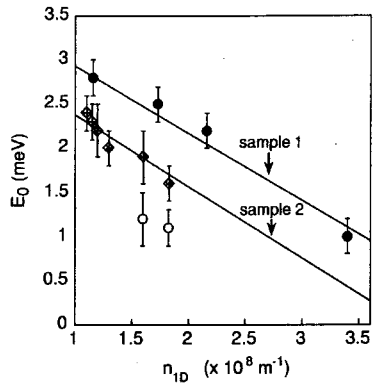

Fig. 24. Subband spacing as a function of the 1D electron density for the two samples considered in the text. Solid circles: Magnetophonon results for sample "1". Open diamonds: Magnetophonon results for sample "2". Open circles: Subband energies obtained by magnetic depopulation from sample "2". The increase of E_0 with decreasing n_{1D} is attributed to screening effects, as discussed in [115].

was determined from the linear part of the low temperature Landau plots according to Eq. (49). Details of the experimental procedure can be found in [114] and [115]. Note that in order to determine the low temperature subband spacing from the magnetic depopulation data it is necessary that the number of occupied subbands in the wires is large enough for the usual evaluation methods to be applicable. This is the case only for sample "2" at relatively high carrier densities. In all cases where a direct comparison was possible, the low temperature subband spacing turned out to be systematically smaller than the high temperature value by 30–50%.

Before giving an explanation of this apparent difference, it is worth mentioning that both in the theoretical and the experimental analysis the LO photon energy of 36.6 meV of bulk GaAs is assumed. Note that there is experimental evidence that the presence of the GaAs–AlGaAs interface leads to a modification of the photon energies. From a combination of cyclotron resonance and magnetophonon resonance experiments on various GaAs–AlGaAs heterojunctions, Brummell et al. [102] found that the LO phonon energy appears to be reduced by approximately 5% to 34.8 meV. However, this possible slight modification of the LO phonon energy has no influence on the above analysis. The reason for this insensitivity is that the statistical error of the fit in Figure 23a is, in spite of the excellent correlation to the data, not very much smaller than approximately 10%. This experimental error far exceeds that introduced by any uncertainty in the phonon energies.

To explain the difference in the E_0 values obtained at low and high temperatures, respectively, we first note that the thermal rearrangement of the electrons among the 1D sublevels at elevated temperatures cannot account for the observed difference. If this rearrangement is considered in a self consistent calculation, it can be shown [116] that it will indeed lead to a slight enhancement of the subband spacing. However, these changes in E_0 are small (less than 10%) unless one assumes considerable recharging and reordering of the electrically active impurities, which is not a very realistic assumption.

It rather turns out that the observed difference can be consistently explained if one takes into account that the actual confinement potential for shallow etched quantum wires is not exactly parabolic but sinusoidal. To demonstrate this, we model the experimental situation by choosing a one-dimensional potential of the form $V(y) = V_{\mathrm{mod}}(\cos(2\pi y/w) + 1)/2$ that best approximates the self-consistently calculated potential for a shallow etched wire (cf. Fig. 6). Using this model potential, we calculate both the magnetoelectric confinement and the corresponding energy states as a function of magnetic field, simply using the one-dimensional Schrödinger equation and the discretization schemes described in Section 2.

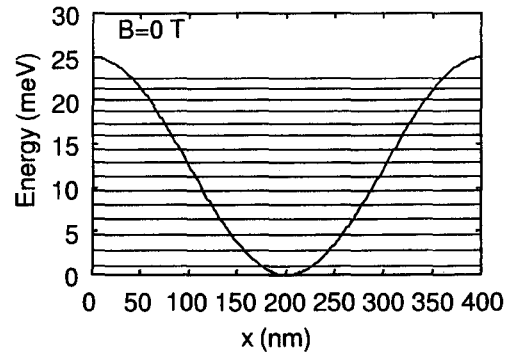

Fig. 25. Cosine-shaped model potential with a period of 400 nm and a modulation amplitude of 25 meV. The energy levels are calculated for zero magnetic field. Because of the shape of the potential the subband spacing decreases with increasing energy.

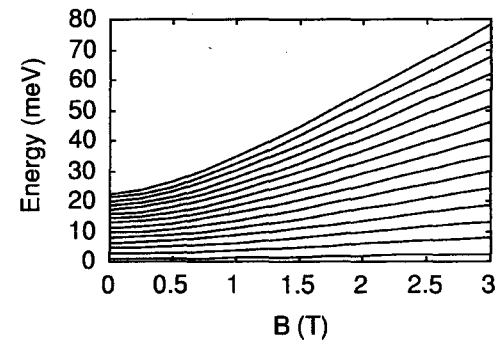

Fig. 26. Magnetoelectric subband edges as a function of magnetic field calculated for the cosine potential shown in Figure 25.

Figure 25 shows the energy levels for a cosine potential with $V_{\text{mod}} = 25$ meV and a period of 400 nm for zero magnetic field. To calculate their magnetic field dependence, one adds the magnetic confinement according to

$$V(y) = V_{\text{e}}(y) + V_{\text{m}}(y) = \frac{V_{\text{mod}}}{2}\left[\cos\left(\frac{2\pi}{w}\right) + 1\right] + \frac{1}{2}m^*\omega_{\text{c}}^2(x - x_0)^2 \qquad (65)$$

To cover the essential features of a magnetophonon or magnetic depopulation experiment, it is sufficient to consider the positions of the sublevel bottoms, that is, to calculate the magnetic field dependence of the 1D subbands setting the center coordinate $x_0 = 0$. The resulting B dependence of the hybrid level energies is shown in Figure 26.

Two main features are interesting. First, the subband spacing of the high-lying subbands is obviously smaller than that of the low-lying levels of the cosine potential. This is important when considering the information on the subband spacing E_0 obtained from the magnetic depopulation method. E_0 is found from that part of the Landau plot where it deviates from a straight line. That is, the main information is obtained from those high-lying subbands that are depopulated at low magnetic fields. If the Landau plot is fitted with a model curve calculated from a simple parabolic potential (Section 4.1.1), one has to be aware that this will only reproduce the subband spacings for the high-lying levels.

Numerically, one can simulate this situation by determining the magnetic field positions, where the magnetoelectric subbands cross the Fermi level. The resulting Landau plot is then evaluated using the simple harmonic oscillator model. In fact, performing this procedure for the model potential of Figure 25, we obtain an energy spacing of 1.35 meV, which excellently reproduces the subband spacing of the high-lying subbands (1.3 meV)

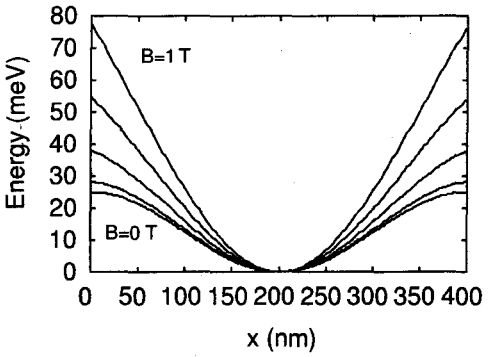

Fig. 27. Sum of the electrostatic and magnetic confinement potentials in the range between $B = 0$ T and $B = 1$ T, plotted in steps of 0.25 T. The parameters of the cosine potential are the same as in Figure 25.

in the cosine-shaped potential. Note that, in the numerical simulation of the magnetic depopulation experiment, the Fermi level has to be calculated as a function of magnetic field, taking into account the one-dimensional density of states. Because this is easily achieved only for the harmonic oscillator potential but computationally very expensive for an arbitrarily shaped electrostatic potential, one may assume an approximately constant Fermi level at low magnetic fields. As can be seen from Figure 14, this assumption is justified at low magnetic fields. The oscillations of the Fermi level are relatively small there and the error introduced by assuming a constant E_F will be negligible.

We now consider the situation encountered in a magnetophonon resonance experiment. Because of the strong damping of the magnetophonon (MP) magnetoresistance oscillations with decreasing magnetic field, it is clear that, in contrast to the magnetic depopulation experiment, the relevant information is drawn from the structure in $R_{xx}(B)$ observed at *high* magnetic fields ($B > 4$ T). As can be seen from Figure 27, the magnetic confinement strongly dominates over the electrostatic one already at fields of 2 T. The resulting total potential is parabolic to a good approximation with the nonparabolic parts of the superposed electrostatic potential entering only as a weak perturbation. At the high magnetic fields at which MP resonances are observed (cf. Fig. 22), only the lowest subbands are occupied. Because the transition probability between the subbands at elevated temperatures is weighted by a Boltzmann factor, resonant LO phonon scattering mainly occurs between the lowest subbands. Hence, what is probed by the magnetophonon effect is the subband spacing of those levels lying near the bottom of the cosine confinement potential, which is larger than that of the high-lying levels. Quantitatively, we demonstrate this by the following considerations. In analogy to the previous simulation of the magnetic depopulation experiment, we calculate those magnetic field positions where an integer number (N) of subbands equals the LO phonon energy (36.6 meV) and plot their squared values against the inverse-squared N (see Fig. 28). The solid straight line in the figure is a fit according to Eq. (64), ignoring all nonparabolic contributions to the electrostatic confinement. As can be seen from Figure 28, the parabolic model fits perfectly with the simulated data points. The values for the effective mass and the subband spacing obtained from the fit are $m^* = 0.070$ and $\Delta E = 2.0$ meV, respectively. The latter reproduces almost exactly the subband spacing at the bottom of the underlying cosine potential.

To summarize these considerations, one may state that magnetic depopulation experiments always probe the subband energies at the Fermi energy, whereas magnetophonon resonance experiments are sensitive to the sublevels near the bottom of the confinement potential. This not only explains the experimentally observed difference between the energy values determined by the two methods. It also shows that the combination of the two methods provides in a simple manner direct information on the actual shape of the underlying confinement potential, in that it allows us to decide immediately if the potential is

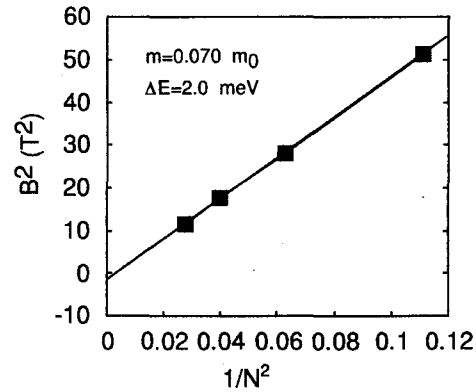

Fig. 28. Simulated magnetophonon resonance experiment for a wire with cosine-shaped confinement. The squares correspond to those magnetic fields, where an integer number of the low-lying subbands fits the LO phonon energy. The straight line stems from a fit using a simple harmonic oscillator potential. The subband spacing extracted from the intersection of the straight line with the B^2 axis is $\Delta E = 2.0$ meV. This value reproduces the subband spacing at the bottom of the cosine potential almost exactly. The mass value obtained from the slope of the line is $m^* = 0.070 m_e$.

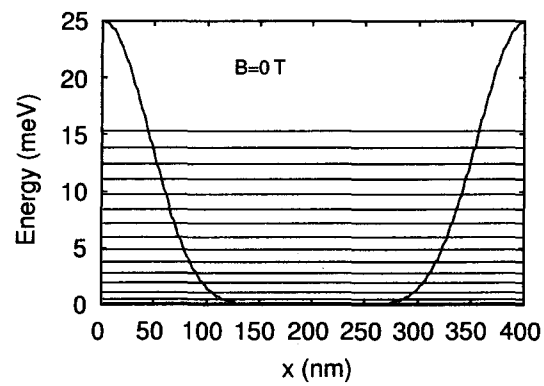

Fig. 29. Confinement potential according to Eq. (66) plotted together with the calculated energy levels at zero magnetic field.

cosine or square well like. Consider as an example a potential calculated according to

$$V(y) = \frac{V_{\text{mod}}}{2}\left(\cos\left(\frac{2\pi y}{w}\right) + 1\right)^4 \tag{66}$$

which is shown in Figure 29 together with the corresponding subbands. This model potential exhibits a flat bottom and has relatively steep side walls as is typical for a split-gate wire at high carrier densities. Inversely to the previous case of a simple cosine potential, the upper subbands now have a higher spacing than the low-lying ones. Again, the simulation of the magnetic depopulation and the magnetophonon resonance experiment shows that the former will give the higher subband spacing of the top levels, the latter that of the bottom levels.

Finally, it is worth noting that the estimate of the 1D carrier density from a magnetic depopulation experiment should be interpreted with some care. The application of the standard parabolic model to the interpretation of a Landau plot also yields the 1D carrier density of the wire [cf. Eq. (49)]. If the "true" confinement is sinusoidal, however, the so-obtained n_{1D} slightly underestimates the actual value, because the procedure leading to Eq. (49) presupposes that the subband spacing appropriate for the high-lying levels is valid for all occupied subbands.

5. WEAKLY AND STRONGLY MODULATED SYSTEMS

A practical problem that sometimes arises when one fabricates an array of shallow etched quantum wires is that one needs to know whether one has really achieved a system of separated quantum wires or only imposed a periodic potential modulation on the underlying 2D electron gas. Also, the variation of the potential amplitude with varying etching depth or gate voltage is sometimes of interest for theoretical or technological reasons. As will be shown in the following, the magnetoresistance measured *perpendicular* to the equipotential lines of a lateral potential modulation contains a wealth of information on the relevant potential parameters. Depending on whether the modulation is only weak, that is, the potential amplitude V_0 is much smaller than the Fermi energy, or whether V_0 is no longer negligible in comparison to E_F, different characteristic features of the magnetoresistance can be used for the characterization of the potential. This will be the topic of the present section. Because modulated systems are of great interest not only from the point of view of potential properties, they have been extensively investigated and reviewed in the past (see, e.g., [84]). We will consider these systems only under the aspect of obtaining insight into the shape and magnitude of the periodic potential. In order to do this, we restrict our discussion to the very simplest (semiclassical) model considerations commonly employed for the explanation of the observed effects.

We start with the case of a weakly modulated system. A weak potential modulation can be realized by different techniques such as *very* shallow etching, by application of small voltages to a grating gate, or even by brief illumination with two interfering laser beams [19]. The magnetoresistance $\rho_\perp$ measured perpendicular to the equipotentials of the so-introduced modulation exhibits a number of characteristic low-field oscillations (see Fig. 30). The oscillations are periodic in $1/B$, just as the Shubnikov–de Haas oscillations of the unstructured 2DEG, but, as the different field scale indicates, of an obviously different origin. After the first observation of these oscillations [19], which have later on been termed *commensurability oscillations*, several equivalent models were developed to explain their origin [117–120]. In the following, we give a very brief account of the semiclassical model of Beenakker [117], because it facilitates an intuitive understanding of the underlying physics. Its basic ideas can also be used to explain the special features occurring if the modulation height is gradually increased.

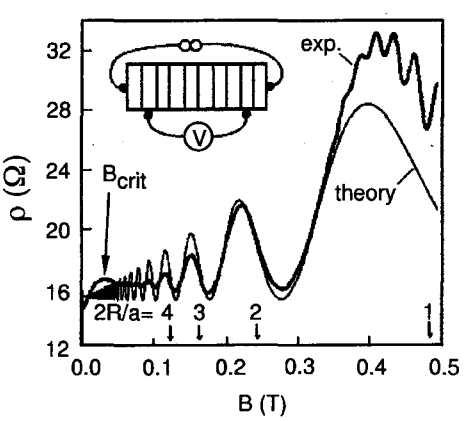

Fig. 30. Longitudinal magnetoresistance of a weakly modulated 2DEG with current flowing perpendicular to the equipotential lines (see inset). The thick solid line represents data from Weiss et al. [19], showing commensurability oscillations below $B = 0.4$ T and the onset of Shubnikov–de Haas oscillations for $B \geqslant 0.4$ T. The thin solid line is calculated from the semiclassical guiding center drift resonance model of Beenakker [117]. The vertical arrows indicate those magnetic field values where the cyclotron diameter matches the period of the grating. The commensurability oscillations are phase shifted relative to these values by $\pi/4$. B_{crit} is the critical field for magnetic breakdown and will be discussed later in this section. (Source: Reprinted with permission from [25].)

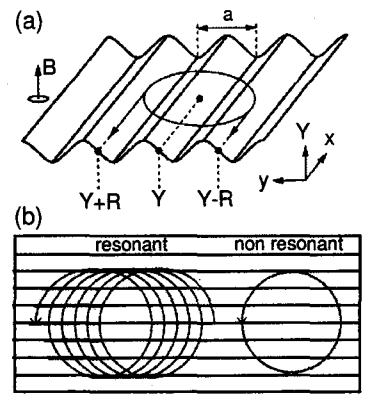

Fig. 31. Illustration of the electron motion in a weakly modulated 2DEG with a magnetic field applied perpendicular to the electron gas. (a) Potential landscape with cyclotron orbit. (X, Y) are the coordinates of the orbit center (guiding center); $Y \pm R$ are the extremal points, where the orbit center acquires a net $\mathbf{E} \times \mathbf{B}$ drift. (b) Numerically calculated cyclotron orbits in a sinusoidal potential. Horizontal lines indicate the equipotential lines of the periodic modulation. The figure shows a resonant orbit at $2R/a = 6.25$ and a nonresonant one at $2R/a = 5.75$ with negligible drift. (Source: Reprinted with permission from [25].)

Figure 31 shows the classical cyclotron trajectory of an electron moving in a weak periodic potential modulation with a magnetic field applied perpendicular to the plane of the 2DEG. (X, Y) denotes the center of the cyclotron orbit and $R = \hbar k_F/eB$ is the cyclotron radius. Because the modulating potential is assumed to be very weak, it can be considered as a small perturbation that leaves the cyclotron orbits essentially undistorted. The simultaneously present electric ($\mathbf{E} = -\nabla V_{\text{mod}}(y)$) and magnetic fields classically give rise to an $\mathbf{E} \times \mathbf{B}$ drift of the center of the otherwise unaffected cyclotron orbit. Because at low magnetic fields the electronic orbit extends over many periods of the potential modulation, only the drift acquired at its extremal points $Y \pm R$ will be essential. This is depicted in Figure 31b. If the position and radius of the orbit are such that the drift acquired at opposite extremal points adds up constructively, one speaks of a guiding center drift resonance. Off resonance, the drift acquired at one extremal of the orbit will cancel that at the other extremal, leading to zero net drift. At resonance, the electron drift, which is directed parallel to the equipotential lines, will lead to a maximum in $\rho_\perp$. An off-resonant, stationary orbit accordingly corresponds to a resistance minimum. This qualitatively accounts for the oscillatory behavior shown in Figure 30. The preceding ideas can be integrated into a rigorous solution of the semiclassical Boltzmann equation. If the strength of the potential modulation is characterized by the parameter $\varepsilon \equiv e\overline{V}/E_F$, the magnetoresistance is then obtained to second order in ε:

$$\frac{\rho_{yy}}{\rho_0} = 1 + \frac{1}{2}\left(\frac{2\pi}{a}\varepsilon l\right)^2 \frac{J_0^2(2\pi R_c/a)}{1 - J_0^2(2\pi R_c/a)} \tag{67}$$

Here, ρ_0 is the usual semiclassical expression for the longitudinal magnetoresistivity, a is the period of the potential modulation, and $l = v_F\tau$ is the mean free path. J_0 is a Bessel function. The exact analysis gives the condition $2R_c/a = n - 1/4$ for a resistance minimum and $2R_c/a = n + 1/4 - \text{order}(1/n)$ for a maximum. In the limit $2\pi(R_c/a) \gg 1$, Eq. (67) can be shown to reduce to the following frequently quoted expression for $\rho_\perp$ [117]:

$$\rho_\perp = \rho_0\left(1 + 2\varepsilon^2\left(\frac{l^2}{aR_c}\right)\cos^2\left(2\pi\frac{R_c}{a} - \frac{\pi}{4}\right)\right) \tag{68}$$

Basically, the same result can also be derived directly from the simple classical picture outlined previously [117]. Note that the $\overline{V}$ entering the definition of ε is a root mean square

average of the modulation potential amplitude. If, for example, a sinusoidal modulation $V_{\mathrm{mod}}(y) = V_0 \cos(2\pi y/a)$ is considered, one has $V_0 = \sqrt{2}\overline{V}$.

The guiding center drift oscillations have also been explained on purely quantum mechanical grounds [118, 119]. If the weak periodic modulation $V(x)$ is treated by simple first-order perturbation theory, it is easily shown that this leads to a widening of the Landau levels to Landau bands according to $E_N(k_y) = (N+1/2)\hbar\omega_c + \langle Nk_y|V(x)|Nk_y\rangle$. The kets in the matrix element denote the Nth Landau state with center coordinate $x_0 = \hbar k_y/eB$ of the unperturbed system. If the matrix element is replaced by the classical expectation value, which can be done because high numbers of Landau levels are occupied at low fields, an expression very similar to Eq. (68) can be derived for $\rho_\perp$.

The result of the semiclassical calculation is shown in Figure 30 (thin solid line). A parameter value $\varepsilon = 0.015$ is assumed to reproduce best the corresponding experimental trace. The most interesting feature of Eq. (68) is the phase shift of $\pi/4$ appearing in the argument of the cosine term. The value of this phase shifts depends on the shape of the modulating potential and equals $\pi/4$ only if a simple sinusoidal potential is assumed. The perfect agreement with the phase shift of the experimental trace indicates that this assumption describes the actual shape of the potential very well.

Another important source of information on the potential parameters is the positive magnetoresistance at very low magnetic fields (denoted by the arrow labeled B_{crit} in Fig. 30). This property of $\rho_\perp$ is clearly not accounted for by the strongly simplified classical picture of undistorted cyclotron orbits undergoing a resonant drift. Beton et al. [121] investigated this positive magnetoresistance systematically by using a grating gate geometry similar to that used by Brinkop et al. [79] (cf. Fig. 12), which allowed them to vary the height of the modulating potential. We reproduce their results in Figure 32, where several magnetoresistance traces are shown for different voltages applied to the modulating gate.

As shown in the figure, with increasing gate voltage and thus increasing potential amplitude, the positive magnetoresistance is significantly enhanced and extends over a larger field range. Simultaneously, the number and peak-to-valley ratio of the commensurability oscillations are reduced. This behavior is easily explained by a modification of the simple

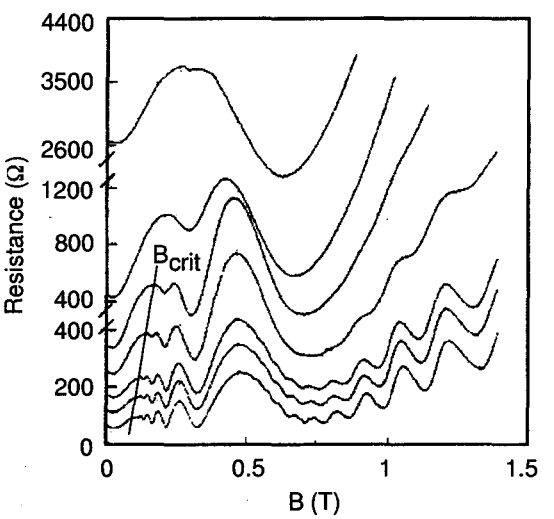

Fig. 32. Magnetoresistance traces measured at 2 K for different top-gate voltages. From top to bottom, $V_G = -1.0, -0.8, -0.6, -0.5, -0.3, -0.2$, and 0 V. The curves are displaced for clarity. The period of the modulation potential was $a = 300$ nm. B_{crit} is the critical field for magnetic breakdown (see also Fig. 30). For $B \geqslant 0.5$ T the usual Shubnikov–de Haas oscillations are observed. (Source: Reprinted with permission from [121]. © 1990 American Physical Society.)

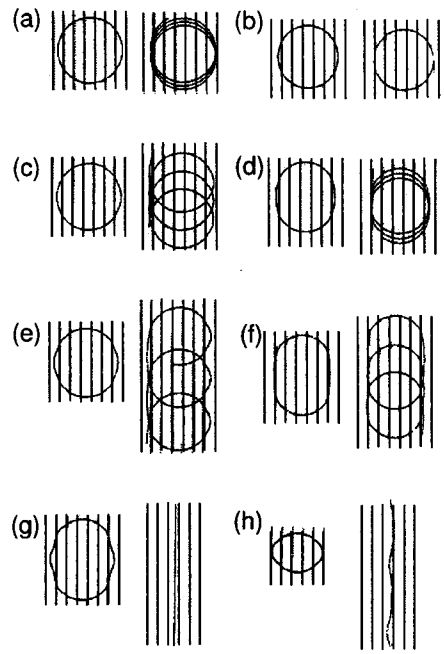

Fig. 33. Numerically calculated classical electron orbits in a periodic potential with a magnetic field applied perpendicular to the 2DEG. The straight lines symbolize the equipotential lines of the periodic potential. The orbits (a), (c), (e), and (g) correspond to $2R_c/a = 6.25$; the orbits (b), (d), (f), and (h) correspond to $2R_c/a = 5.75$. The left-hand orbit of each partial figure is symmetric with respect to the periodic potential; the right-hand one is positioned asymmetrically with respect to the equipotential lines. The values of the parameter $\varepsilon = eV_0/E_F$ are (a), (b) 0.01; (c), (d) 0.05; (e), (f) 0.09; and (g), (h) 0.15. (Source: Adapted from [121].)

classical picture outlined previously. The main ideas become clear from Figure 33, which shows numerically calculated classical trajectories for different potential heights (characterized by the parameter ε defined previously). The left-hand set of orbits is calculated for $2R_c/a = 6.25$, which, in the case of a weak modulation, would correspond to a maximum of $\rho_\perp$; the right-hand orbits were obtained for $2R_c/a = 5.75$, corresponding to a resistance minimum.

If the potential amplitude is increased, the corresponding electric field consequently enhances the $\mathbf{E} \times \mathbf{B}$ drift. On the other hand, this also leads to an increasing distortion of the cyclotron orbits. As a consequence those trajectories begin to drift (right-hand trajectories of parts b, d, f, and h of Figure 33), which are stationary in the weak potential case and lead to a distinct minimum in $\rho_\perp$. This fact explains the reduction of contrast of the commensurability oscillations with increasing potential amplitude. As shown in parts g and h of Figure 33, there is also a possibility of open orbits traversing parallel to the equipotential lines. Beton et al. [121] conclude from their classical model that a certain fraction of open orbits is present even for the smallest magnetic field values. Because the open orbits are traversed with the Fermi velocity v_F rather than with the slower $\mathbf{E} \times \mathbf{B}$ drift velocity, they dominate the resistivity at very low magnetic fields and lead to the observed positive magnetoresistance. As shown in Figure 32, the magnetoresistance (caused by open orbits) remains positive up to a certain magnetic field B_{crit} where it has a maximum, followed by commensurability oscillations resulting from closed and drifting orbits. It was shown by Beton et al. [121] that the maximum in $\rho_\perp$ occurs when the Lorentz force equals the electric force caused by the potential gradient:

$$2\pi \frac{V_0}{a} = eB_{crit} v_F \tag{69}$$

Magnetic fields weaker than B_{crit} are unable to force an electron on a closed cyclotron orbit against the action of the potential wells, which leads to a dominant fraction of open orbits. When the magnetic field exceeds the critical value determined by Eq. (69), the number of open orbits is drastically reduced ("magnetic breakdown"). It can be easily shown [121] that the magnetoresistance can be approximated by

$$\frac{\Delta\rho_{xx}}{\rho_0} \approx 2\omega_c^2\tau\frac{N_0}{N_T} \tag{70}$$

where N_0/N_T denotes the fraction of open orbits relative to the total number of trajectories and ρ_0 is the resistivity at zero magnetic field. In Eq. (70), the magnetic field dependence contained in ω_c together with the drastic reduction of N_0/N_T at

$$B \geqslant B_{crit} = \frac{2\pi V_0}{ea v_F} \tag{71}$$

leads to the observed peak in $\rho_\perp$ at low magnetic fields.

Beton et al. also gave a semiqualitative quantum mechanical explanation of the observed low-field behavior [122]. A rigorous analysis of the semiclassical dynamics in lateral superlattices was given by Streda and Kucera [123, 124], who analyzed the detailed features of the electronic energy spectrum and obtained the characteristic low-field magnetic breakdown peak from the Chambers solution of the semiclassical Boltzmann equation. A similar magnetic breakdown concept had been used earlier by Streda and MacDonald [125] for an investigation of the weak modulation limit. In principle, the classical considerations made responsible for the magnetoresistance peak remain a valid picture also in the more detailed study of Streda and Kucera. In contrast to the classical model of Beton et al. [121], however, the latter does not predict a magnetoresistance that falls off abruptly for fields $B \geqslant B_{crit}$, but behaves smoothly in this field regime. Also the relation for the expected peak position is slightly modified to $B_{crit} = 4V_0/ea v_F$.

According to Eq. (69), the determination of B_{crit} allows the characterization of the amplitude V_0 of the periodic potential, if the Fermi velocity v_F is known. An example of the application of Eqs. (68) and (69) to the systematic study of V_0 and its dependence on various sample parameters is given in Figure 34 [126]. The shown data were obtained from the magnetoresistance of an inverted, back-gated heterostructure. The lateral superlattice is induced by a grating metal gate, fabricated on top of the heterostructure. The gate fingers had a width of only 25 nm and formed a grating with period $a = 200$ nm. The height of the potential modulation was tuned by a voltage V_G applied to the top Schottky gates, whereas the electron density could be independently varied by a back-gate voltage. The different symbols in Figure 34 indicate different methods used to extract the value of V_0. The squares are obtained from an analysis of the magnetic breakdown peak discussed previously. The circles and triangles stem from a comparison of the $n = 1$ and $n = 2$ commensurability oscillations (labeled $i = 1, 2$ in the figure) to the theoretical expression Eq. (68), where this was possible. As shown in Figure 30, this approximate relation not only reproduces the correct period and phase of these oscillations, but also gives a fair approximation of their amplitude for low values of n. For higher n, the calculated amplitude generally overestimates the measured one, which is due to the previously discussed reduction of the oscillation "contrast" by distorted orbits not accounted for by the simple classical picture of [117].

Figure 34a shows the dependence of the potential amplitude on the gate voltage for a certain fixed back-gate voltage, that is, for fixed electron density. The two different evaluation methods approximately give the same results when the modulation is very weak. This is the regime for which Eq. (68) is conceived and where it gives a fair representation of the actual situation. For higher V_G, Eq. (68) yields smaller values than Eq. (71). It is expected that in the case of stronger modulation Eq. (68) overestimates the oscillation amplitude, particularly at higher indices n and, consequently, underestimates V_0. In part b of the figure, the same analysis is performed for fixed V_G but at different electron densities, varied by a back-gate voltage. Again, the two evaluation methods give different results for the

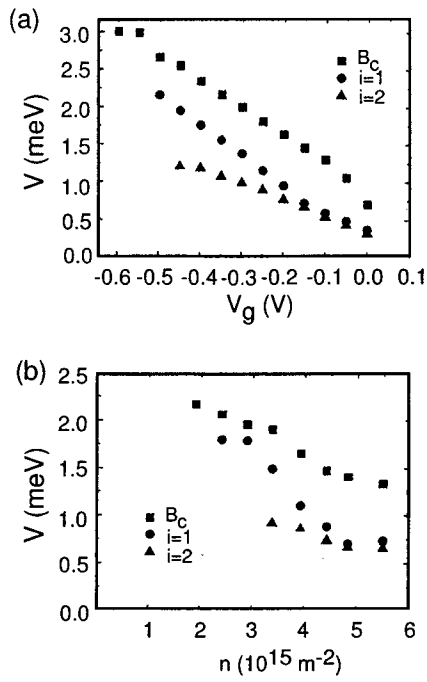

Fig. 34. Amplitude V of the periodic potential modulation for a back-gated inverted heterostructure, plotted as a function of the voltage applied to a grating gate, fabricated on top of the sample. Squares are obtained from an analysis of the magnetic breakdown peak at B_{crit}; circles and triangles are obtained from the application of Eq. (68) to the $i = 1$ and $i = 2$ commensurability oscillation. (Source: Adapted from [126].)

same reasons as before. However, all values confirm the observed trend of an increasing modulation amplitude (at fixed top gate voltage) with decreasing carrier density n_s. This carrier density dependence is a signature of screening effects that should be independent of n_s in a purely 2D electron system. The results of Figure 34b, therefore, nicely illustrate the reduction of screening when the potential amplitude increases and an increasing number of electrons become bound in one dimension.

A similar analysis has been applied to the characterization of short-period ($a = 100$ nm) lateral surface superlattices, fabricated by a plasma etching process [127]. An additional blanket gate on top of the etched superlattice has been used to improve the properties of the potential modulation. Indeed, the analysis of the phase of the commensurability oscillations shows that the blanket gate smooths the periodic potential and suppresses most of its higher harmonics; that is, the potential is sinusoidal to a very good approximation and, consequently, yields a phase shift of the commensurability oscillations equal to $\pi/4$. According to Davies and Larkin [128], a potential that is not perfectly sinusoidal creates higher harmonics in the magnetoresistance commensurability oscillations. Thus, an additional possibility to obtain information on the shape of $V_{\text{mod}}(y)$ is to analyze the Fourier transform of the low-field oscillatory magnetoresistance, taken as a function of $1/B$. This method was also applied in [127] and was found to confirm the results obtained from the phase analysis.

When the lateral superlattice potential becomes still stronger, the magnetoresistance anomalies change their character. This is illustrated in Figure 35 [129]. In this example, the periodic potential is created by shallow etching on a GaAs–AlGaAs heterostructure. The potential amplitude relative to the Fermi level is tuned by brief illumination from a red LED. In part a of the figure, V_0 and E_F, measured relative to the subband bottom in the wells of the lateral potential, are nearly equal. In this case, there is no trace of

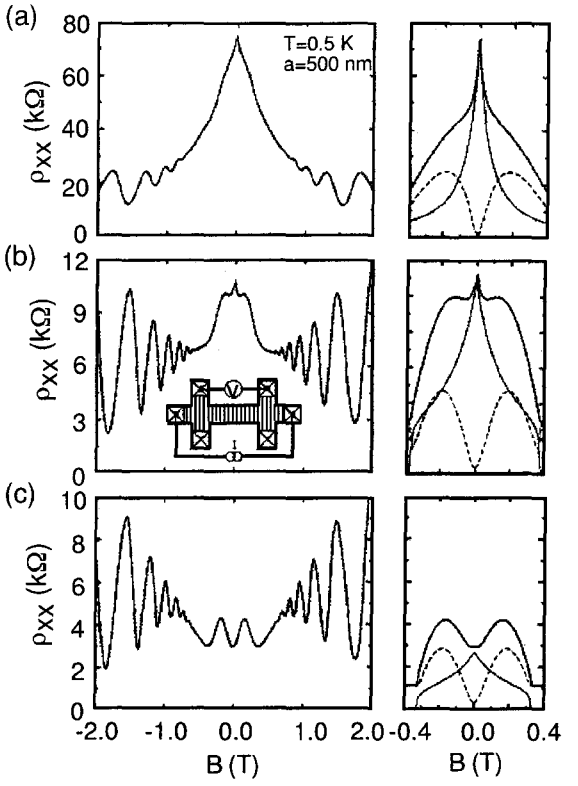

Fig. 35. The left-hand curves show experimental magnetoresistance traces for different amplitudes of the modulating potential. The top curve corresponds to the strongest modulation, the bottom curve to the weakest one. The inset in part b shows the experimental setup. The right-hand figures display the calculated magnetoresistance (thick solid lines; see text). The dashed curves correspond to the isotropic contribution to ρ_{xx}, thin solid lines to the anisotropic part, which dominates for very strong modulation. The Fermi level (measured from the bottom of the potential wells) and the potential amplitudes used in the calculation are: (a) $E_F^{weil} = 8.1$ meV, $V_0 = 7.8$ meV; (b) 8.6 meV, 7.0 meV; (c) 9.0 meV, 6.7 meV. (Source: Adapted from [129].)

a positive magnetoresistance, which, on the contrary, becomes negative. With increasing difference between V_0 and E_F, that is, decreasing ε, a positive contribution to the low-field magnetoresistance becomes visible, which dominates for the lowest value of ε (part c of the figure).

This behavior can be explained semiclassically if one assumes different scattering times for electrons bound in the wells and for those having sufficient energy to overcome the barriers and to move freely [129]. In the following outline of the underlying semiclassical model, we suppose that the potential modulation is in the x direction. One assigns a scattering time τ_0^b to those electrons bound in the well and τ_0^f to those electrons whose energy is high enough to overcome the barriers, both defined for zero magnetic field. With an applied magnetic field, the number of free electrons is not constant, because due to the Lorentz force electrons can acquire an additional momentum component in the x direction, which transforms previously bound electrons into free ones. Thus, for $B \neq 0$, one can define an average, magnetic field–dependent scattering time for free electrons

$$\frac{1}{\tau_f} = \frac{\theta_0}{\theta_B}\frac{1}{\tau_0^f} + \frac{\theta_B - \theta_0}{\theta_B}\frac{1}{\tau_0^b} \tag{72}$$

which is equivalent to the assumption that the phase space average of the scattering probability is not changed by a weak magnetic field. The angles θ_0 and θ_B delimit those regions in k space (at zero and nonzero magnetic field, respectively) that correspond to a free-electron

dispersion, that is, where the electrons have sufficient kinetic energy in the x direction to overcome the barriers. One finds from a semiclassical treatment [129] that the resistivity in the x direction may be split up into two components:

$$\rho_{xx} = \rho_{xx}^{\mathrm{iso}}(\tau_y) + \Delta\rho_{xx} \tag{73}$$

The first term follows from the Chambers solution of the Boltzmann equation

$$\rho_{xx}^{\mathrm{iso}}(\tau) = \frac{m^*}{e^2 n_s \tau} \frac{1 + \omega_c^2 \tau^2 C(\theta_B)}{1 - C(\theta_B)} \tag{74}$$

if for τ an *isotropic* scattering time is used, which is given by

$$\tau_y = \tau^f + \frac{\pi + \theta_B + \sin\theta_B}{\pi}\left(\tau_0^b - \tau^f\right) \tag{75}$$

The effect of anisotropy, induced by the presence of two different scattering times, is subsumed in the second term of Eq. (73):

$$\Delta\rho_{xx} = \frac{m^*}{e^2 n_s \tau_y} \frac{\pi - \theta_B + \sin\theta_B}{\theta_B + \sin\theta_B} \frac{\tau_0^b - \tau^f}{\tau^f} \tag{76}$$

In Figure 35, the magnetoresistance traces calculated according to Eqs. (74) and (76) are shown on the right-hand side. The dashed lines correspond to ρ_{xx}^{iso} which, in analogy to the strongly modulated case discussed previously, exhibits a positive magnetoresistance followed by a breakdown peak. The solid lines correspond to the anisotropic contribution $\Delta\rho_{xx}$. It can be seen that at large values of ε the anisotropic part strongly dominates the low-field magnetoresistance, leading to the characteristic spiked helmet form. The model calculations also allow one to estimate the amplitude of the periodic potential. However, the involved formalism is much more intricate than the methods described previously and does not lend itself to systematic routine investigations. The V_0 values corresponding to the different experimental situations shown in Figure 35 are given in the caption.

In conclusion, it is worth mentioning that the semiclassical modeling of magnetotransport in a periodic potential gives in a way complementary information on the underlying potential for weak and strong modulation. In the first case, the commensurability oscillations provide phase information that allows one to draw conclusions on the shape of the potential. However, because the semiclassical model treats the potential modulation as vanishingly small, the potential amplitude is not well reproduced by the semiclassical expressions (see [126]). In contrast to that, the magnetic breakdown picture yields a particularly simple tool for the determination of potential amplitudes but it is basically insensitive to the exact shape of the modulating potential. Sinusoidal or Kronig–Penney-like model potentials give essentially the same results [123, 129].

6. VERTICAL TUNNELING THROUGH QUANTUM WIRES

6.1. Experimental

In this section, we discuss the use of tunneling spectroscopy as a tool for the investigation of confining potentials and wave functions of 1D systems. Experimentally, tunneling via 1D states can be realized in various ways. Lateral tunneling between a quantum wire and 2D systems, for example, can be implemented on modulation-doped heterostructures using a split-gate geometry with a "leaky" channel. In this geometry, electrons are allowed to tunnel out of a 1DEG through a thin side-wall barrier into an adjacent 2D electron bath [130, 131]. A pronounced oscillatory structure can be observed in the 1D–2D tunneling current when the carrier concentration in the 1D channel is modulated through the split gates. These features reflect the modulation of the 1D density of states as the 1D subbands are successively depopulated with increasing split-gate bias.

However, tunneling between electron systems of different dimensionality in the vertical (growth) direction turned out to be the more interesting situation. In vertical geometry, epitaxial regrowth techniques either on V-groove etched substrates, as proposed by Luryi and Capasso [132], or on the edge of *in situ* cleaved substrates [133] can be used for devices, where electrons tunnel resonantly from a 2D emitter state into the 1D subbands of a quantum wire [134]. In such a sample, tunneling proceeds from the edge of a two-dimensional electron source through a bound state in a quantum wire into the edge of another 2D electron system and the combined effects of the longitudinal and perpendicular motion of electrons allows a detection of the excited wire states. On double-barrier resonant tunneling diodes, the lateral dimension can be restricted by use of focused Ga ion beam implantation [135]. In this case, the mixing of 2D emitter subbands and 1D subbands in the double-barrier region can be observed [136]. In theoretical models, these subband mixing and coupling effects turned out to be important and have, therefore, to be taken into account [137, 138].

The most instructive way to investigate tunneling processes through quantum wires, however, is to use a nanostructured double-layer electron system consisting of two coupled two-dimensional electron gas (2DEG) systems separated by a thin tunnel barrier. Three types of such bilayer structures have been extensively investigated: the double heterostructure with a two-dimensional electron gas on both sides of an AlGaAs barrier, the double-barrier resonant tunneling diode with two-dimensional emitter, and the coupled quantum well system. On all types of samples, either the upper 2D-channel, lying closer to the sample surface, or both channels can be patterned into quantum wires. In this way, tunneling processes from a 2D emitter into a system of one or more quantum wires and also vertical tunneling between insulated quantum wires can be investigated. In all these cases, the fundamental technological problem, which makes the construction of a vertical tunneling device a challenging task, is the formation of independent ohmic contacts to each of the barrier-separated low-dimensional systems. In the following, we discuss three representative experiments, each performed on one of the three mentioned systems of coupled electron channels. We describe briefly the sample geometry used and show some typical data obtained for each of these devices. In a subsequent section, we shall discuss briefly the theoretical models underlying the interpretation of these data. In the discussion, the emphasis will be put on the influence of the confining potential on the resonant tunneling characteristics or, vice versa, on the question to which extent the latter can provide substantial information on the former.

The double GaAs–AlGaAs–GaAs heterostructure, used in [23, 139–142], is shown in Figure 36a. The sample structure is made up of a nominally undoped GaAs layer

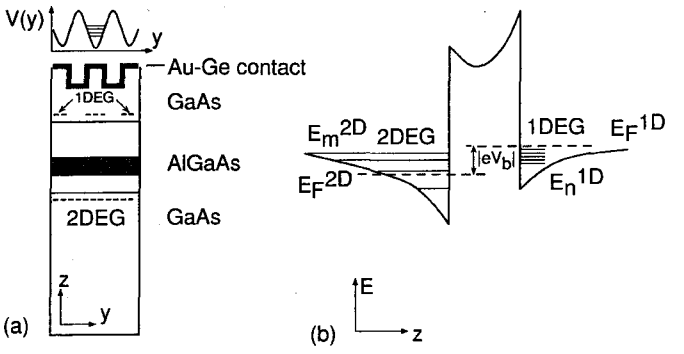

Fig. 36. (a) Schematic cross section of a processed single-barrier resonant tunneling device and resulting surface potential in the y direction (top). (b) Corresponding conduction band profile in the z direction. E_m and E_n denote the energy levels on the 2D and 1D side, respectively. E_F is the Fermi energy; V_b is the applied sample bias.

($N_A \leqslant 1 \times 10^{14}$ cm^{-3}) grown on a semiinsulating substrate, followed by an undoped AlGaAs spacer ($d = 50$ Å), doped $Al_xGa_{1-x}As$ ($d = 50$ Å, $N_D \leqslant 3 \times 10^{18}$ cm^{-3}, $x = 0.36$), another spacer ($d = 100$ Å), and n^--doped GaAs ($d = 800$ Å, $N_D \leqslant 1.2 \times 10^{15}$ cm^{-3}). An additional highly doped GaAs cap layer ($d = 150$ Å, $N_D = 6.4 \times 10^{18}$ cm^{-3}) was added on the surface. This structure provides an inversion layer at the lower GaAs/$Al_xGa_{1-x}As$ interface, containing several 2D subbands, and an accumulation layer at the upper $Al_xGa_{1-x}As$/GaAs interface, both separated by a barrier of only 200-Å thickness. From Shubnikov–de Haas measurements, it was deduced that in both 2DEG systems only one subband is occupied with values of $n_s^{inv} = 6.0 \times 10^{11}$ cm^{-2} and $n_s^{acc} = 5.5 \times 10^{11}$ cm^{-2} for the electron densities, respectively.

With this sample structure, 1D–2D tunneling can be realized if the upper channel is structured into quantum wires using, for example, standard laser holographic techniques and wet chemical etching. The etching process will induce a potential modulation only in the upper electron system, because the lower 2DEG is screened by the highly doped barrier separating the two channels. More details concerning sample preparation, particularly on the question of independent ohmic contacts to the low-dimensional systems, can be found in [140]. A bias voltage V_b, applied between the top and the bottom electron systems across the barrier, will shift the 1D states energetically with respect to the 2D electron gas as indicated in Figure 36b. It can be shown from self-consistent calculations that the externally applied voltage drops almost completely across the potential barrier. Consequently, the relative energy shift ΔE between the 1D and 2D system is equal to eV_b to a very good approximation, which considerably simplifies a quantitative analysis of the experimental data. Note that for this geometry both the initial and the final states involved in a tunneling process are quantized in a way that no free momentum component exists in the direction of the tunneling current.

Some typical tunneling data are shown in Figure 37. For reference purposes, consider first the results for the unstructured sample (upper curve in Fig. 37), where the resonant tunneling processes occur between two 2D electron gases and lead to a series of sharp peaks in dI/dV_b. Because in the geometry discussed the transverse electron momentum (parallel to the barriers) is conserved during the tunneling process, resonant tunneling occurs whenever the subband in the accumulation layer is energetically aligned with a subband in the inversion layer [141, 142].

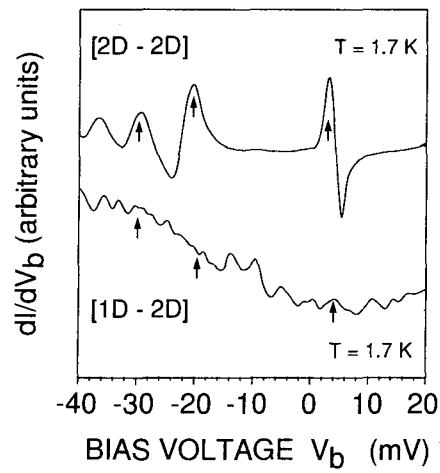

Fig. 37. dI/dV_b curves of an unstructured sample (2D–2D tunneling), recorded at $T = 1.7$ K and dI/dV_b characteristics of a nanostructured sample (1D–2D tunneling). The upward arrows indicate the resonance positions of the unstructured sample.

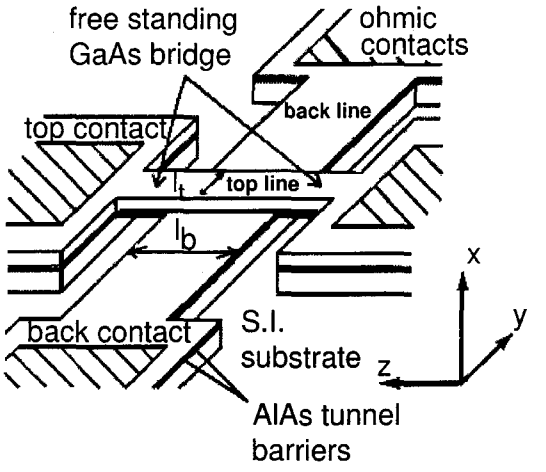

Fig. 38. Schematic diagram of a 1D–1D tunneling device based on a double-barrier resonant tunneling structure. (Source: Reprinted with permission from [143]. © 1994 American Physical Society.)

The trace at the bottom of Figure 37 shows the corresponding low-temperature dI/dV_b characteristics for a nanostructured sample. A wealth of additional structure appears in the differential tunneling characteristics in the investigated bias regime. It turns out that the identification of single peaks is not as straightforward as in the case of 2D–2D tunneling. It will be shown later in detail that for 1D–2D tunneling individual peaks in dI/dV_b cannot be simply assigned to the energetic alignment of the 2D emitter level with a special 1D wire state.

Vertical tunneling between single quantum wires (1D–1D tunneling) was demonstrated by Wang et al. [143, 157] in a very appealing way. They used a conventional double-barrier resonant tunneling diode with symmetric barriers having a thickness of 47 Å and enclosing a 90-Å-wide well. On both sides of the double barrier, 200-Å-thick spacer layers were grown to minimize the unintentional incorporation of donors into the well. The sample geometry depicted in Figure 38 is achieved by optical lithography and a series of selective wet chemical etch steps [157]. The top line has a submicrometer width and forms an air bridge to the top contact regions. This allows one to establish independent ohmic contacts to the top and back lines of the device. Its active area is formed by the overlap region of the top and back lines, as shown in Figure 39a. When a bias voltage is applied, the spacer in front of the double barrier forms an accumulation layer, which acts as a 1D emitter (see the conduction band profile in Fig. 39b). The 1D quantization energy $\hbar\omega_e$ in the emitter is determined by the width l_t of the top line and the side-wall depletion induced by the etching process. In general, the 1D quantization of the emitter will be much weaker than in the double-barrier region.

If the width l_t of the top line is in the micrometer range, a conventional small-area resonant tunneling diode is obtained, whose current–voltage characteristics display the usual region of negative differential resistance. The reduction of l_t to submicrometer dimensions leads to the observation of a rich additional structure in the I–V curves, which is due to resonant tunneling through the quantized 1D states between the AlAs barriers of the active area (cf. Fig. 48). Using magnetotunneling experiments, even the probability density of the quantum confined states can be determined with this device [144–146].

As a third example, we mention a vertical tunneling device that is based on coupled quantum wells [147–149]. Both wells are 180 Å wide and separated by a 125-Å AlGaAs barrier. The reported electron concentrations are typically 3×10^{11} cm^{-2} (μ = 800,000 cm^2/V s) and 1.8×10^{11} cm^{-2} (μ = 200,000 cm^2/V s) in the upper and the lower wells, respectively. On these samples, independent contacts to the electron systems in the

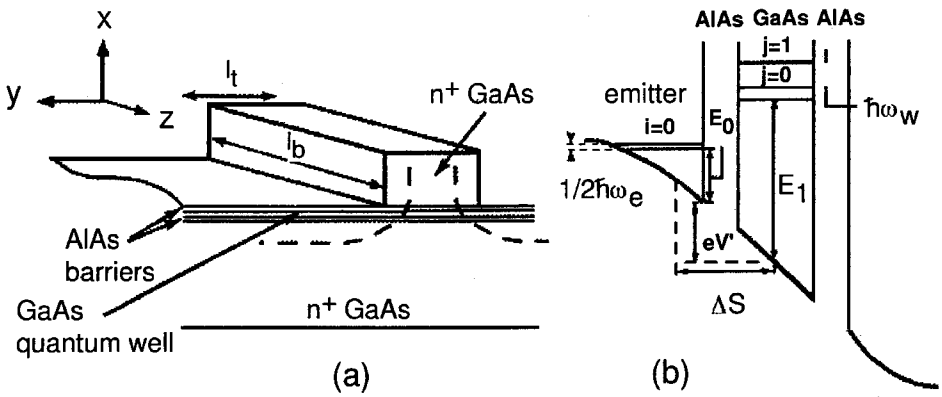

Fig. 39. (a) Side view of the 1D–1D tunneling device. The wires are formed by side-wall depletion underneath the GaAs bar. (b) Corresponding conduction band profile. $\hbar\omega_e$ and $\hbar\omega_w$ are the subband spacings in the 1D emitter and well. E_0 and E_1 are the energy levels resulting from quantization in the growth direction. (Source: Reprinted with permission from [144]. © 1995 American Physical Society.)

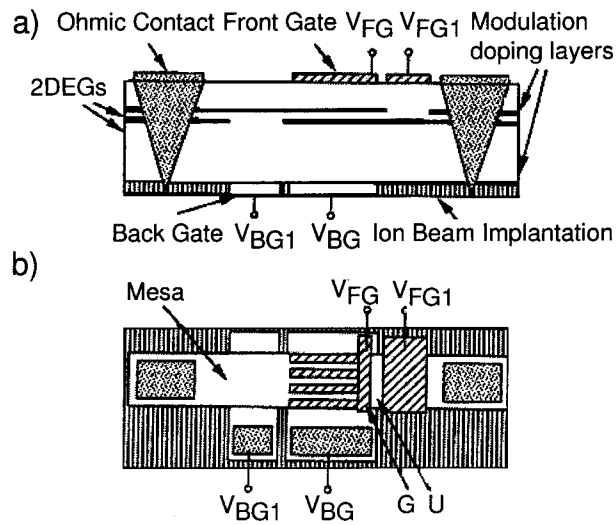

Fig. 40. Cross-sectional view (a) and top view (b) of the device structure. The selective depletion technique, which is used to contact each 2DEG separately, is shown in (a) and definitions of the different tunneling regions in (b). G denotes the gated, U the ungated region of the device leading to the q- and k-peaks shown in Figure 41. (Source: Reprinted with permission from [147]. © 1996 American Institute of Physics.)

upper and lower wells were established by *in situ* focused ion beam lithography and selective gate depletion techniques. A schematic view of the sample geometry is shown in Figure 40. The gates BG1, formed by an *in situ* patterned n^+ layer, and FG1 are used for the local depletion of the lower and upper channels, respectively. In this way, independent contacts to both 2D systems can be achieved. The back gate BG is used to tune the electron concentration in the lower channel. A potential modulation can be imposed on the upper well by means of the nanostructured top (front) Schottky gate FG.

The back gate allows the variation of the electron density (i.e., the Fermi level) in the lower channel. By recording the tunneling conductance as a function of the back-gate voltage, the resonant tunneling between the barrier-separated electron systems can be studied

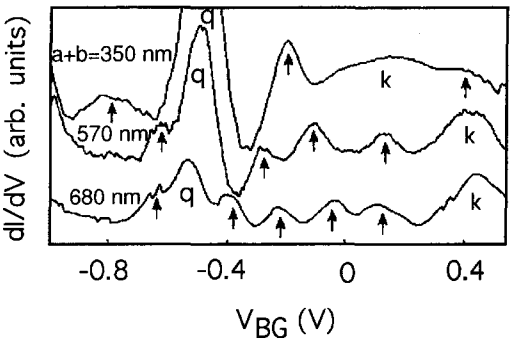

Fig. 41. Tunneling differential conductance for $V_{sl} = -0.25$ V and three different grating periods. The arrows mark the peaks, which are due to the crystal part of the 1DSSL band structure. Definition of separated quantum wires occurs at $V_{sl} = -0.45$ V. (Source: Reprinted with permission from [148]. © 1996 American Physical Society.)

without applying a bias voltage across the tunnel junction. This technique, first introduced by Eisenstein et al. [150–152], is called "equilibrium tunneling spectroscopy." In the case of 2D–2D tunneling, the net effect of the back-gate voltage is, just as in the previously discussed "biased" cases, a relative shift of the emitter and collector subband energies. As soon as the bottoms of the two subbands on both sides of the barrier are energetically aligned, the requirements of energy and momentum conservation are fulfilled and resonant tunneling between the subbands can occur. To study 1D–2D tunneling processes, a voltage V_{sl} can be applied to the front Schottky gate. This induces a potential modulation in the upper 2DEG whose amplitude can be tuned from zero up to a value where an array of independent quantum wires is established in the upper channel. At intermediate values of V_{sl}, the strength of the modulation is not sufficient to create a set of independent wires but rather leads to the formation of a lateral superlattice. For this latter situation, typical tunneling spectra are shown in Figure 41, where the differential tunneling conductance is plotted for three different grating periods and a front-gate voltage of $V_{sl} = -0.25$ V.

It can be shown (see the following sections) that the two large peaks, labeled k and q, are due to resonant 2D–2D tunneling between the 2D emitter and the 2D gases in the gated (q-labeled peak) and the ungated (k-labeled peak) regions of the device. They occur at back-gate voltages where the 2D electron densities in the emitter (lower) 2DEG and in the respective regions of the upper channel coincide. The small peaks, denoted by arrows, correspond to back-gate voltages where k_y at the Fermi energy in the 2DEG is equal to k_y in the one-dimensional surface superlattice (1DSSL) to within a reciprocal lattice vector $G_n = 2n\pi/(a+b)$ of the superlattice. Here, n is an integer, $a+b$ is the superlattice period (i.e., the sum of the width of a gate finger and the gate separation). The y axis is oriented perpendicular to the 1DSSL gates. In other words, the regular series of small-amplitude peaks can be assigned to the "crystal part" of the superlattice band structure.

Before continuing the discussion of these experiments, we briefly introduce the theoretical machinery of the transfer Hamiltonian formalism [153–155], which forms the basis of a quantitative analysis of all the vertical tunneling experiments discussed in this review.

6.2. Transfer Hamiltonian Formalism

Consider a tunneling process starting in an electron system, which we shall call the *emitter* in the following, and ending in some collector electron bath. To support the intuitive understanding of the following, one might imagine a 2DEG as the emitter and a second 2DEG, separated from the first through a barrier, as the collector system. In the formalism of the

transfer Hamiltonian approach, one treats, in a first step, both 2DEGs as independent systems. Each one is characterized by a complete set of eigenfunctions $\{\Psi_i\}_\mathrm{I}$ and $\{\Psi_k\}_\mathrm{F}$ and the corresponding eigenenergies, respectively (the indices I and F indicate the initial and final state of a tunneling process). If the two systems are brought into contact, for example, by a thin tunneling barrier, one may approximate the wave function of the total system by an expansion of the form

$$\Psi(t) = \sum_i a_i(t)\Psi_i \exp\left(\frac{iE_i t}{\hbar}\right) + \sum_k b_k(t)\Psi_k \exp\left(\frac{iE_k t}{\hbar}\right) \tag{77}$$

The indices i denote the emitter states and k those of the collector system. Equation (77) will be a good approximation if the coupling between the two systems is weak and the barriers are relatively thick. If the electron is assumed to start from a state $\{\Psi_0\}_\mathrm{I}$, one has as initial conditions for the coefficients $a_0(t=0)=1$ and $a_i(0)=b_k(0)=0$. The preceding total wave function may now be inserted into the time-dependent Schrödinger equation $i\hbar\dot{\Psi} = H\Psi$. If one assumes a weakly coupled system, a perturbation approach may be taken, which starts with the assumptions $a_i(t)\approx 1$, $b_k(t)\approx 0$, and $da_i(t)/dt \approx 0$ for all times t. This leads to the expression $\Psi(t)\approx\Psi_{i=0}\equiv\Psi_\mathrm{I}$ for the total wave function, and the time-dependent Schrödinger equation takes the form

$$\sum_k i\hbar\frac{db_k}{dt}\Psi_k \exp\left(-\frac{iE_k t}{\hbar}\right) = (H-E_\mathrm{I})\Psi_\mathrm{I}\exp\left(-\frac{iE_\mathrm{I}t}{\hbar}\right) \tag{78}$$

After multiplication with a state Ψ_F taken from the set of possible states in the collector system and repeating the same procedure familiar from standard time-dependent perturbation theory, one obtains for the transition probability between the states Ψ_I and Ψ_F the expression

$$\frac{|b_\mathrm{F}(t)|^2}{t} = \frac{2\pi}{\hbar}|M_\mathrm{IF}|^2\,\delta(E_\mathrm{F}-E_\mathrm{I}) \tag{79}$$

with a transition matrix element given by $M_\mathrm{IF} = \langle\Psi_\mathrm{F}|H-E_\mathrm{I}|\Psi_\mathrm{I}\rangle$. Note that in the present context E_F does not denote the Fermi level but the energy of the final state. To obtain the total transition probability, one has to sum over all initial and final states and to weight every term in the usual way by the combined probability to find the initial state occupied and the final state empty. This leads to the expression

$$P_\mathrm{IF} = \frac{2\pi}{\hbar}\sum_{m,n}\sum_{k_\mathrm{I},k_\mathrm{F}}|M_\mathrm{IF}|^2\big[f(E_\mathrm{I})-f(E_\mathrm{F})\big]\delta(E_\mathrm{I}-E_\mathrm{F}+eV_\mathrm{b}) \tag{80}$$

The δ function ensures the conservation of energy. Note that in the previous equation it is already assumed that a bias voltage is applied, which drops completely across the tunneling barrier and, hence, simply leads to a relative shift in the Fermi levels of the emitter and collector systems. Furthermore, the summation is carried out over all electron wave vectors k_x and k_y parallel to the barrier and all 2D subbands n, m of the initial and final 2DEGs. It can be easily shown that the matrix element M_IF can be transformed into the following expression [154]:

$$M_\mathrm{IF} = -\frac{\hbar^2}{2m^*}\int\!\!\int_{z=z_0} d^2S\left[\Psi_\mathrm{F}^*\frac{\partial\Psi_\mathrm{I}}{\partial z}\bigg|_{z=z_0} - \Psi_\mathrm{I}\frac{\partial\Psi_\mathrm{F}^*}{\partial z}\bigg|_{z=z_0}\right] \tag{81}$$

The integration over the surface elements dS has to be carried out in the plane of the barrier, which separates the initial and final side at $z=z_0$.

We first evaluate the matrix element M_IF for the case where both the initial and the final states are purely two-dimensional electron systems, as is the case for unstructured 2D–2D tunneling samples. In a two-dimensional system, the states are quantized in the z direction,

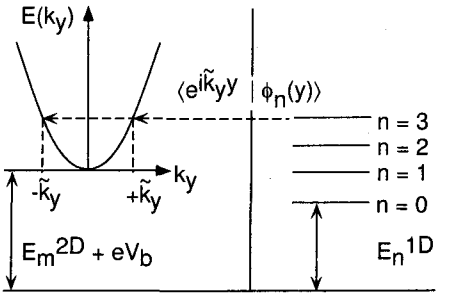

Fig. 42. Schematic illustration of a 1D–2D tunneling process. The arrow represents an electron tunneling from the quantum wire system into the 2DEG. The x component of the electron momentum is not considered here, as it is conserved during the tunneling process.

but free motion of electrons exists parallel to the barrier in the x and y directions. The wave functions for the initial and final states thus have the form

$$\begin{aligned} \Psi_{\mathrm{I}} &= \psi_{\mathrm{I}}(z)\exp(ik_{x,\mathrm{I}}x)\exp(ik_{y,\mathrm{I}}y) \\ \Psi_{\mathrm{F}} &= \psi_{\mathrm{F}}(z)\exp(ik_{x,\mathrm{F}}x)\exp(ik_{y,\mathrm{F}}y) \end{aligned} \tag{82}$$

Inserting these wave functions into the expression for the matrix element and evaluating the integrals yields

$$M_{\mathrm{IF}} = -\frac{\hbar^2}{2m^*}\left[\psi_{\mathrm{F}}^*\frac{\partial\psi_{\mathrm{I}}}{\partial z}\bigg|_{z=z_0} - \psi_{\mathrm{I}}\frac{\partial\psi_{\mathrm{F}}^*}{\partial z}\bigg|_{z=z_0}\right]\delta(k_{x,\mathrm{I}}-k_{x,\mathrm{F}})\,\delta(k_{y,\mathrm{I}}-k_{y,\mathrm{F}}) \tag{83}$$

The first term defines the *transmission coefficient of the barrier* in the z direction:

$$T_{\mathrm{IF}} = \left|\psi_{\mathrm{F}}^*\frac{\partial\psi_{\mathrm{I}}}{\partial z}\bigg|_{z=z_0} - \psi_{\mathrm{I}}\frac{\partial\psi_{\mathrm{F}}^*}{\partial z}\bigg|_{z=z_0}\right|^2 \tag{84}$$

The δ functions in Eq. (83) are the evaluated overlap integrals between the wave functions in the x and y directions of the initial and final states. Because for tunneling between 2D states these wave functions are plane waves, the overlap integrals reduce to δ functions. In this case, one thus obtains as a condition for resonant tunneling between 2D states that the electron wave vectors (k_x, k_y) parallel to the barrier have to be conserved during the tunneling process.

Next, we consider transitions between a 2D system and a quantum wire as the emitter. In this case, the wave functions are plane waves in the x and y directions in the 2D collector. For the quantum wire side, however, one has plane waves in the x direction but quantized states in the y direction. This situation is schematically sketched in Figure 42 for an electron tunneling from a 1D quantum wire state ($n = 3$) into an unoccupied 2D subband. For this situation, the wave functions are written as

$$\begin{aligned} \Psi_{\mathrm{I}} &= \psi_{\mathrm{I}}(z)\exp(ik_{x,\mathrm{I}}x)\exp(ik_{y,\mathrm{I}}y) \\ \Psi_{\mathrm{F}} &= \psi_{\mathrm{F}}(z)\exp(ik_{x,\mathrm{F}}x)\,\Phi_{n,\mathrm{F}}(y) \end{aligned} \tag{85}$$

and the corresponding matrix element for the 1D–2D tunneling process reads

$$\begin{aligned} M_{\mathrm{IF}} = &-\frac{\hbar^2}{2m^*}\left[\psi_{\mathrm{F}}^*\frac{\partial\psi_{\mathrm{I}}}{\partial z}\bigg|_{z=z_0} - \psi_{\mathrm{I}}\frac{\partial\psi_{\mathrm{F}}^*}{\partial z}\bigg|_{z=z_0}\right] \\ &\times\delta(k_{x,\mathrm{I}}-k_{x,\mathrm{F}})\int\exp(ik_{y,\mathrm{I}}y)\,\Phi_{n,\mathrm{F}}(y)\,dy \end{aligned} \tag{86}$$

We now assume that a voltage V_{b} is applied across the tunneling barrier and use Eq. (86) to calculate the total tunneling probability per unit time according to Eq. (80). The corresponding tunneling current is then given by $I = 2eP_{\mathrm{IF}}$, where the factor of 2 accounts

for the spin. The tunneling matrix element, Eq. (86), has two remarkable features. First, the δ function indicates that the x component of the electronic momentum is still conserved in a tunneling process. The second feature is the appearance of the overlap integral $\int \exp(ik_{y,\mathrm{I}}y)\,\Phi_{n,\mathrm{F}}(y)\,dy$ between the final and initial states in the y direction, which is recognized to be simply the Fourier transform of the quantized wire state forming the starting point of the tunneling process. This means that there are two main contributions to P_{IF}, leading to observable structure in the measured tunnel current: the transmission coefficient of the tunneling barrier [see Eq. (84)] and the overlap integral. For a single-barrier tunneling device, the transmission coefficient T_{IF} of the barrier adds no resonance structures to the tunneling current. Consequently, it will only be the overlap integral between the initial and final states that is responsible for all structures in the tunneling current. If we assume that the electron systems on both sides of the barrier are shifted in energy by eV_{b} with respect to each other, total energy conservation requires that

$$E_{n,\mathrm{I}} + \frac{\hbar^2 k_{x,\mathrm{I}}^2}{2m^*} + \frac{\hbar^2 k_{y,\mathrm{I}}^2}{2m^*} + eV = E_{\mu,\mathrm{F}} + \frac{\hbar^2 k_{x,\mathrm{F}}^2}{2m^*} \tag{87}$$

where μ is the subband index. Because we can ignore the free-electron motion in the x direction, this equation can be expressed in terms of k_y:

$$k_y(V) = \pm\sqrt{\frac{2m^*}{\hbar^2}[E_{\mu,\mathrm{F}} - E_{n,\mathrm{I}} - eV]} \tag{88}$$

This means that the wavevector of the tunneling electron, k_y, appearing in the overlap integral, is controlled by the external voltage. Consequently, the measured current–voltage characteristics of the tunneling device basically reflect the Fourier transform of the 1D emitter wave functions.

6.3. Influence of the Potential Profile on 2D–1D Tunneling Processes

The "real" profile of the confining potential in a quantum wire is determined by various effects such as Fermi-level pinning at exposed surfaces, free-carrier contributions, and many-body effects such as electron–electron interactions or screening at low temperatures. The bottom part of the quantum wire potential is especially influenced by the densities of free as well as fixed carriers, resulting in potential shapes ranging from almost parabolic to almost square well like.

To analyze the influence of the shape of the confining potential on the overlap integral in Eq. (86), one may calculate the wave function overlap for different model potentials. To do this, we consider as the emitter system an array of shallow etched quantum wires. If one assumes periodic boundary conditions, the following cosine-shaped potential can be considered as a reasonably good approximation of the real situation:

$$V(y) = V_{\mathrm{mod}}\left[\frac{1}{2} + \frac{1}{2}\cos\left(\frac{2\pi}{w}\left(y - \frac{w}{2}\right)\right)\right] \tag{89}$$

Here, V_{mod} is the potential amplitude and w is the electrical width of an individual quantum wire. Using Eq. (88), we now calculate the overlap integrals $I_n = |\langle \exp(ik_y y)|\phi_n(y)\rangle|^2$ as a function of the applied bias voltage. The results for the tunneling transitions from the four lowest 1D subbands ($n = 0, \ldots, 3$) into an unoccupied 2D subband are plotted in Figure 43. We first discuss the result for the lowest 1D subband ($n = 0$), which is shown in the uppermost curve.

At bias voltages where the 1D subband edge is energetically below the 2D subband edge ($V_{\mathrm{b}} > V_0$), resonant tunneling is forbidden because the total energy cannot be conserved in such a process. If the bias voltage reaches $V_{\mathrm{b}} = V_0$, the subband edges of the 2D subband

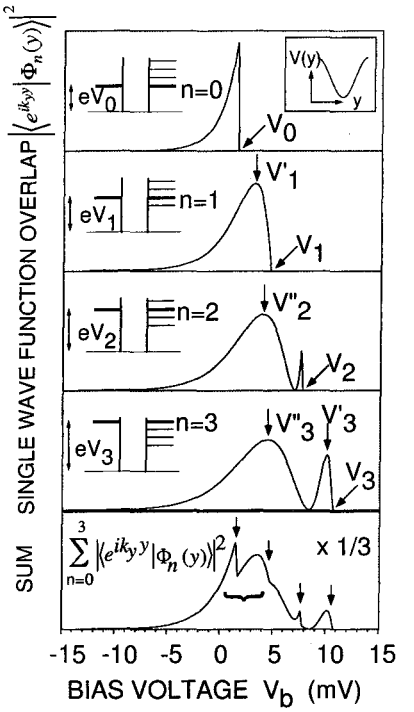

Fig. 43. Plot of the overlap integrals for the lowest four 1D subbands ($n = 0, \ldots, 3$) in a cosine-shaped potential [Eq. (89)], with a single 2D subband; V_n is the resonance position of the subband edges ($k_y = 0$), whereas ΔV_n denotes the deviation between the first overlap maximum and the position of the subband edge resonance V_n (only present for even n). The parameters for the 1D potential were $V_{\text{mod}} = 60$ mV, $w = 350$ nm. The lowest curve represents the sum of the upper four. (Source: Reprinted with permission from [23]. © 1993 American Physical Society.)

and of the lowest 1D subband ($n = 0$) are in resonance, and the overlap integral of the lowest 1D subband, I_0, reaches its maximum value. As V_b is decreased further, I_0 drops gradually toward zero. Note that I_0 indirectly reflects the spatial extent of the wave function, because it is nothing else than its Fourier transform. For the first excited 1D subband ($n = 1$), the tunneling probability, moreover, reflects the parity of this state. If the subband edges of both the 2D and the $n = 1$ subband coincide at $V_b = V_1$, I_1 is still zero because the corresponding 1D state has odd parity, $I_1(k_y = 0) = 0$. The tunneling probability then increases with decreasing bias voltage and reaches its maximum, which is slightly shifted by ΔV_1 from the subband edge resonance. With further decreasing bias voltage, I_1 drops toward zero. The behavior of the tunneling probabilities for the higher 1D subbands can, in principle, be understood in an analogous way.

It is obvious from Figure 43 that the maxima of I_n at the positions of the subband edge resonances (even 1D subband index, V_{2n}) or most close to them (odd 1D subband index, $V_{2n+1} + \Delta V_{2n+1}$) are much more pronounced than all the other structures caused by the nodes of the 1D wave functions. In addition, the values of ΔV_{2n+1} become smaller and smaller with increasing n (e.g., $\Delta V_1 > \Delta V_3$ etc.). Therefore, resonances caused by an energetic alignment between the subband edges of the 1D and 2D states can be expected to be dominant in the 1D–2D tunneling experiments, but are by no means the only reason for structures in the tunneling characteristics.

As has been shown previously, the confining potential in split-gate structures is rather "boxlike" than cosine shaped. Therefore, it is necessary to study also the influence of the steepness of the confinement walls. For this purpose, we choose an analytical expression

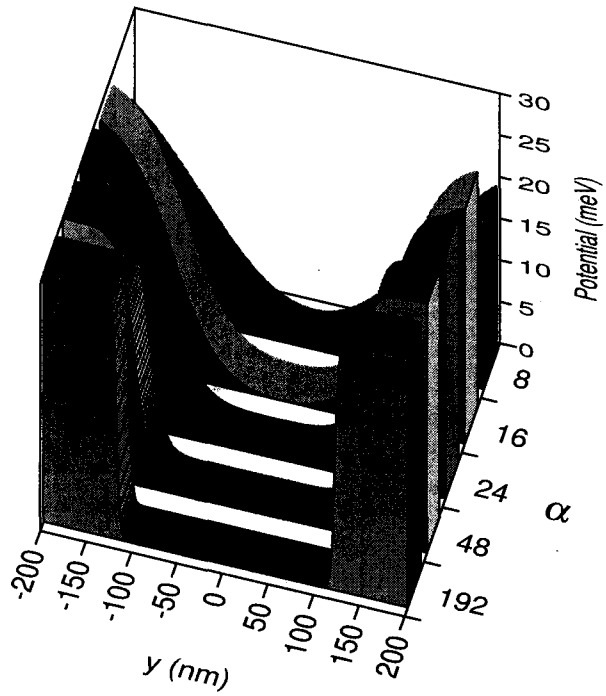

Fig. 44. Potential profiles for a series of α values, tuning the shape of $V(y)$ from smooth parabolic like ($\alpha = 8$) to almost rectangular box like ($\alpha = 192$).

for the potential, which allows us to control the steepness by a single parameter α. To obtain a potential profile that is smooth within one period of the multiple quantum wire system under consideration, we use the one-dimensional Woods–Saxon potential [42], which was already introduced in Section 2:

$$V(y) = V_{\text{mod}}\left[\frac{1}{1+\exp\left(\frac{\alpha(w/2-y)}{w}\right)} + \frac{1}{1+\exp\left(\frac{\alpha(w/2+y)}{w}\right)}\right] - V_{\text{min}} \tag{90}$$

The last term $V_{\text{min}} = V_{\text{mod}}\{2/[1+\exp(\alpha/2)]\}$ sets the potential minimum to zero. The parameter α allows a continuous variation of the potential shape from an approximately parabolic to a nearly rectangular form.

Figure 44 shows the potential profiles for a series of α values, starting at $\alpha = 8$ (nearly parabolic) and ending at $\alpha = 192$ (nearly rectangular box). The other parameters used in the calculation are $V_{\text{mod}} = 50$ meV and $w = 250$ nm.

In analogy to the case depicted in Figure 43, the overlap integral for the 1D ground state $n = 0$ and the third excited 1D subband $n = 3$ as well as their sum ($\sum n = 0, \ldots, 3$) is calculated for various values of α. The results are plotted in parts a–c of Figure 45.

Because of the variation of the potential profile, the energies of all 1D subband edges are shifted to lower values with increasing parameter α. The change in shape of the wave functions has a pronounced effect on the corresponding overlap integrals. This is illustrated for the 1D ground state in Figure 45a. With rising α, the spatial extent of the wave function is increased. As a result, the overlap integral of the single 1D wave function is squeezed on the wavevector scale k_y and, consequently, on the bias voltage scale V_b, too. In addition, the maximum tunneling probability is increased by more than 50%, whereas the integral tunneling probability, which is represented by the area enclosed by the curve, decreases simultaneously by a factor of 2. This behavior is even more pronounced for the overlap integrals of the higher quantum wire states, as shown in Figure 45b for the subband index $n = 3$. While α increases, the resonance structure close to the position of the subband

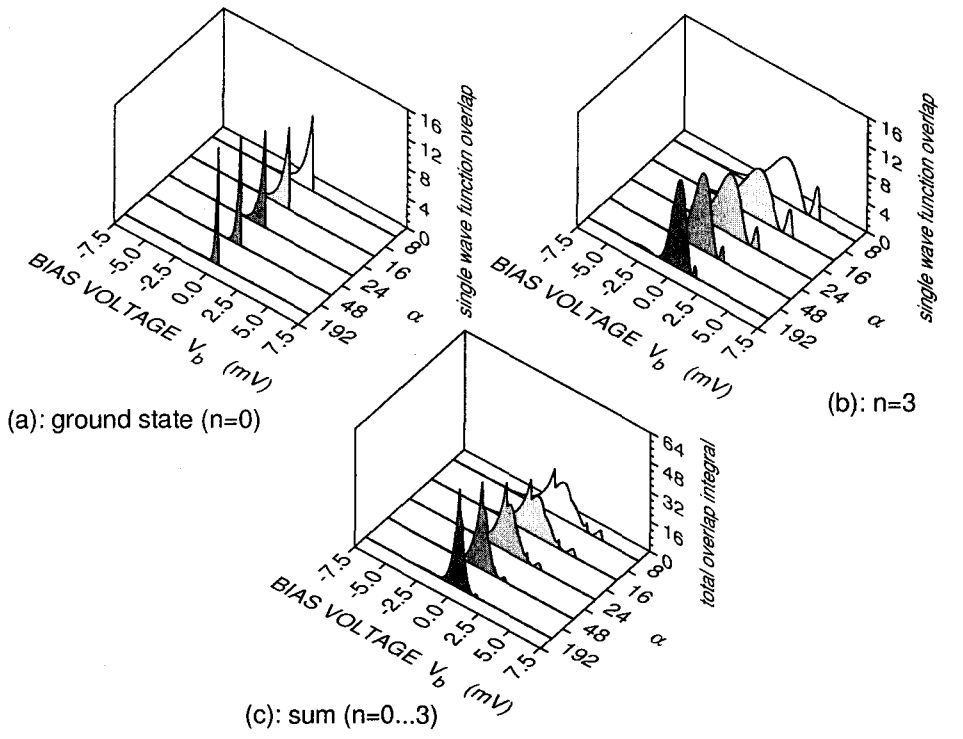

Fig. 45. Plot of the overlap integrals for the 1D subbands $n = 1$ (a) and $n = 3$ (b) with a single 2D subband as a function of the parameter α. (c) Sum of the overlap integrals of the lowest four subbands. (Source: Reprinted with permission from [23]. © 1993 American Physical Society.)

edge resonance (labeled V_3' in Fig. 43) is systematically degraded. In contrast to that, the tunneling probability at the bias voltage position of the second maximum (labeled V_3'' in Fig. 43) is drastically increased and becomes the by far most dominant structure for high values of α. Comparing the amplitudes of the overlap integral at the voltage positions V_3' and V_3'', their ratio increases from 1.4 for $\alpha = 8$ to above 8 for $\alpha = 192$. For the rectangular potential profile, the maximum in the tunneling probability at V_3'' coincides with the subband resonance position of the lowest 1D subband, that is, $V_b = V_0$.

To illustrate this remarkable behavior more clearly, we have recalculated the results shown in Figure 43 for a box potential with infinitely high walls and a width of $w =$ 100 nm. For this potential profile, the values of I_n ($n = 0, \ldots, 3$) as well as their sum are plotted in Figure 46. Although the shapes of the curves are qualitatively identical with the corresponding curves of Figure 43, the intensity ratios of the structures within a curve show a completely different behavior. As pointed out previously, only the structures in the vicinity of the resonance of the lowest 1D subband (labeled V_0, V_1', V_2'', and V_3'') remain important. The width of these resonance structures, however, increases as the 1D quantum number increases. All other peaks of I_n for the higher 1D subbands at voltage positions $V_b > V_0$ are of minor importance, because their intensity can be neglected. All these features are also present in the sum of all overlap integrals, which determines the total tunneling probability (lowest curve of Fig. 46). There is only one broad maximum dominant, peaking at a bias voltage of V_0. This result is valid for all quantum wire subbands, but particularly pronounced for higher subband indices.

The total tunneling probability exhibits less and less structures as the potential profile is tuned from a smooth parabolic shape to a rectangular shape, as shown in Figure 45c. In the latter case, just one broadened maximum, located at $V_b = V_0$, characterizes the tunneling probability for all 1D subbands. Therefore, a single, but broad resonance structure

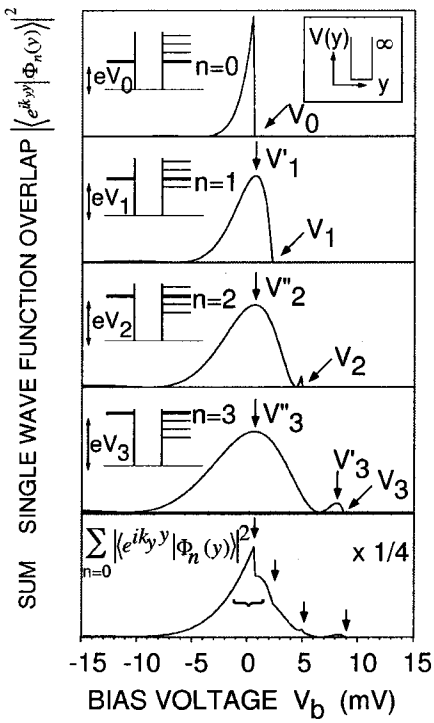

Fig. 46. Plot of the overlap integrals for the lowest four 1D subbands ($n = 0, \ldots, 3$) with a single 2D subband (not occupied) for a box potential with infinite high walls and a width of 100 nm. The lowest curve represents the sum of the overlap integrals for the four lowest subbands. (Source: Reprinted with permission from [23]. © 1993 American Physical Society.)

is expected at the position of the former 2D–2D resonance (which in the ideal case of zero-level broadening is a δ function), but only very weak additional structures resulting from the 1D subbands should occur at higher bias voltages. For a smooth potential profile, however, all quantum wire states give rise to a series of resonances that interfere within the voltage range mentioned previously.

With these insights into the nature of the 1D–2D tunneling process, an attempt can be made to simulate the corresponding tunneling characteristics and to compare them with the experimental results depicted in Figure 37. First, note that the experimental I–V curve displays a multitude of resonant structures. From the preceding analysis we know that a rectangular potential would lead only to a weak fine structure in the overlap integrals and, consequently, in the total tunneling probability P_{IF} [cf. Eqs. (80) and (86)]. One therefore concludes that the confinement leading to the characteristics of Figure 37 is due to a smooth potential profile. In the following, we shall only be interested in the numerical reproduction of the average number and spacing of the experimental tunneling structures. We, therefore, describe the 1D confinement by the cosine function of Eq. (89), which was found previously to be a good approximation of the potential of shallow etched wires [140]. The resonant tunneling current $I(V_{\mathrm{b}})$ is calculated according to $I = 2eP_{\mathrm{IF}}$ together with Eq. (88) and its first derivative $dI(V_{\mathrm{b}})/dV_{\mathrm{b}}$ is obtained numerically. To account for generic broadening effects caused by the limitation of the carrier lifetime in the states involved in the resonant tunneling process and by the interaction between electrons and acoustic phonons, the tunneling probability near a resonance at V_{b}' is assumed to have Lorentz form, which we denote by $L(V_{\mathrm{b}} - V_{\mathrm{b}}')$:

$$L(V_{\mathrm{b}} - V_{\mathrm{b}}') = \frac{1}{\pi} \frac{\Gamma}{(V_{\mathrm{b}} - V_{\mathrm{b}}')^2 + \Gamma^2} \tag{91}$$

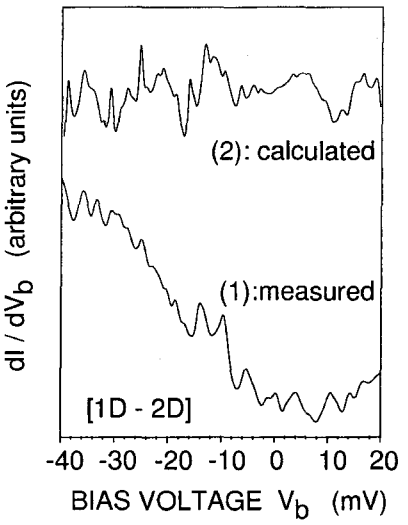

Fig. 47. Comparison of the measured and calculated 1D–2D tunneling characteristics (see also Fig. 37). (Source: Reprinted with permission from [23]. © 1993 American Physical Society.)

In this equation, Γ represents the linewidth of any resonance position on the scale of the applied voltage. The application of Eq. (91) to the model calculation also accounts for broadening effects caused by the sample preparation technique, such as fluctuations of the wire width and so on. The total tunneling current is then given by the convolution of the current represented by the bare tunneling probability and the Lorentz function given previously [154, 156]:

$$j_{\mathrm{tot}} \rightarrow \int dV_{\mathrm{b}}' j_{\mathrm{tot}}(V_{\mathrm{b}}') L(V_{\mathrm{b}} - V_{\mathrm{b}}') \tag{92}$$

The positions of the 2D subbands in the inversion (collector) layer needed for the calculation can be obtained from the tunneling experiments on non-nanostructured samples.

The final result is shown in Figure 47, curve 2, assuming a temperature of $T = 2$ K and a level width $\Gamma = 0.5$ mV. The parameters of the cosine potential were chosen to be $V_{\mathrm{mod}} = 55$ meV and $w = 350$ nm. The corresponding experimental result is plotted as curve 1 in the figure. All structures in the calculated dI/dV_{b} curves are mainly caused by the overlap integral. As a major difference between the measured and calculated curve, one may note that in the former the resonant tunneling structure is superposed on a background that increases monotonically with decreasing bias voltage. This background presumably reflects a possible energy (i.e., bias voltage) dependence of the transmission coefficient of the tunneling barrier [Eq. (84)]. Note that the structures of the calculated curve are determined by the sum of overlap integrals as discussed previously. Any influence of the applied bias voltage on the transmission coefficient of the barrier itself is neglected in the calculation. Nevertheless, the qualitative features of the measured tunneling characteristics, for example, the average peak amplitude and peak distance, are well reproduced within the outlined model. However, as one has to sum up over all closely spaced 1D emitter and 2D collector subbands, it is not possible to identify and analyze the contributions of each single 1D state to the total tunneling current. The main factor, which limits the resolution, is the doped barrier between the 1D and 2D systems. It introduces scattering in the tunneling process and, therefore, broadens the linewidth of the resonances in the dI/dV_{b} curves. Because of the large number of resonance structures in the dI/dV_{b} curves, the peaks will overlap and also smear out, which makes a more detailed quantitative analysis rather difficult.

6.3.1. 1D–1D Tunneling: Probing the Fourier Transform of One-Dimensional Wave Functions

In the experiment outlined previously, it was not possible to explain all measured features of the tunneling characteristics in detail, although its numerical analysis gave valuable insight into how the presence of numerous 1D subbands influences the 1D–2D tunneling current when the conservation of the k_y momentum component is relaxed because of the confinement in the y direction. The particular form of the tunneling matrix element in Eq. (86) also suggests the possibility of measuring directly the Fourier transform of the wave functions of the confined emitter states. To this end, however, the number of 1D subbands contributing to the tunneling characteristics within a given bias voltage interval has to be considerably reduced. Progress in this direction has been achieved by manufacturing single-wire tunneling devices from double-barrier resonant tunneling diode (DBRTD) structures [157]. The corresponding device geometry is shown in Figure 39 together with the definitions of some notation used later on. Depending on the width l_t of the top line, a situation can be achieved where only one 1D subband is occupied in the emitter and the subband spacing in the well, $\hbar\omega_w$, is on the order of 10 meV [144]. For this situation, a set of tunneling I–Vs is shown in Figure 48, obtained for different magnetic fields applied perpendicular to the tunneling direction (and parallel to the top line). Each of the displayed tunneling peaks now corresponds to transitions from the single 1D emitter level (labeled by $i = 0$) into a single collector level(labeled by the index j).

For the numerical analysis of the measured I–Vs, a modified form of the transfer Hamiltonian formalism is applied [145, 146]. In the form used by Beton et al. [144] and Wang et al. [143], level broadening is included in the formalism from the very beginning by replacing the δ functions used in Eq. (80) with spectral density functions [158, 159]. The corresponding expression for the tunneling current as a function of bias voltage V, applied across the barrier, is

$$I = 2e \sum_{k_y,k_z} \sum_{jk'_z} |T_{jk'_z,k_y,k_z}|^2 \int \frac{d\varepsilon}{2\pi} A_e(k_y, k_z, \varepsilon) \times A_w\left(jk'_z, \varepsilon + eV\right) f(\varepsilon) \qquad (93)$$

The coordinate system underlying this equation is shown in Figure 38. T denotes the tunneling matrix element already introduced in Eq. (86). The spectral density functions A_e and A_w for the emitter and the well have Lorentzian shape. In addition, it is assumed that there is no charge accumulation in the well and that all collector states are empty. If a

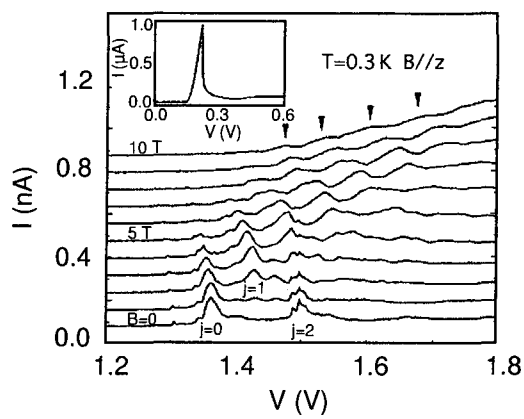

Fig. 48. I–V characteristics of a 1D–1D submicrometer tunneling diode in the presence of a magnetic field applied parallel to the z direction. The curves are measured for magnetic field strengths ranging from 0 T (lowest curve) up to 10 T (uppermost curve), varied in 1-T steps. The curves are offset for clarity. The inset shows I–V at $B = 0$ T for a large-area device. The device geometry is shown in Figure 38. (Source: Reprinted with permission from [144]. © 1995 American Physical Society.)

magnetic field is applied parallel to the top line (cf. Fig. 39), the tunneling current can be expressed as [145]:

$$\frac{I}{I_0} = \frac{1}{\pi} \sum_{ij} \left\{ \frac{2[\varepsilon_F - (i+1/2)\hbar\hat{\omega}_e]}{\hbar\omega_e} \right\}^{1/2} M_{ij}^2(B) \frac{\Gamma^2}{(\varepsilon_i + eV^* - \varepsilon_j)^2 + \Gamma^2} \tag{94}$$

Here, ω_e is the confining frequency of the emitter quantum wire whose confinement potential is assumed to be parabolic. $\hat{\omega}_e = \omega_e(\Omega/\sqrt{\Omega_e^2 + \omega_c^2})$ is the emitter frequency in the presence of a magnetic field.* I_0 is a renormalized tunneling current that is solely due to the transmission coefficient t of the barrier: $I_0 = 4et^2\sqrt{m\omega_e/\hbar}(L_z/\Gamma)$. The main information on the tunneling process is contained in the matrix element M_{ij}, which now reads

$$M_{ij}(B) = \int \frac{dk_y}{2\pi} \Phi_i\left(l_e^{-2}\hat{l}_e; k_y - \frac{eB\Delta s}{\hbar}\right) \Phi_j\left(l_w^{-2}\hat{l}_w; k_y\right) \tag{95}$$

Here, $\Phi_{i,j}$ are the Fourier transforms of the corresponding wave functions in the emitter (i) and the well (j) and the $l_{e,w}$ are given by $l_{e,w} = (\hbar/m\omega_{e,w})^{1/2}$ (in $\hat{l}_{e,w}$ the corresponding frequencies $\hat{\omega}_e$ have to be inserted). The magnetic field dependence enters through a parameter $k_0 = eB\Delta s/\hbar$ in the tunneling matrix element, where Δs is the spatial separation of the 1D states in the emitter and in the well. The k_0 dependence can be derived quantum mechanically, but it can also be motivated from a simple classical picture. In the given geometry of $B \| z$, an electron moves on a curved orbit. While it is traveling the distance Δs in the x direction, the electron momentum in the y direction changes by $eB\Delta s = \hbar k_0$ through the influence of the Lorentz force. In a quantum mechanical picture of 2D–2D tunneling, this means that the magnetic field introduces a wavevector shift of k_0 between the initial and final states, which is achieved by applying the translation operator ($\exp(-ik_0 y)$) to the corresponding wave function. For 1D–1D tunneling, however, k_0 enters as a wavevector shift between the Fourier transforms of the initial and final wave functions of the 1D states.

Now, if only one subband is occupied in the emitter and the subband spacing in the well is large enough, one has realized the unique situation that the Fourier transform of the probability density of the laterally confined states in the well can be determined directly, if the resonant tunneling current is measured as a function of the magnetic field applied parallel to the wires. Note that the occupation of only one emitter state is crucial for this purpose; otherwise, the measured $I(B)$ curve will be a convolution of many resonances of all occupied states. In the case of a single-emitter subband, resonant 1D–1D tunneling via the jth state in the well occurs when the voltage is adjusted in a way that the emitter state is aligned in energy with the jth state in the well, which is for (see also Fig. 39)

$$eV^* + E_0 + \frac{\hbar\hat{\omega}_e}{2} = E_1 + \left(j + \frac{1}{2}\right)\hbar\hat{\omega}_w \tag{96}$$

Here, E_0 is the emitter subband energy, E_1 the subband energy in the well (both are magnetic field dependent in the special notation used in [145]), V^* is the voltage drop across the barrier, and $\hat{\omega}_e$ and $\hat{\omega}_w$ the magnetic field–dependent oscillator frequencies of the lateral confining potentials in the emitter and the well, respectively. At resonance, the current flowing through the jth state, $I_j(B)$, is proportional to the modulus squared of the overlap integral $M_j(B)$ between the initial and final state. This is given by Eq. (95), which can be rewritten as [144]:

$$\begin{aligned} M_j(B) &= \int_{-\infty}^{+\infty} \exp(-ik_0 y)\, \varphi_0^e(y)\, \varphi_j^w(y)\, dy \\ &= \int_{-\infty}^{+\infty} \Phi_0^e(k_y - k_0)\, \Phi_j^w(k_y)\, dk_y \end{aligned} \tag{97}$$

* In the special notation used by Mori et al. [145], Ω_e quantifies the confinement in the growth direction, which is assumed to be parabolic for simplicity. In a magnetic field, this confining frequency also becomes magnetic field dependent.

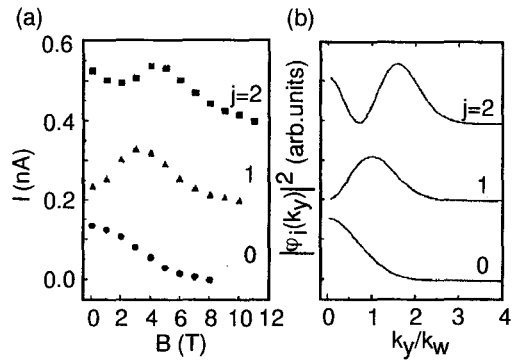

Fig. 49. (a) Peak currents as a function of magnetic field for the $j = 1, 2, 3$ resonance peak. The experimental data are displaced for clarity. (b) Probability densities for the $j = 0, 1, 2$ simple harmonic oscillator states plotted versus k_y/k_w. A value of $\hbar\omega_w = 10$ meV was assumed for this calculation. (Source: Reprinted with permission from [143]. © 1994 American Physical Society.)

where $\Phi_0^e(k_y) = \int_{-\infty}^{+\infty} \varphi_0^e(y) \exp(ik_y y)\, dy$ and $\Phi_j^w(k_y)$ are the Fourier transforms of the emitter and well wave functions. As discussed previously, the magnetic field thus induces a relative shift in k space between the emitter and the collector states. If the emitter state has a narrow spread in k space, Eq. (97) shows that the Fourier transform of the jth 1D wave function in the well can be probed by simply measuring the peak tunneling current as a function of the magnetic field. Due to the asymmetry of the 1D–1D tunneling device, the assumption of narrow k spread of the emitter wave function is justified because the confining potential in the y direction is much stronger between the double barriers than for the emitter electrode owing to side-wall depletion.

Figure 49a shows the peak currents of the magnetotunneling peaks labeled $j = 0, 1, 2$ in Figure 48, plotted as a function of the magnetic field. In Figure 49b the calculated Fourier transforms of the probability densities, corresponding to the three lowest states in a simple harmonic oscillator potential, are also shown for the purpose of comparison. For convenience, the calculated probability density was plotted versus k_y/k_w, where $k_w = (m\omega_w/\hbar)^{1/2}$ and k_y is calculated from $k_y = eB\Delta s/\hbar$. If one chooses $\hbar\omega_w$ such that the measured and the calculated positions of the $j = 1$ maximum coincide, one obtains excellent agreement between the measured and the calculated results. However, one has to be aware of the fact that the width of the emitter Fourier transform $\Phi_0^e(k_y) = 1/(\pi k_e^2)^{1/4} \exp(-k_y^2/k_e^2)$, characterized by $k_e \equiv (m\omega_e/\hbar)^{1/2}$ is finite. This limits the resolution of the minimum of the $j = 2$ state.

6.3.2. 2D–1D Surface Superlattice Tunneling: Measuring Potential Profiles

In the preceding experiment, vertical transport through quantum wires and the transfer Hamiltonian formalism were used to determine the probability density for electrons in quantum wire states. The measured (k space) probability density was found to agree well with the one expected for a parabolic confinement potential. This justifies the assumptions on the shape of the confinement made to get tractable expressions in the formalism used for the analysis of the experiments. As will be shown in this section, this type of wave function spectroscopy allows one to gain even more detailed information on the shape of confining potentials. A particularly well elaborated example of this is ? by the results of Kardynal et al. [147–149], who have used the tunneling geometry shown in Figure 40.

As already mentioned earlier, their device allows them to perform equilibrium tunneling spectroscopy, that is, the measurement of the differential tunneling conductance as

a function of the Fermi energy in the emitter without applying a bias voltage across the tunneling barrier. Due to the particular sample layout this can be done as a function of different parameters, such as magnetic fields or front-gate voltages. The latter offers the possibility of using, alternatively, a set of independent quantum wires [147] or a lateral surface superlattice (1DSSL) [148] as the collector system. For the quantitative analysis of their experimental results, Kardynal et al. also employ a transfer Hamiltonian formalism similar to the model discussed in the previous section. They obtain for the derivative of the tunneling current the following expression [148]:

$$\frac{dI}{dV} \propto t^2 \sum_{k_x,k_y} B_1(k_x, k_y, \mu) A_2(k_x, k_y, \mu) \tag{98}$$

where the so-called augmented spectral function

$$B_1(k_x, k_y, \mu) = \sum_{\nu} \left|\widetilde{\varphi}_{k_x,\nu}(-k_y)\right|^2 A_1(k_x, k_y, \nu, \mu) \tag{99}$$

has been introduced, whose detailed form will be discussed later for the case of tunneling into a lateral 1DSSL. A_1 and A_2 are Lorentzian spectral functions accounting for level broadening just as in Eq. (93). t^2 is again the transmission coefficient of the tunneling barrier. In fact, Eq. (98) is equivalent to Eq. (93), because the differentiation with respect to V removes the integration over the energy ε. Note, however, that in the preceding expression the general overlap integrals are already cast in a form appropriate for a 2D emitter and a set of tightly bound superlattice states in the collector. In the notation of Kardynal et al. [148], the spectral functions are written as

$$A_{(1,2)}(s_{1,2}, \mu) = \frac{\Gamma}{2\pi[(\Gamma/2)^2 + (\mu - \xi^{(1,2)}_{s_{(1,2)}})^2]} \tag{100}$$

where $s_1 = (k_x, k_y, \mu)$ and $s_2 = (k_x, k_y)$ are the relevant quantum numbers for the 2DEG and the 1DSSL, $\hbar/\Gamma$ is the quasiparticle lifetime, and μ is the electrochemical potential. $\xi^{(1)}_{s2} = (\hbar^2/2m)(k_x^2 + k_y^2) + V_2$ is the energy dispersion in the 2DEG. If tunneling into a 1DSSL is studied, the energy dispersion of the collector electron gas is written as $\xi^{(1)}_{s1} = \hbar^2 k_x^2/2m^* + E_{k_y,\nu} + V_1$, where the miniband structure of the 1DSSL is characterized by $E_{k_y,\nu}$ (termed the *crystal part* of the 1DSSL band structure in [148]), ν being the miniband index. $V_{(1,2)}$ are the energy levels of the 2D subbands in the upper and lower channels, respectively. Because of the superlattice nature of the collector system, the wave functions perpendicular to the 1DSSL are Bloch functions. If a tight binding picture is adopted, they are given by a linear combination of the $\varphi_{k_y,\nu}(y)$ obtained by solving the Schrödinger equation in the range $0 \leqslant y \leqslant a + b$ for a single potential well of the 1DSSL:

$$\Phi_{k_y,\nu}(y) = \sum_{n} \exp\big(ik_y n(a+b)\big)\varphi_{k_y,\nu}\big(y - n(a+b)\big) \tag{101}$$

The Fourier transforms of $\varphi_{k_y,\nu}(y)$ will be denoted by $\widetilde{\varphi}_{k_y,\nu}(k)$. They already appear in the definition Eq. (99) of the augmented spectral density function.

To illustrate the meaning of the spectral density functions, we first consider the case of zero potential modulation. In this case, Eq. (98) describes pure 2D–2D tunneling processes and the spectral density functions at the Fermi energy simply have circular shape. The circles will be broadened by the linewidth Γ. If an appropriate front-gate voltage is applied to the nanostructured front gate, the electron density is modulated under the gated area and a 1DSSL is induced. A typical situation is shown in Figure 50.

The spectral density function A_1 for a 1DSSL, calculated according to Eq. (100) and with the appropriate dispersion relation given previously, is plotted in Figure 51a. The 1DSSL induces a set of Brillouin zone boundaries in k space. In the extended-zone scheme, a cut through the spectral density function at the Fermi energy will consequently appear as a set of circles displaced by the reciprocal lattice vector $G_n = 2\pi n/(a + b)$, as is shown

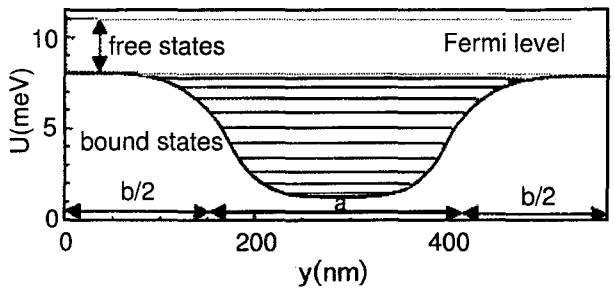

Fig. 50. 1DSSL potential, which is induced by the nanostructured front gate. The total period of the 1DLSSL is equal to $(a+b)$. (Source: Reprinted with permission from [148]. © 1996 American Physical Society.)

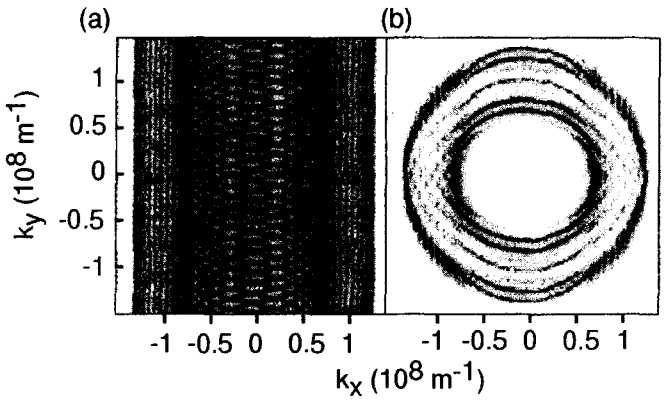

Fig. 51. (a) Cut at the Fermi energy through the spectral density function A_1 of the potential discussed in the text. (b) Same as (a) but for the augmented spectral density function B_1. (Source: Reprinted with permission from [148]. © 1996 American Physical Society.)

in Figure 51. If the 1DSSL potential is sufficiently deep, bound states will also exist in the potential wells. These states have no dispersion in k_y and appear, therefore, as lines parallel to the k_y direction in Figure 51a.

According to Eq. (98), the tunneling differential conductance (TDC) is proportional to the convolution of A_2 and the augmented spectral function B_1. The main features of the measured TDC, shown in Figure 41, are, therefore, due to the overlap integrals contained in B_1. Assume a shape of the confining potential as shown in Figure 50, giving rise to a number of tightly bound Bloch states. The k_y dependence of the bound states will be weak and, consequently, the overlap integrals in the expression for B_1 will essentially be given by the Fourier transform $\tilde{\varphi}_{k_y,\nu}(-k_y)$ of the wave functions corresponding to a single well. The corresponding k-space plot of B_1 is given in Figure 51b. The vertical lines in Figure 51a are now replaced by the modulus squared of the Fourier transforms of the bound state wave functions. In addition to the quasi–bound states, quasi–free states will also be present in the 1DSSL. These give rise to the approximately circular features of B_1 in Figure 51b. To see this, one may approximate the free-state Bloch functions according to Kardynal et al. [148] by Kronig–Penney wave functions. If $\varphi_{k_y,\nu}(y) = A\exp(iky) + B\exp(-iky)$ represents the free states in the ungated regions and $\varphi_{k_y,\nu}(y) = C\exp(iqy) + D\exp(-iqy)$ the free states in the gated regions of the LSSL, it becomes immediately clear that $|\tilde{\varphi}_{k_y,\nu}(-k_y)|^2$ will display peaks at $k_y = \pm k$ and $k_y = \pm q$. If a smooth potential is assumed instead of the rectangular Kronig–Penney potential, these peaks will be broadened but otherwise remain at the same k-space positions. They are responsible for the k and q peaks in the experimental

data shown in Figure 41. Their position in the differential tunneling conductance gives the electron concentration in the gated and ungated regions of the 1DSSL and, consequently, the values of the potential minima and maxima. The positions of the smaller peaks, denoted by arrows in Figure 41, are exclusively determined by the shape of the 1DSSL potential. Excellent agreement between the calculated dI/dV curves and the experimental data can be achieved, if the 1DSSL potential is properly chosen. The potential shown in Figure 50 gives the best fit to the experimental data in a broad range of the top-gate and back-gate voltages V_{sl} and V_{BG}. It has the typical shape expected for confinement potentials induced by the split-gate technique at relatively low gate bias.

With the same sample layout, the voltage applied to the nanostructured front gate can be increased to yield a collector system that consists of a set of separated quantum wires. For this case the analysis of potential shapes can be extended by performing magnetotunneling spectroscopy, just as it was discussed in the previous section [149]. For this purpose, a magnetic field is applied parallel and also perpendicular to the layers of the sample and the equilibrium tunneling conductance dI/dV is measured as a function of the magnetic field B. Typical experimental results are shown in Figure 52 (solid lines).

From the discussion of the transfer Hamiltonian formalism given previously, it is clear that the detailed shape of the confining potential will have a strong influence on the measured tunneling conductance. Hence, a plot of dI/dV versus magnetic field is a unique fingerprint of the confining potential. By incorporating the magnetic field into the calculation of the tunneling differential conductance [Eq. (98)] and by fitting the calculated curves to the corresponding experimental data, a quite realistic picture of the confining potential and the corresponding wave functions can be constructed (see parts e and f of Fig. 52). To

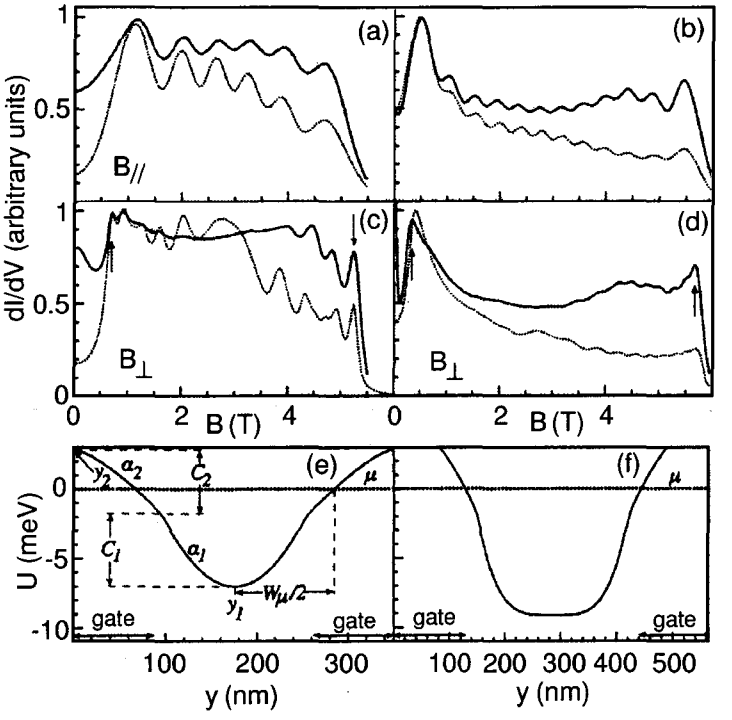

Fig. 52. Experimental (solid lines) and calculated tunneling conductance (dotted lines) for $V_{\mathrm{SL}} = -0.48$ V for $B_{\|}$ (a) and (b) and $B_{\perp}$ (c) and (d). (a) and (c) are the data of a device with a 350-nm superlattice period; (b) and (d) belong to a device with a 570-nm grating period. (e) shows the best fitting potential profile for the 350-nm-period device and (f) for the 570-nm-period device. (Source: Reprinted with permission from [148]. © 1996 American Physical Society.)

obtain better results, the fitting procedure was carried out simultaneously for both magnetic field directions [149].

As shown in Figure 52, the overall features of the tunneling characteristics are well reproduced by the transfer Hamiltonian approach. Parts e and f of Figure 52 show the fitted potential profiles of a 350-nm- and a 570-nm-period device, respectively. For the short-period device, the confining potential is approximately parabolic at the bottom, giving rise to equidistant subband spacing. For higher energies, the nonparabolic widening of the potential will lead to decreasing subband spacings. For the longer-period device, the confining potential is approximately square well like. The reason for this difference is simply the different "overlap" of the electrostatic depletion fields of the two gate electrodes defining the wire region. For the small-period device, the wire region is depleted by the gate voltage from the very beginning, resulting in an approximately cosine-shaped potential. The depletion of the wire region is also reflected by the fact that the bottom of the potential in Figure 52e is higher in energy than in Figure 52f. The electron density in the short-period wire will, therefore, be substantially influenced by the gate voltage. For the long-period wire, this will only be the case at high gate voltages, where the confinement potential will change its character and develop from a flat bottom, nearly rectangular well into an approximately parabolic one. The discussed experiment, therefore, gives a rather direct experimental proof for the validity of the general results obtained by the self-consistent treatment of split-gate-induced confining potentials (see Section 3.2).

7. VERTICAL TRANSPORT THROUGH QUANTUM DOTS

In this section, vertical tunneling through quantum dots will be discussed on the basis of a few instructive experiments. Lateral transport through quantum dots will be ignored almost completely because, owing to the vastness of this field, it is beyond the scope of the present chapter. The lateral transport geometry will only be treated in the context of Coulomb blockade effects, which are most easily introduced and discussed for this case. For a comprehensive treatment of lateral tunneling through quantum dots, see, for example, the book *Single Charge Tunneling* [160], the clear and concise exposition by Meirav and Foxman [161], or the very recent article by Kouwenhoven et al. [162], and, of course, the references cited therein.

In the following, emphasis will again be placed on the question of how to gain some information on the confining potential and the corresponding wave functions in quantum dots. In this respect, it is important to note that the I–V curves of quantum dot devices have to be interpreted with some care. As shown in the previous section, information on confining potentials is obtained from the resonance structures in the I–V curves. However, in the case of 0D tunneling, a wealth of structure is observed in the I–V characteristics that is not necessarily due to resonant tunneling processes in the sense discussed previously for quantum wires. Other physical effects such as tunneling via donor states or Coulomb blockade effects can also lead to a multitude of structures in the I–V curves. The discussion of early experiments on tunneling in quantum dots is, therefore, followed by a brief discussion of these "parasitic" effects and of some instructive experiments that allow us to separate Coulomb blockade–mediated structure from resonant tunneling through quantum dot states.

7.1. First Experiments

The first measurements on vertical quantum dot tunneling were reported by Reed and coworkers [163] in 1988. In this early work, GaAs–AlGaAs–InGaAs–AlGaAs–GaAs double-barrier resonant tunneling diodes (DBRTDs) were used as the basic material. The InGaAs was introduced between the barriers because it allows us to lower the quantum well states

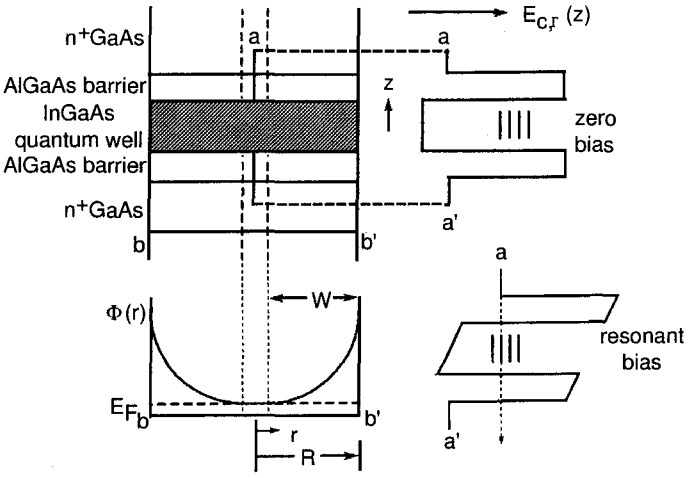

Fig. 53. Left, top: Schematical view of a quantum dot sample realized on double-barrier resonant tunneling diodes. The barriers have a thickness of 40 Å; the undoped InGaAs well is 50 Å wide. On both sides of the barriers, there is an undoped GaAs spacer (100 Å) and a graded region, where the doping is changed from 1×10^{16} cm^{-3} to 2×10^{18} cm^{-3}. The top contact is highly n doped. Left, bottom: Radial component of the confining potential in the pillar-shaped structure. Right: Conduction band profile of the quantum dot structure. The discrete states in the dot are indicated schematically. (Source: Reprinted with permission from [163]. © 1988 American Physical Society.)

with respect to the conduction band edge without changing the width of the quantum well. More details about the sample structure are shown in Figure 53. On these samples, ultrafine pillars were fabricated by electron beam lithography and reactive ion etching. The pillars had a typical diameter of 250 nm and a height of 0.5 μm. The main technological problem in the beginning was the formation of ohmic contacts to the tops of these pillars. For this purpose, the structures were planarized by covering the whole sample with polyimide, followed by a reactive ion etch back. In this way, only the uppermost parts of the pillars were exposed, which finally could be coated by an evaporated gold contact. More details on the fabrication process can be found in [164, 165].

Current–voltage curves were measured at low temperatures and also capacitance measurements were performed to characterize large quantum dot arrays [166]. We restrict the discussion to the I–V measurements that are more instructive in the present context. Figure 54 shows a typical I–V curve of a nanostructured DBRTD. An unstructured sample fabricated on the same wafer behaves "normal" and a clear negative differential resistance region is observed above $V = 0.9$ V.

The nanostructured sample, however, exhibits several extra features at low temperatures. As shown in Figure 54, the expected negative differential resistance region is somewhat less pronounced and a series of equidistant structures in the I–V curve is revealed instead. These peaks are due to resonant tunneling processes through the zero-dimensional states in the quantum "dot" or quantum "disk," which is formed in the InGaAs well cladded by the two AlGaAs barriers and the radial confinement in the small pillar. At higher temperatures, these small peaks disappear again and the I–V curves of the nanostructured DBRTD resemble those of large-area samples. The equidistant peak spacing suggests a parabolic confinement, which can be estimated quantitatively using the following considerations: The edge depletion width in the pillars, W, can be derived if one assumes that the current density in the small pillars is the same as in the large-area samples. Because the Fermi level pins at the midgap position of $\Phi_T = 0.7$ eV, the confining potential can be written as

$$\Phi(r) = \Phi_T \left[\frac{1 - (R - r)}{W} \right]^2 \tag{102}$$

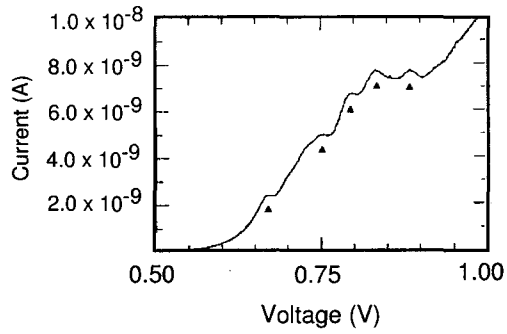

Fig. 54. Typical current–voltage characteristics of a single quantum dot measured at liquid helium temperatures. (Source: Reprinted with permission from [163]. © 1988 American Physical Society.)

where r is the radial coordinate, R is the geometrical radius of the pillar, and W is the depletion width ($R - W \leqslant r \leqslant R$). For $R \approx W$, the corresponding energy spacing between the single electron levels is given by

$$\Delta E = \left(\frac{2\Phi_T}{m^*}\right)^{1/2} \frac{\hbar}{R} \tag{103}$$

This yields a value of 26 meV for the 0D states in the InGaAs well, which can be compared with the peak positions in the measured I–V curve. If one assumes that the applied voltage drops homogeneously across the whole structure, approximately half of the voltage will drop between the emitter and the confined states at the center of the well. As a consequence, the measured energy spacing ΔE is equal to e times half the voltage spacing ΔV between the peaks. One obtains a subband spacing of approximately 25 meV from the experimental I–V curve, showing that the preceding considerations give a fairly accurate description of the situation.

For the previous analysis, however, an important assumption was made that caused some confusion in the early stages of low-dimensional tunneling experiments. As already stated by Reed et al., their samples represent a system with electrons in the pillar traveling through a freestanding quantum wire, tunneling through a quantum dot, and continuing to flow in another quantum wire. The correct description of this 1D–0D–1D tunneling process necessitates the calculation of transmission coefficients that takes the dimensionality of the involved states into account [167–169].

In the previous experiment, however, excellent agreement with the experiment is achieved by simply assuming that resonance structures in the I–V curve occur whenever the Fermi energy in the emitter electrode is energetically aligned with a zero-dimensional state in the dot. Because this assumption is only true if the emitter and collector electrodes do not contain any quantized states and can, therefore, be considered as perfectly three-dimensional systems, one might conclude that the sample quality was too poor to observe the influence of the different dimensionality in the emitter and collector electrodes.

At this point, it should be mentioned, however, that besides poor sample quality there are also several other possibilities for the missing evidence of 1D–0D–1D tunneling processes even if the sample quality is sufficiently good. To illustrate this, we just consider one possible example: To improve the sample quality, undoped spacer layers were introduced in front of the double-barrier structure, which under bias form a triangular potential well, resulting in electron confinement in the growth direction (cf. Fig. 39b for a similar situation in the 1D–1D case). Together with the radial confinement caused by the etching process, the emitter itself will represent a second quantum dot in front of the double barrier, which, in principle, should lead to 0D–0D–1D tunneling behavior. Because confinement in the growth direction is weak, many closely spaced subbands will exist in this direction,

each of them having a ladder of corresponding (and also closely spaced) 0D states resulting from the lateral confinement. These states will be broadened at finite temperatures and in the presence of a certain amount of scattering. The overlap of the resonant peaks and the scattering-induced broadening will smear out the expected fine structure completely and only the main resonances resulting from the 0D states in the InGaAs well will be dominant. Thus, proper sample design is required if tunneling processes between states of different dimensionality are to be studied on quantum dot samples.

Tarucha et al. [170] were the first to report experimental evidence of the expected dimensionality effects for the emitter electrode in DBRTDs. In their work, focused ion beam implantation is used to define rectangular quantum dot or quantum wire structures of variable size. This also allows one to vary the dimensionality as well as the geometry of the nanostructured collector system and enables studies of tunneling processes through 0D and 1D states in rectangular geometry. Although the experimental results look very similar to the results of Reed et al., additional spectral features in the measured I–V curves suggested a mixing of the 1D or 0D states between the barriers and the 2D states in the contacts.

7.2. Lateral and Vertical Transport through Quantum Dots: Coulomb Blockade Effects

7.2.1. Coulomb Blockade in Planar Quantum Dots

In the previous section, vertical resonant tunneling through quantum dots was used for an investigation of the energy spectrum caused by 0D lateral quantization. The structure observed in the tunneling characteristics was thereby assigned to resonant tunneling processes via 0D states, just as in the case of quantum wires discussed in Section 6. For quantum dots, especially for those containing only a few electrons, this simple interpretation can be obscured by other mechanisms, which will also lead to structure in I–V characteristics. One of them, the so-called Coulomb blockade, will be the topic of the present section. The following discussion will be short and very elementary. The reader particularly interested in an in-depth exposition of Coulomb blockade and related effects is referred to the existing excellent reviews on this subject (see, e.g., [160–162]).

The Coulomb blockade effect in semiconductor nanostructures was first demonstrated and subsequently extensively studied on planar quantum dot devices, defined by properly designed split-gate geometries. Because the particular nature of the Coulomb blockade is most easily understood for these planar devices, we make a short digression from our discussion of vertical transport. The typical features of a planar quantum dot are depicted in Figure 55. The two constrictions formed by the gates G0, G1, and G2 define together with the independently biased plunger gate GP a small electron island within the underlying

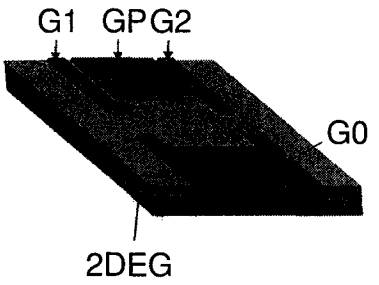

Fig. 55. Typical planar quantum dot geometry, which consists of the metallic gate areas G0, . . . , G2, GP, and the two-dimensional electron gas underneath. (Source: Reprinted with permission from [161].)

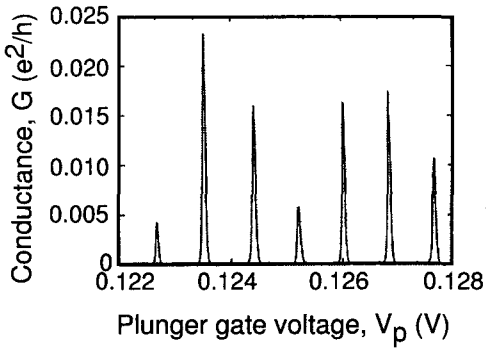

Fig. 56. Typical data showing the conductance of a planar quantum dot as a function of the plunger gate voltage V_p. The measurement was carried out at a temperature of $T = 100$ mK. (Source: Reprinted with permission from [161].)

2DEG. The point contacts between G0, G1, and G2 can be narrowed until they form low-energy barriers, through which electrons can be transferred by tunneling processes. Detailed information on the potential distribution and the corresponding electron energy spectrum can be obtained from self-consistent calculations [171]. It is also worth noting that, if the narrow constrictions are operated below pinch-off voltage, the planar dot structure of Figure 55 can be regarded as a short quantum wire, displaying transport properties characteristic of ballistic transport, such as, for example, quantized conductance (for details, see [160, 161]).

The plunger gate GP is a very common feature of all planar quantum dot structures [172–174]. It is coupled capacitively to the electron island and is used to change the electron concentration in the dot as well as the confinement strength. The relation between the plunger gate voltage V_p and the electron concentration is found to be linear. In a properly designed planar structure, the tunneling barriers at the entrance and exit of the dot are not influenced by the plunger voltage.

If the current through the dot is measured as a function of the plunger voltage at low temperatures (usually below 0.5 K) and a given source drain bias V_{DS}, the conductance $G = I/V_{DS}$ displays a series of sharp spikes, as shown in Figure 56. These spikes are called *Coulomb blockade oscillations* and they occur whenever an additional electron is added to a low-capacitance, few-electron system. Coulomb blockade oscillations were first observed in a system of metallic junctions [175]. For the case of semiconductor quantum dots, they were theoretically explained by Beenakker and van Houten [176, 177] as single-electron charging of the dot.

For an elementary explanation of the basic physics of the Coulomb blockade effect, we assume that N electrons are present in the dot, leading to a total charge of $Q = Ne$. Because the plunger is capacitively coupled to the dot, Q can be varied by varying V_p. However, owing to the discrete nature of the electron charge, Q must increase in discrete steps when the plunger gate voltage is swept continuously. The electrostatic energy of the dot is given by

$$E(N) = \frac{(Ne)^2}{2C} - \varphi Ne \tag{104}$$

where the first term represents the capacitive charging of the dot and the second term is the potential energy. C is the total capacitance of the dot with respect to its surroundings and φ is the electrostatic potential. If the plunger gate is assumed to be the only gate with significant capacitive coupling to the dot, one has $C = C_p$ and $\varphi = V_p$.

The previous equation can be easily solved for those integer values of N minimizing $E(N)$ for a given value of V_p, which immediately leads to the staircase relationship

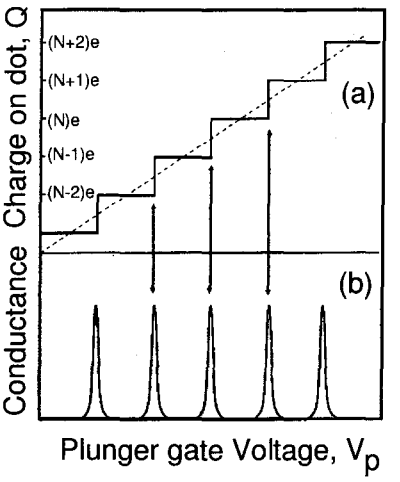

Fig. 57. (a) Charge on the quantum dot according to the relation $Q = CV_p$ (dashed line) and single electron charging (solid line). (b) Schematic plot of the conductance showing peaks each time an electron is added to the system. (Source: Reprinted with permission from [161].)

depicted in Figure 57a. The situation where a new electron is added to the dot corresponds to $E(N) = E(N+1)$. This occurs periodically at plunger gate voltages given by

$$V_p = \frac{e(N+1/2)}{C_p} \tag{105}$$

If V_p is adjusted according to this relation, the corresponding charge on the dot would be given by a half-integer multiple of e. Because half-integer values of e cannot occur, this means, of course, that the actual lowest energy state is degenerate and corresponds to either N or $N+1$ electrons. At the gate voltage given by Eq. (105), the dot is thus free to fluctuate between the N or $N+1$ electron state.

If a current flows through the dot, an electron must cross the barrier at the entrance and be able to stay inside the dot for a finite amount of time before exiting it through the other barrier. It is clear that this can happen only for those values of V_p where charge in the dot can fluctuate between Ne and $(N+1)e$, that is, where electron transfer into the dot is possible for constant energy. Away from these so-called charge degeneracy points, the electron transfer is suppressed by the Coulomb charging energy. This explains the occurrence of the Coulomb blockade oscillations shown in Figure 56.

The electrostatic charging energy necessary to add another electron to the dot is equal to e times the voltage spacing between two neighboring charge degeneracy points: $e(V_p^{N+1} - V_p^N) = e^2/C$. The resonances in the conductance are periodic and have a voltage separation of $\Delta V_p = e/C_p$. A detailed theoretical explanation of the exact shape of Coulomb blockade resonances and also of some additional fine structure observed in the experiment is rather complex and takes tunneling rates, bias voltages, and temperature effects into account [178, 179]. Coulomb blockade effects completely disappear if the temperature exceeds the Coulomb charging energy, that is, for $k_B T \approx e^2/C$.

7.2.2. Excitation Spectrum

Consider a situation where the plunger gate voltage and, hence, the electron concentration in the dot are kept constant. Electrons can now be injected into the dot by sweeping the voltage V_{DS} applied across the dot [180–182]. The schematic band diagram in Figure 58 is intended to illustrate this situation. Because of 0D confinement, a series of

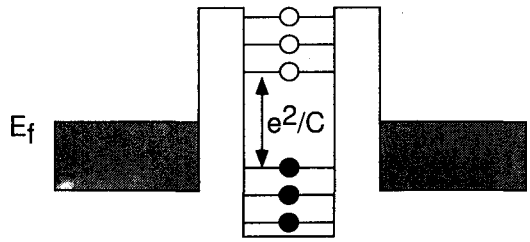

Fig. 58. Conduction band profile of a quantum dot, showing both occupied and empty levels in the dots having a Coulomb gap in between. (Source: Reprinted with permission from [161].)

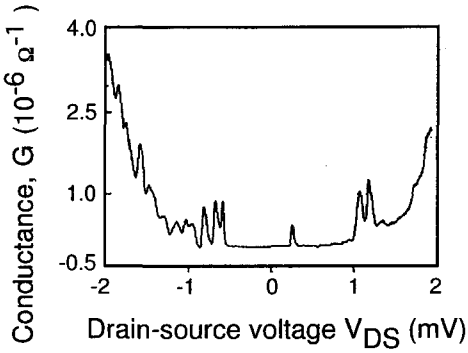

Fig. 59. Differential conductance dI/dV_{DS} as a function of V_{DS}. The flat region at zero bias reflects the Coulomb gap. The peaks are due to higher energy states in the dot. (Source: Reprinted with permission from [181]. © 1993 American Physical Society.)

equidistant electron levels exists in the dot. Occupied and unoccupied levels are separated by the Coulomb blockade gap e^2/C.

As long as the applied voltage is so small that the corresponding electron energy is below the electrostatic charging energy, electrons are not allowed to tunnel into the dot and the conductance is zero. With increasing Fermi level on the left-hand side, current begins to flow as soon as the Coulomb gap is overcome and E_F is aligned with the lowest empty level of the dot. The differential conductance dI/dV_{DS}, plotted as a function of the source drain bias, therefore, displays a flat region around $V_{DS} = 0$, which is a direct consequence of the Coulomb gap, followed by a number of resonant structures associated with the quantized levels of the dot. An example of this so-called *excitation spectrum* of the dot is shown in Figure 59.

Although it is clear from the preceding arguments that the peaks in dI/dV_{DS} are associated with higher energy levels inside the dot, a quantitative analysis of the peak positions is nevertheless difficult because of the interplay between resonant and Coulomb blockade effects. There will be a one-to-one correspondence between the peaks in the excitation spectrum and the quantum dot levels only if just one electron at a time is allowed to tunnel through the dot. Even if there are many empty states available, an additional electron will be able to enter the dot only if it has enough energy to overcome the additional Coulomb barrier of the first electron *and* if it is in resonance with an empty state of the dot. The same arguments are valid for all other electrons that could enter the dot at sufficiently high bias voltages. Taking into account that the tunneling rates and dwell times will be different for electrons in different 0D states, it is easy to imagine that a quantitative analysis of the subband energies in the presence of Coulomb blockade effects will not be a straightforward matter.

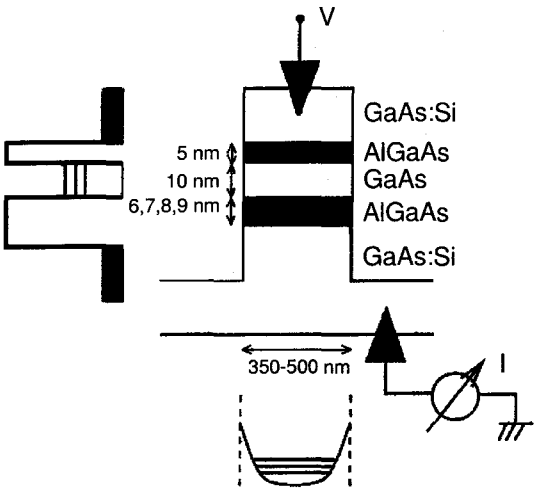

Fig. 60. Cross section of a double-barrier tunneling device used for single-electron tunneling spectroscopy. (Source: Reprinted with permission from [185].)

7.2.3. Tunneling and Coulomb Blockade Effects in Vertical Quantum Dots

Coulomb blockade effects in vertical transport through quantum dots were first demonstrated by capacitance spectroscopy on strongly asymmetric double-barrier structures [183, 184]. In vertical tunneling experiments, it is possible to detect them also if samples with a relatively wide central well and asymmetric barriers are used [185, 186]. A cross section of such a double-barrier tunneling device is shown in Figure 60. For the depicted sample structure, the emitter and collector electrodes are degenerate at low temperatures and, therefore, contain no quantized states. This is an important point concerning the interpretation of the resulting tunneling spectra because 0D states in the emitter electrode would cause a multitude of additional structure in the corresponding I–V curves in zero [187] as well as in nonzero magnetic fields [167, 188]. Some theoretical considerations concerning this topic are found in [168, 169, 189–191].

Owing to the asymmetric conduction band profile of this 3D–0D–3D tunneling structure, the I–V characteristics exhibit an asymmetric bias voltage dependence, because completely different physical processes dominate the measured I–V curves, depending on the polarity of the bias voltage. A schematical view of the band diagram under bias and the corresponding I–V curves are shown in Figure 61. For positive bias direction (Fig. 61a), the emitter barrier is thicker than the collector barrier, and, as a consequence, the tunneling rate through the emitter barrier will be low compared to the tunneling rate out of the central well. It is, therefore, reasonable to expect that the electrons will be transferred through the central well one by one and all structures in the measured I–V curves are due to new channels for tunneling electrons, which open as soon as the emitter Fermi level matches their energetic position.

For opposite bias, the collector barrier is thick and the tunneling rate out of the dot is small. Thus, charge will accumulate inside the dot and Coulomb blockade effects can be expected. As shown in Figure 61b, one indeed observes a Coulomb staircase, which is shifted in voltage because of the confinement energy inside the dot [192–194]. Note that the step height is dominated by the transmission coefficient of the collector barrier. Systematic studies of devices with different barrier thickness have shown that the step height increases exponentially with increasing barrier thickness [195].

As shown by Nomoto et al. [196] for a vertical double-dot system [197], both the excitation spectrum and the Coulomb staircase can be used to extract some information on the

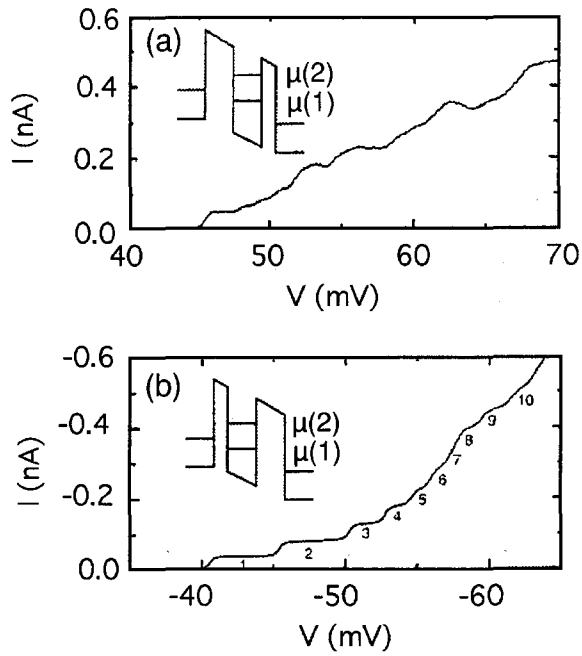

Fig. 61. I–V curves measured on vertical quantum dots with asymmetric barriers. (a) Situation for positive bias and thick emitter barrier (excitation spectrum); (b) situation for the thick collector barrier (charging regime). (Source: Reprinted with permission from [185].)

confining potential in the dot. We outline the underlying ideas in the following considerations, which refer to an asymmetric tunneling system similar to that shown in Figure 60. Assume a cylindrical symmetric confinement whose radial part is given by a harmonic oscillator potential: $V(r) = m\omega_0^2 r^2/2$. Here, r is the radial coordinate, $\omega_0 = 1/R\sqrt{2\Phi/m^*}$, $\Phi = 0.7$ eV is the Fermi level pinning at the surface, and R is the lithographically defined radius of the diode. As mentioned earlier, this approximation will give a fairly correct description only for a certain range of dot radii R. In the limit of very small R, the diode will be totally depleted, whereas for relatively large values of R the potential will not be parabolic but rather exhibit a flat center part. For a parabolic potential, the eigenstates can be easily calculated, and, provided the scaling factor between electron energy and sample bias is known, it should yield the peak positions in the excitation spectrum correctly. For the forward bias situation of Figure 61a, a direct comparison of the outlined simple calculation with the experimental excitation spectrum is feasible and can be used to determine the strength of the confinement potential. From the latter, the radial extension of an electron in the ground state can be estimated according to $r_{\text{wave}} = [\hbar/(m^*\omega_0)]^{1/2}$.

As shown by Nomoto et al. [196], this value is in good agreement with the radius of the internal capacitor, which can be estimated from the (reverse bias) Coulomb staircase as follows. The dot is considered as a planar capacitor with circular electrodes. The corresponding capacitance is simply given by $C = \varepsilon\varepsilon_0\pi r_{\text{cond}}^2/d$, where ε is the permittivity of the AlGaAs barrier and d is the corresponding thickness. The radius r_{cond} of this capacitor is defined as the radius of the conducting area in the dot. According to the orthodox theory of Coulomb blockade, the width of a current step, ΔV, is always equal to $\Delta V = e/C$, which offers the possibility of determining the junction capacitance directly from the voltage positions of current steps. By inserting the preceding expression for the capacitance and solving for the radius r_{cond}, good agreement with the radius of the wave function in the ground state r_{wave} is obtained.

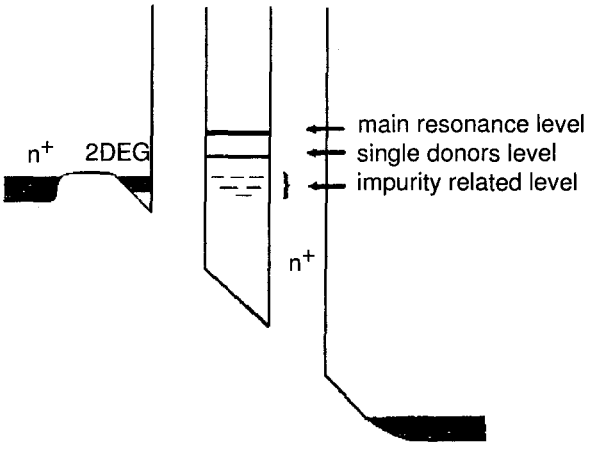

Fig. 62. Energy band diagram of a resonant tunneling device, where a layer of donors was incorporated between the barriers. Tunneling occurs from the two-dimensional electron gas via the main resonance level and also via single-donor and impurity-related levels. (Source: Reprinted from [199]. © 1994 American Institute of Physics.)

7.3. Tunneling via Zero-Dimensional Donor States

Besides quantized states and Coulomb blockade effects, tunneling processes through single impurities can also result in additional resonance structures in the measured I–V curves of a quantum dot. Although tunneling through donor states is not at all restricted to 0D systems, it is treated here in the framework of quantum dot tunneling for two reasons. First, the donors themselves can be considered to be natural 0D systems, giving rise to a set of localized states that can serve as some kind of collector in tunneling experiments. Second, as will be shown that the natural way to achieve a better understanding of the tunneling through donor states is to reduce the number of donors involved. This can be attained by reducing the lateral dimensions of the underlying tunneling devices, thereby entering the quantum dot regime.

The first detailed investigations on this subject, which we will discuss briefly at the beginning of this section, were performed on large-area double-barrier resonant tunneling diodes (DBRTDs). As mentioned earlier, DBRTDs are often equipped with undoped GaAs spacer layers in front of the barriers in order to enhance the resolution of the tunneling experiments. Provided the GaAs spacer is sufficiently thick, a triangular well is formed in front of the barriers under bias, leading to a two-dimensional accumulation layer of electrons as shown in Figure 62. Because the electron wavevector parallel to the barrier is conserved during a tunneling process, the transmission coefficient of the barrier only depends on the electron wavevector component k_z perpendicular to the barrier. The wavevector components parallel to the barrier do not influence the transmission coefficient at all. For the sample structure under consideration, this means that resonances in the I–V curves are only expected when the edge of the 2D subband in the emitter (and *not* the Fermi level as in similar samples used, e.g., by Reed et al. [163]; see Section 7.1) is in exact coincidence with the main resonance levels within the double barrier. Because the linewidth of the resonances in a tunneling I–V curve is limited only by the natural width of the 2D subband, the resolution of fine structure in the I–V curves is enhanced compared to those cases where the linewidth is determined by the distribution of electrons at the Fermi energy. By proper design, it can be achieved that only one subband is occupied in the 2D emitter, leading to an almost perfectly monoenergetic energy distribution in tunneling direction. Note that for a tunneling process starting from a 2D emitter the shape of the resonance is to first order independent of the temperature. This is easily understood from the fact that the main effect

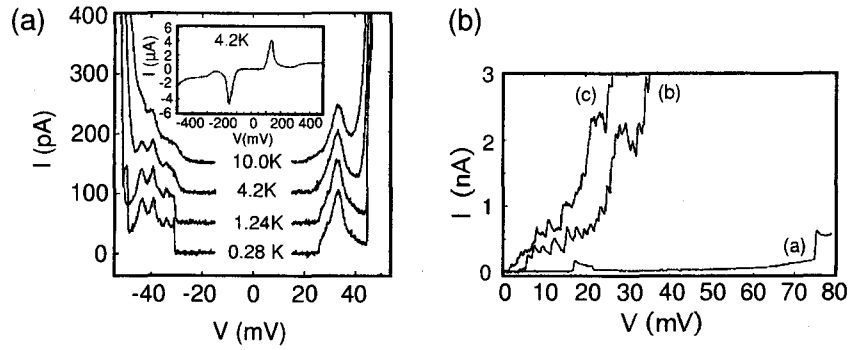

Fig. 63. Left: I–V curves of a DBRT device as a function of temperature. Right: I–V curves of a DBRT device as a function of doping level: (a) undoped device, (b) 4×10^{13} m^{-2}, and (c) 8×10^{13} m^{-2}. (Source: Reprinted from [199]. © 1994 American Institute of Physics.)

of temperature is to broaden the Fermi distribution function. For a 2D emitter, this only changes the momentum distribution parallel to the barriers in the emitter, which obviously has no influence on the transmission coefficient in the tunneling direction.

The strongly enhanced energy resolution obtained for samples with a 2D emitter was exploited by Geim and co-workers [198–200] to investigate tunneling processes through single-donor related states on *large-area* DBRTDs with a delta-doped layer incorporated between the double barriers. Figure 63 shows typical data. As seen from the inset of Figure 63 (left) the main resonance of the I–V curve has the commonly expected form. Note that because of the two-dimensional emitter electrode the peak-to-valley ratio of the main resonances is much larger than for the samples used by Reed et al. [163], where the electrons in the emitter showed 3D behavior. In the low-bias region of the I–V curve, pronounced additional fine structure is revealed, which is temperature dependent and which can unambiguously be demonstrated to be impurity related. Consider Figure 63 (right), where the I–V curves of three different samples are plotted. Curve a corresponds to an undoped sample and exhibits no fine structure. This is in contrast to curves b and c, which correspond to two different donor concentrations in the δ-doping layer.

It was shown by Geim and co-workers that the observed effects can be quantitatively explained if donor pairs of random separation ("donor molecules") are made responsible for the fine structure in the tunneling I–V. Because of the relatively low donor concentration in the well, the average donor separation is in the range of 0.1 to 0.5 μm. Consequently, only a small number of donor molecules will exist in a tunneling device with a mesa diameter of typically 10 μm. As shown by Geim and co-workers [198], only donor molecules formed by nearest-neighbors will play a role at the used doping level. Larger clusters would lead to binding energies too small to account for the observed peak positions. The multitude of fine structures in the tunneling characteristics then originates from the random distribution of the relative nearest-neighbor donor separation and the corresponding multitude of possible energy states. Although the model is relatively simple, quantitative simulations showed excellent agreement with the measured tunneling current in the low-bias regime.

The next step toward a more advanced investigation of impurity-related tunneling was initiated by the introduction of "squeezable" quantum dot structures with side-gate geometry. The sample design, originally developed by Kinard et al. [201] and used later on by Eaves and co-workers [202–204] for detailed studies of tunneling via single-donor states, is shown in the inset of Figure 64. The lithographically defined width of the active device region is 1 μm^2. In contrast to the previously discussed sample structures, the well enclosed by the AlAs barriers is *not* intentionally doped. The lateral confinement, that is, the effective width of the current path can be controlled by the electrically tunable side-wall depletion. By determining the current density in the device, the scaling factor of the actual

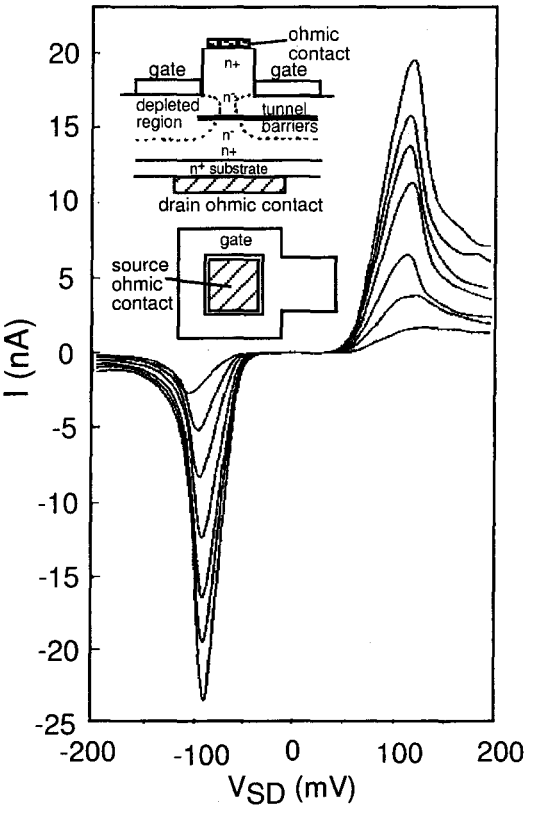

Fig. 64. I–V curves of a squeezable quantum dot structure. The different curves show the influence of the applied side-gate voltage. (Source: Reprinted with permission from [202].)

conducting area as a function of the side-gate voltage can be obtained. The conducting area is found to decrease down to 0.1 μm^2 for a gate bias of -5 V.

Figure 64 shows the I–V curves obtained for various values of the side-gate voltage. The main resonance peak current is seen to decrease when the conducting channel is narrowed. An interesting feature is the asymmetry between the forward and the reverse bias region which is induced when the tunneling region is squeezed. This behavior can be explained in terms of a lateral variation of the potential drop across the AlGaAs barriers. To see this, consider the schematic view of the sample cross section shown in Figure 65. Figure 65a refers to zero side-gate voltage. The point of maximum depletion is seen to be slightly above the tunnel barriers. Parts b and c of Figure 65 show the equipotential lines for forward ($V > 0$) and reverse bias ($V < 0$), respectively. The solid circles represent the electron accumulation layer from which the electrons are injected into the double barrier. The important point is that for positive bias the equipotential lines converge in the direction of the electron flow upwards in Figure 65b, implying that the voltage drop between the accumulation layer and the quantum well is larger at the center of the device than at the edge. In reverse bias, the equipotential lines diverge in the direction of the current flow and the potential difference between the accumulation layer and the quantum well does not vary over the width of the accumulation layer. The lateral variation of the voltage drop in forward bias means that the edge of the device goes on resonance at a higher bias than the center of the device (see Fig. 65b). As a consequence, the main resonance is smeared out and the peak-to-valley ratio decreases faster for positive side-gate voltages.

The second main feature of these squeezable dots is revealed when the I–V curves close to threshold are considered as they are plotted in Figure 66. A series of peaks is clearly

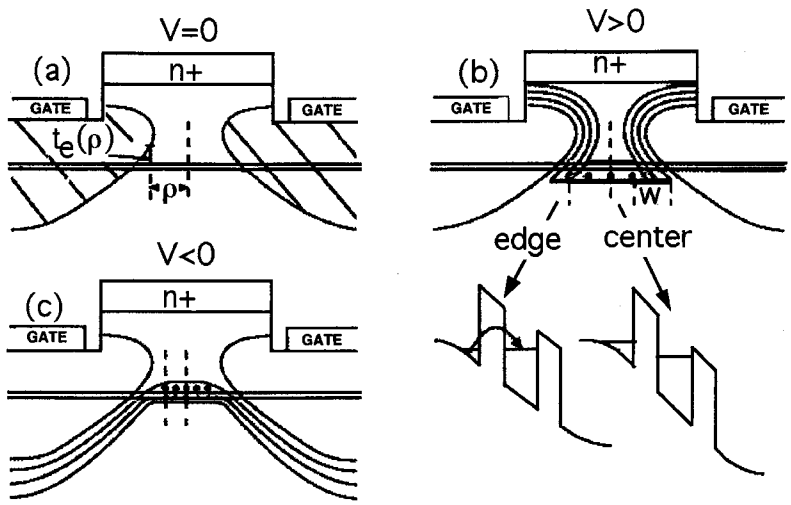

Fig. 65. Schematic diagram of the equipotential lines and depletion regions for a side-gated double-barrier resonant tunneling diode. (a) $V = 0$, (b) $V > 0$, and (c) $V < 0$. In (a), the cross-hatched area represents the region that is depleted by the gate. In (b), the conduction band profile indicates how the device can be on resonance at the edge, but not at the center. (Source: Reprinted with permission from [202].)

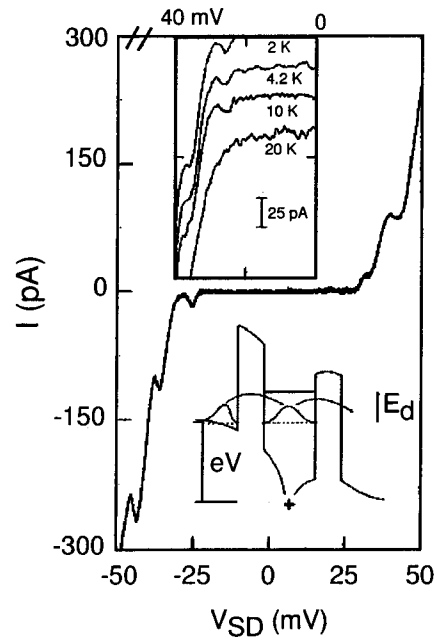

Fig. 66. I–V curve close to threshold for $V_g = 0$ V measured at $T = 39$ mK. The inset shows I–V in reverse bias for temperatures of $T = 2$, 4.2, 10, and 20 K. (Source: Reprinted with permission from [202].)

observed for both bias directions although for reverse bias the peaks are better resolved. These peaks are a universal feature and also occur for different samples at similar voltage positions, but always below the onset of the main resonance. They are attributed to energy levels lying below the first confined state in the well. The striking feature of these peaks is, however, that their position is independent of the side-gate voltage and, as can be seen in the inset of Figure 66, they are also relatively insensitive to temperature. Thus, quantum

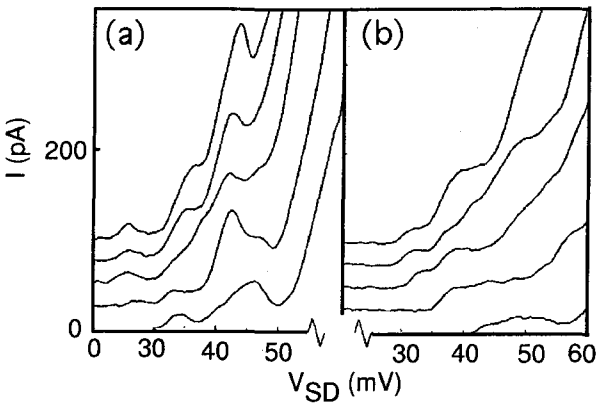

Fig. 67. Dependence of $I(V)$ on the applied side-gate voltage in reverse bias (a) and forward bias (b) for voltages of $V_g = 0$, 1, 1.5, 2.25, and 3 V from top to bottom. (Source: Reprinted with permission from [202].)

confined states or Coulomb blockade effects cannot be made responsible for the structures in the low-bias range; otherwise, they would occur at a position above the main resonance and show a distinct voltage dependence.

Tunneling via a local inhomogeneity, such as a donor impurity unintentionally incorporated in the well between the AlAs barriers, provides a possible explanation for the observed behavior. In contrast to the large-area DBRTDs considered previously, the gated structures now offer the possibility of probing the spatial extent of these donor states using the following considerations. A peak in the I–V curves will be unaffected until the depletion edge impinges on the region of the corresponding localized state, through which the electrons tunnel. If the depletion zone moves across the active area of the localized state, the amplitude of the corresponding resonance peak will decrease, because electrons are prohibited from entering the depletion zone. Thus, the current path for electrons flowing through this impurity state becomes smaller. If the side-gate voltage becomes large enough, the localized states will lie totally within the depletion region and the corresponding resonance will be quenched. This is shown in Figure 67, where the near-threshold I–V curves are given for various side-gate voltages. If the effective diameter d of the resonant tunneling device as a function of the side-gate voltage is known, the spatial extent Δx of such an impurity-related level can be determined. If V_{g1} is the highest voltage for which the resonance peak is still unaffected and V_{g2} is the lowest voltage, where the peak is totally suppressed, one estimates $\Delta x = \frac{1}{2}[d(V_{g1}) - d(V_{g2})]$. For the lowest peak in the I–V curves of Figure 67, one obtains, for example, a spatial extension of approximately 30 nm, which is close to the value for a single-donor bound state, expected from a simple first-principles calculation.

In the preceding experiment, donor-related tunneling was investigated using squeezable quantum dot devices, which, however, showed no sign of resonant tunneling via 0D states. It was shown by Blanc et al. [205], however, that the inverse situation can be achieved by some modifications of the device design. By growing a larger spacer layer in front of the double barrier (7 nm instead of 3.4 nm in the case of Eaves and co-workers [202]), the unintentional incorporation of shallow donors in the quantum well region is largely suppressed. A reduction of the mesa size down to 0.1 μm leads to relatively high 0D quantization energies, which facilitates the observation of resonant tunneling via quantized states.

With increasing side-gate voltage, the main resonance peak current is reduced in analogy to the previously discussed experiment, but no asymmetry is observed for forward and reverse bias. In contrast to the previous experiment, no evidence of donor-related tunneling processes is found. The low-temperature conductance exhibits a series of well-resolved

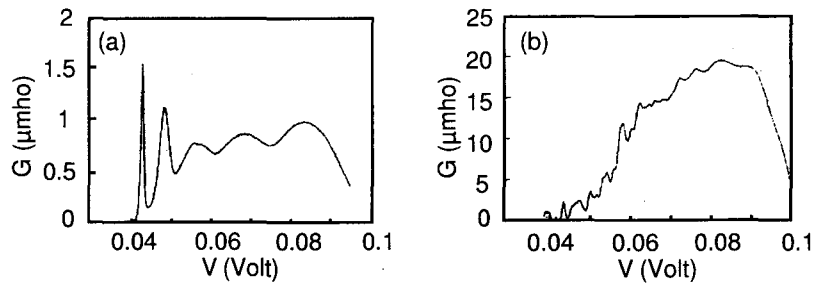

Fig. 68. Conductance measured at 40 mK for a device with a diameter of 0.2 μm ($V_g = -0.2$ V) (a) and a device with a nominal diameter of 0.8 μm and $V_g = 0$ V (b). The resonance structures are due to resonant tunneling via 0D states. For the smaller device (curve a), the energy spacing of the quantized states is considerably enhanced compared to the larger device (curve b). (Source: Reprinted from [205], with permission of Elsevier Science.)

peaks (Fig. 68), which are attributed to resonant tunneling via 0D states. This is confirmed by the observed dependence of the I–V characteristics on gate voltage as well as magnetic field.

7.4. 0D–2D Tunneling

So far, the presented experiments on quantum dot tunneling were not or only superficially analyzed in terms of the properties of the confinement potential defining the dot. Whenever an attempt of a quantitative comparison between experiment and calculation was made, the confinement was assumed to be parabolic and subband energies or the spatial extent of electronic wave functions were calculated within this assumption. The transfer Hamiltonian formalism, which was introduced in Section 6.2, can also be employed to gain more detailed information on the shape of the quantum dot potential from 0D–2D tunneling processes. This will be discussed in the following for tunneling experiments performed using the double-heterostructure layout already treated in Sections 6.1 and 6.3 in the context of 1D–2D tunneling. The same sample structure turned out to be also suitable for the fabrication of a 0D–2D tunneling device [206]. For this purpose, the upper (emitter) channel is nanostructured into quantum dots as schematically depicted in Figure 69. The dot array can be fabricated by laser holography using a double-exposure technique. In order to deplete the accumulation layer between the dots, the structures were wet chemically etched 300 Å deep into the GaAs cap layer. An ohmic contact to the dots is obtained by evaporating a Au/Ge electrode covering the dot array. The experimental data shown in Figure 70 were obtained for a period of the dot array of $a = 350$ nm. The corresponding dot diameter was estimated to be approximately $a/2$.

As discussed in Section 6.1, the applied bias voltage can be assumed to drop exclusively across the potential barrier separating the 2D collector from the 0D islands. A bias voltage ΔV_b is, thus, equivalent to a relative energetic shift of the 0D states by $\Delta E = e\Delta V_b$. A negative bias voltage $V_b < 0$ corresponds to tunneling processes from a 0D state into a 2D subband of the inversion channel. The band structure of the biased sample is shown in Figure 69b for both the etched and the nonetched regions (upper and lower parts, respectively).

Some experimental results are plotted in Figure 70. Part a of this figure shows the dI/dV_b characteristics of the nanostructured (0D–2D) sample for various temperatures in the range between $T = 1.7$ K (curve 1) and $T = 40$ K (curve 12). For reference purposes, the dI/dV_b characteristics of an unstructured sample are plotted in part b of the figure for two temperature values $T = 1.7$ K (curve 1) and $T = 40$ K (curve 2). All resonance peaks of the (0D–2D) dI/dV_b characteristics show a strong dependence on temperature.

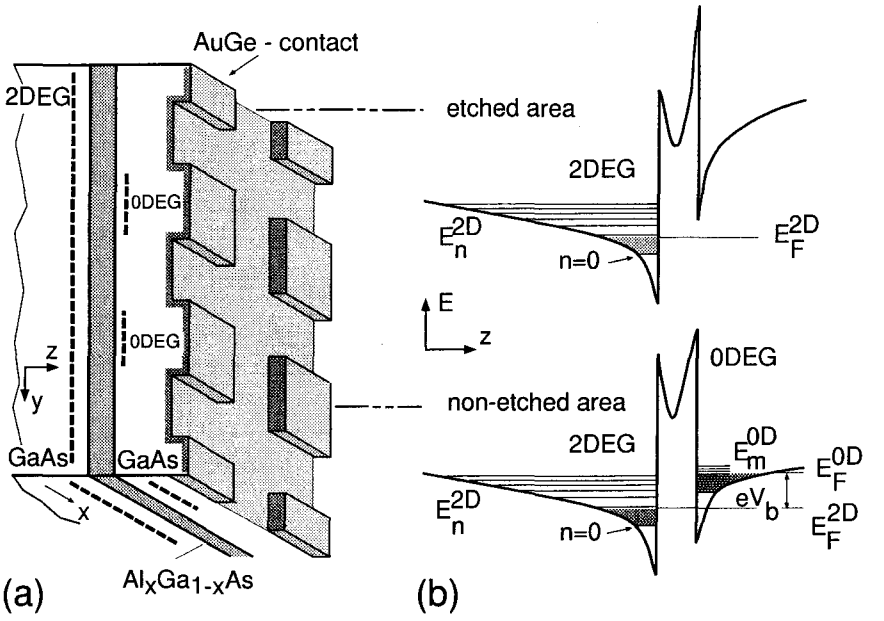

Fig. 69. (a) Schematic view of a 0D–2D sample. (b) The corresponding conduction band profile for the etched and nonetched areas of the sample. (Source: Reprinted with permission from [24].)

Above $T = 4.2$ K (part a, curve 2), the number of resolved resonance structures is already considerably reduced. A further increase in temperature results in a monotonic broadening of the resonance structures, accompanied by a decrease in the peak amplitudes. Generally, the resonance positions observed for $V_b < 0$ are slightly shifted toward more negative bias voltages. This behavior, which also occurs for the subband resonances of the (2D–2D) tunneling characteristics, is due to the thermally activated occupation of the first excited subband in the inversion channel causing a modification of the self-consistent potential profile. In both parts a and b of Figure 70, the positions of the (2D–2D) subband resonances are denoted by arrows.

Similar to the 1D–2D tunneling processes discussed in Section 6.3 it can be shown that the structures in the measured tunneling characteristics can be traced back to the form of the overlap integral formed by the initial and final states. To see this, we introduce cylinder coordinates and write the wave functions for the collector and the emitter system in the form

$$\begin{aligned} \text{2DEG}: \quad & \Psi_{\mathrm{I},\nu}^{2\mathrm{D}} = \frac{1}{\sqrt{A_{\rho\varphi}}}\psi_{\mathrm{I},\nu}(z)\frac{1}{\sqrt{2\pi}}\exp(im_{\mathrm{I}}\varphi)J_{m_{\mathrm{I}}}(k_{\parallel}\rho) \\ \text{0DEG}: \quad & \Psi_{\mathrm{A}}^{0\mathrm{D}} = \frac{1}{\sqrt{A_{\rho\varphi}}}\psi_{\mathrm{A}}(z)\frac{1}{\sqrt{2\pi}}\exp(im_{\mathrm{A}}\varphi)\varphi_{n_{\mathrm{A}},m_{\mathrm{A}}}(\rho) \end{aligned} \tag{106}$$

In the expression for $\Psi_{\mathrm{A}}^{1\mathrm{D}}$, n_{A} represents the radial and m_{A} the azimuthal quantum number. Because prior to the nanofabrication process the upper 2DEG (accumulation layer, index A) contains only one occupied subband in the z direction, these two quantum numbers are sufficient to describe the 0D states of the quantum dot system. The wave functions of the subbands in the lower 2DEG (inversion layer, index I) are given by $\Psi_{\mathrm{I},\nu}^{2\mathrm{D}}(\rho, \varphi, z; m_{\mathrm{I}})$. Here, ν is the 2D subband index and m_{I} takes the degeneracy of $E_{\parallel}$ (energy of the motion parallel to the interface) into account. $A_{\rho\varphi}$ represents the normalization area in both systems.

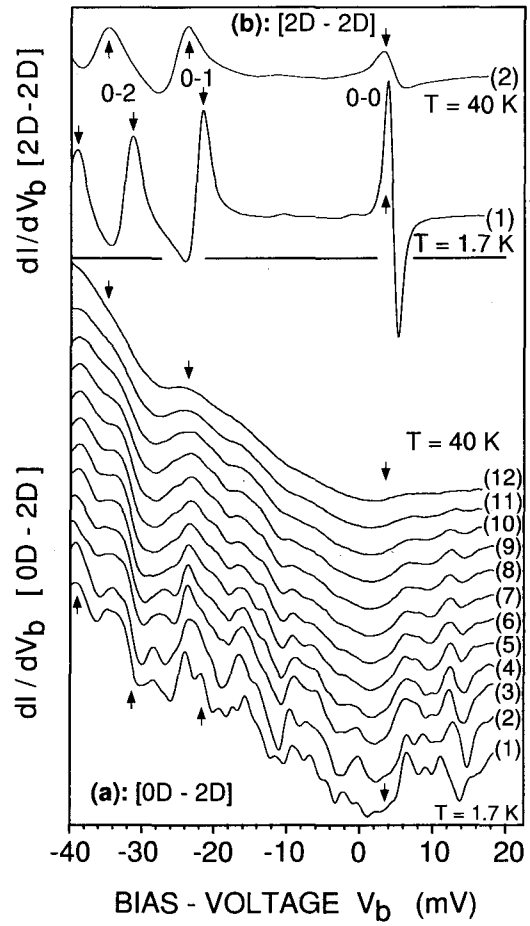

Fig. 70. (a) Measured dI/dV_b curves in the temperature range between 1.7 and 40 K. (b) For comparison, dI/dV_b curves of an unstructured sample are also shown. The corresponding temperatures are 1.7 K (curve 1), 4.2 K (2), 6.5 K (3), 9.5 K (4), 11.7 K (5), 13.9 K (6), 15.7 K (7), 18.5 K (8), 22.7 K (9), 29.0 K (10), 35.5 K (11), and 40 K (12). (Source: Reprinted with permission from [24].)

The matrix element M_{AI} [Eq. (81)], which is governed by the overlap of the single wave functions, now has the following form:

$$M_{AI} = -\frac{\hbar^2}{2m^*}\int\int_S dx\,dy\left(\Psi_I^*\frac{\partial\Psi_A}{\partial z} - \Psi_A\frac{\partial\Psi_I^*}{\partial z}\right)$$

$$= \underbrace{-\frac{\hbar^2}{2m^*}\left[\psi_{I,\nu}^*\frac{\partial\psi_A}{\partial z} - \psi_A\frac{\partial\psi_{I,\nu}^*}{\partial z}\right]_{z=z_b}}_{t_B} \times \delta_{m_I,m_A} \times \underbrace{\int d\rho\,\rho J_{m_I}(k_\parallel\rho)\varphi_{n_A,m_A}(\rho)}_{\langle J_m(k_\parallel\rho)|\varphi_{n_A,m}(\rho)\rangle} \quad (107)$$

The first term in this equation, t_B, represents the transmission coefficient of the barrier. The Kronecker symbol guarantees the conservation of the angular momentum (quantum number m) during the tunneling process. The matrix element is nonzero only if $m_I = m_A \equiv m$.

The value of the corresponding matrix element is a function of the radial quantum number n_A, the (common) azimuthal quantum number m, and the wavevector $\mathbf{k}_\parallel$ which depends on the applied bias voltage. Its value, however, is completely determined by the

requirement of total energy conservation:

$$\tilde{k}_{\parallel}(V_b) = \sqrt{\frac{2m^*}{\hbar^2}[E_{n_A,m} - E_{\nu_1} - eV_b]} \tag{108}$$

As in the case of 1D–2D tunneling, the (0D–2D) matrix element M_{AI} not only depends on the quantum numbers n_A and m and on the bias voltage V_b, but also on the particularities of the potential profile. Considering the multitude of resonant structures in the tunneling differential conductance, a strictly rectangular potential profile can be excluded, because just as in the 1D–2D case it would lead only to weak fine structure (cf. Section 6.3). As in the case of shallow etched quantum wires, one obtains a relatively realistic description of the situation by assuming a cosine-shaped radial part of the quantum dot potential profile:

$$V_{dot}(\rho) = V_{mod}\left[\frac{1}{2} + \frac{1}{2}\cos\left(\frac{\pi}{R_{dot}}(\rho - R_{dot})\right)\right] \qquad \text{with } \rho \leqslant R_{dot} \tag{109}$$

In Figure 71, the tunneling probability, calculated from this potential profile, is compared to the measured dI/dV_b at $T = 1.7$ K. The parameters of the model potential were adjusted to obtain the best possible agreement with the experimental results. Again, an energy (i.e., bias voltage) independent transmission coefficient of the tunnel barrier was assumed for this calculation. Hence, the model is, just as in the 1D–2D case, unable to reproduce the monotonic background in the experimental tunneling characteristics. It should be noted that the tunneling probability is proportional to the tunneling current, so that, to be rigorous, one has to compare the calculated curve directly with the measured tunneling current. Because the resonant structure is too weak to be observed in $I(V_b)$ directly and because a numerical derivative of the calculated results would somewhat obscure their structure, a direct comparison is not feasible in this case. Nevertheless, good agreement between the experimental results and the calculated peak positions is immediately obvious. The parameter values used in the calculation are $R_{dot} = 62.5$ nm and $V_{mod} = 38$ meV.

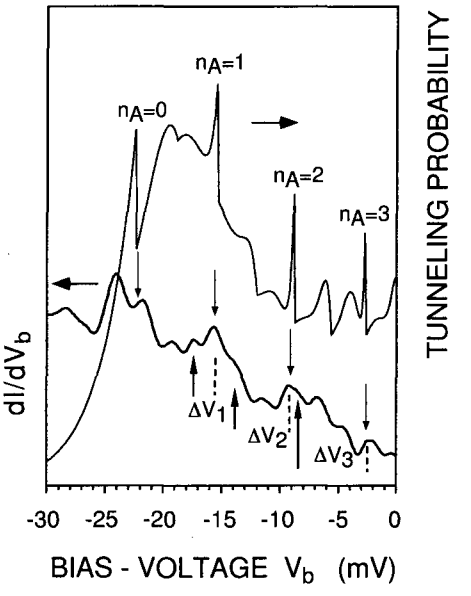

Fig. 71. Comparison between the calculated tunneling probability and the measured dI/dV_b curve at 1.7 K. The downward arrows denote the $n = 0, \ldots, 3$ resonance peaks. The upward arrows denote the peak positions where individual 0D and 2D subbands are exactly aligned. As for 1D–2D tunneling, ΔV_n denotes the distance between the resonance maximum and those positions. (Source: Reprinted with permission from [24].)

The sharp structures in the total tunneling probability are due to sharp peaks in the wave function overlap integrals for $n_A = 0, 1, 2, 3$ and can, therefore, be assigned to single peaks in the measured tunneling characteristics (denoted by downward arrows). In this way, the energy spacings of the lowest three 0D subbands in the quantum dot can be determined. If one takes into account that the relative energy shift of the 2D and 0D states is approximately equal to $e\Delta V_b$, these subband spacings are given by $\Delta E_{01} \approx 7$ meV, $\Delta E_{12} \approx 6$ meV, and $\Delta E_{23} \approx 5$ meV. ΔE_{ij} is, thus, found to decrease with increasing subband index, which is consistent with the assumption of a cosine-shaped dot potential.

Finally, it is worth noting that Coulomb charging effects will play no significant role in the discussed experiment. This is mainly due to the particular sample layout. As discussed earlier in the context of an asymmetric double-barrier tunneling device (cf. Fig. 61), Coulomb blockade effects are not observed, if the emitter barrier is less transmissive than the collector barrier. This picture is valid for *forward bias* also in the present situation, if one identifies the emitter barrier with the AlGaAs layer separating the two electron systems and the collector barrier with the broad but low barrier between the dot and the alloyed AuGe contact. Because the collector barrier is then clearly much more transmissive than the emitter barrier, Coulomb blockade is not expected for positive sample bias. For negative bias, Coulomb charging effects could, in principle, play a role. In practice, however, the sample design leads to a large capacitance between the dot and its surroundings: Each dot is capacitively coupled vertically to two large electrodes covering the whole area of the quantum dot array, namely, the underlying 2DEG and the top electrode. A rough estimate shows that this leads to an effective "capacitive" radius of the dot on the order of 150 nm. The corresponding Coulomb charging energy is far below 1 meV and, therefore, an order of magnitude smaller than the average subband spacing of the dot. This means that in the temperature range of the preceding experiments quantization effects are dominant.

Acknowledgments

The authors are grateful to G. Berthold, W. Demmerle, and F. Hirler for their substantial contribution to the scientific part of this work and N. Reinacher for solving the numerical problems. The excellent samples used in our experiments were grown by G. Böhm, W. Schlapp, G. Strasser, and G. Weimann. Valuable technical help during the sample preparation process was provided by C. Eder, C. Gmachl, M. Hauser, R. Maschek, and V. Rosskopf. The authors also acknowledge numerous fruitful discussions with W. Boxleitner, C. Hamaguchi, M. Heiblum, Y. Levinson, U. Meirav, J. C. Portal, D. Schneider, F. Stern, P. Streda, and P. Vogl. Financial support was obtained through the Gesellschaft für Mikroelektronik (GMe) and the Jubiläumsfonds der Oesterreichischen Nationalbank (OENB). Finally, we wish to thank E. Gornik for his help and continuous support during the past years.

References

1. Y. Arakawa, K. Vahala, and A. Yariv, *Appl. Phys. Lett.* 45, 950 (1984).
2. Y. Arakawa, H. Sakaki, and M. Nishioka, *Oyo Buturi* 52, 852 (1983).
3. Y. W. Lai and S. DasSarma, *Phys. Rev. B* 33, 8874 (1986).
4. S. Luryi and F. Capasso, *Appl. Phys. Lett.* 47, 1347 (1985).
5. K. Tsubaki, T. Fukui, Y. Tokura, H. Saito, and N. Susa, *Electron. Lett.* 24, 1267 (1988).
6. W.-Y. Wu, N. J. Schulmann, Y. T. Hsu, and E. Uzi, *Appl. Phys. Lett.* 51, 710 (1987).
7. T. Takagahra, *Phys. Rev. B* 36, 9293 (1987).
8. L. Wolf, "Principles of Tunneling Spectroscopy." Oxford University Press, New York, 1985.
9. D. C. Tsui, in "Handbook of Semiconductors" (T. W. Moss and W. Paul, eds.), Vol. 1, p. 662. North-Holland, Amsterdam, 1982.
10. M. Boero and J. C. Inkson, *Phys. Rev. B* 50, 2479 (1994).
11. B. J. van Wees, H. van Houten, C. W. J. Beenakker, G. J. Williamson, L. P. Kouwenhoven, D. van Marel, and C. T. Foxon, *Phys. Rev. Lett.* 60, 848 (1988).

12. D. A. Wharam, T. J. Thornton, R. Newbury, M. Pepper, H. Ahmed, J. E. F. Frost, D. G. Hasko, D. C. Peacock, D. A. Ritchie, and G. A. C. Jones, *J. Phys. C* 21, L209 (1988).
13. C. W. J. Beenakker and H. van Houten, *Phys. Rev. Lett.* 60, 2406 (1988).
14. F. M. Peeters, *Phys. Rev. Lett.* 61, 589 (1988).
15. R. K. Reich, D. K. Ferry, R. O. Grondin, and G. J. Iafrate, *Phys. Lett.* 91, 28 (1982).
16. D. R. Hofstadter, *Phys. Rev. B* 14, 2239 (1976).
17. A. Lorke, J. P. Kotthaus, and K. Ploog, *Phys. Rev. B* 44, 3447 (1991).
18. K. Ensslin and P. M. Petroff, *Phys. Rev. B* 41, 12307 (1990).
19. D. Weiss, K. von Klitzing, K. Ploog, and G. Weimann, *Europhys. Lett.* 8, 179 (1989).
20. H. Fang and P. J. Stiles, *Phys. Rev. B* 41, 10171 (1990).
21. E. S. Alves, P. H. Beton, M. Henini, L. Eaves, P. Main, O. H. Hughes, G. A. Toombs, S. P. Beaumont, and C. C. W. Wilkinson, *J. Phys. C* 1, 8257 (1989).
22. B. Kardynal, C. H. W. Barnes, E. H. Linfield, D. A. Ritchie, K. M. Brown, G. A. C. Jones, and M. Pepper, in "Proceedings of NANOMES 96," Santa Fe, NM, 1996.
23. W. Demmerle, J. Smoliner, E. Gornik, G. Böhm, and G. Weimann, *Phys. Rev. B* 47, 13574 (1993).
24. J. Smoliner, W. Demmerle, E. Gornik, G. Böhm, and G. Weimann, *Semicond. Sci. Technol.* 9, 1925 (1994).
25. C. W. J. Beenakker and H. van Houten, in "Solid State Physics" (H. Ehrenreich and D. Turnbull, eds.), Vol. 44. Academic Press, New York, 1991.
26. H. van Houten, C. W. J. Benakker, and B. J. van Wees, in "Semiconductors and Semimetals" (R. K. Willardson, A. C. Beer, and E. R. Weber, eds.), Vol. 35. Academic Press, New York, 1992.
27. A. Yacoby, U. Sivan, C. P. Umbach, and J. M. Hong, *Phys. Rev. Lett.* 66, 1938 (1991).
28. A. Yacoby, M. Heiblum, H. Shtriktman, V. Umansky, and D. Mahalu, *Semicond. Sci. Technol.* 9, 907 (1994).
29. R. Schuster, E. Buks, M. Heiblum, D. Mahalu, V. Uhansky, and H. Shtrikman, *Nature* 385, 417 (1997).
30. A. Yacoby, M. Heiblum, D. Mahalu, and H. Shtriktman, *Phys. Rev. Lett.* 74, 4047 (1995).
31. L. Pfeiffer, H. L. Stormer, K. W. Baldwin, K. W. West, A. R. Goni, A. Pinczuk, R. C. Ashoori, M. M. Dignam, and W. J. Wegscheider, *J. Cryst. Growth* 127, 849 (1993).
32. W. Wegscheider, G. Schedelbeck, G. Abstreiter, M. Rother, and M. Bichler, *Phys. Rev. Lett.* 79, 1917 (1997).
33. A. Yacoby, H. L. Stormer, K. W. Baldwin, L. N. Pfeiffer, and K. W. West, *Solid State Commun.* 101, 77 (1997).
34. T. Honda, S. Tarucha, T. Saku, and Y. Tokura, *Jpn. J. Appl. Phys.* 34, L72 (1995).
35. A. Yacobi, H. L. Stormer, N. S. Wingreen, L. N. Pfeiffer, K. W. Baldwin, and K. W. West, *Phys. Rev. Lett.* 77, 4612 (1996).
36. S. Tarucha, T. Honda, and T. Saku, *Solid State Commun.* 94, 413 (1995).
37. K. J. Thomas, M. Y. Simmons, J. T. Nicholls, D. R. Mace, M. Pepper, and D. A. Ritchie, *Appl. Phys. Lett.* 67, 109 (1995).
38. A. Gold and L. Calmels, *Philos. Mag. Lett.* 74, 33 (1966).
39. K. J. Thomas, J. T. Nicholls, M. Y. Simmons, M. Pepper, D. R. Mace, and D. A. Ritchie, *Phys. Rev. Lett.* 77, 135 (1996).
40. M. J. Kelly, "Low Dimensional Semiconductors." Clarendon Press, Oxford, U.K., 1995.
41. D. K. Ferry et al., eds., "NATO ASI Series B," Vol. 342. Plenum, New York, 1995.
42. R. D. Woods and D. S. Saxon, *Phys. Rev. B* 95, 577 (1954).
43. C. W. J. Beenakker, H. van Houten, and B. J. van Wees, *Superlattices Microstruct.* 5, 127 (1989).
44. S. E. Laux, D. J. Frank, and F. Stern, *Surf. Sci.* 196, 101 (1988).
45. S. E. Laux and A. C. Warren, in "Proceedings of the 1986 Int. Electron. Dev. Meeting," 1986, p. 576.
46. S. E. Laux and F. Stern, *Appl. Phys. Lett.* 49, 91 (1986).
47. S. E. Laux, in "Proceedings of NASECODE V Conference" (J. J. H. Miller, ed.), p. 270. Boole Press, 1987.
48. A. C. Warren and A. D. Antoniadis, *IEEE Electron Device Lett.* 7, 413 (1986).
49. J. H. Davies, *Semicond. Sci. Technol.* 3, 995 (1988).
50. T. Kerkhoven, A. T. Galick, and Y. Saad, *J. Appl. Phys.* 68, 3461 (1990).
51. B. S. Garbow, J. M. Boyle, J. J. Dongara, and B. B. Moler, *Lecture Notes Comput. Sci.* 51 (1977).
52. J. H. Luscombe, *Nanotechnology* 4, 1 (1993).
53. J. H. Luscombe and W. R. Frensley, *Nanotechnology* 1, 131 (1990).
54. J. H. Luscombe and A. M. Bouchard, *Phys. Rev. B* 46, 10262 (1992).
55. J. H. Luscombe, in "Proceedings of the International Symposium on Nanostructures and Mesoscopic Systems, Santa Fe, 1991" (W. P. Kirk and M. A. Reed, eds.), p. 357. Academic Press, Boston, 1992.
56. J. H. Luscombe, J. N. Randall, and A. M. Bouchard, *Proc. IEEE* 79, 1117 (1991).
57. A. M. Bouchard, J. H. Luscombe, A. C. Seabaugh, and J. N. Randall, in "Nanostructured and Mesoscopic Systems" (W. P. Kirk and M. Reed, eds.), p. 393. Academic Press, New York, 1992.
58. J. H. Luscombe and M. Luban, *Appl. Phys. Lett.* 57, 61 (1990).
59. J. M. Bigelow and J. P. Leburton, *J. Appl. Phys.* 76, 2887 (1994).
60. D. Jovanovic and J. P. Leburton, *Phys. Rev. B* 49, 7474 (1994).
61. J. Smoliner, G. Berthold, F. Hirler, and N. Reinacher, *Semicond. Sci. Technol.* 6, 642 (1991).
62. W. H. Press, B. P. Flannery, S. A. Teukolsky, and W. T. Vettering, "Numerical Recipes." Cambridge University Press, Cambridge, U.K., 1986.

63. D. D. Johnson, *Phys. Rev. B* 38, 12807 (1988).
64. G. P. Srivastava, *J. Phys. A: Math. Gen.* 17, L317 (1984).
65. M. Luban, J. H. Luscombe, M. A. Reed, and D. L. Pursey, *Appl. Phys. Lett.* 54, 1997 (1989).
66. A. Kumar, S. E. Laux, and F. Stern, *Phys. Rev. B* 42, 5166 (1990).
67. S. Udipi, D. Vasileska, and D. K. Ferry, *Superlattices Microstruct.* 20, 3 (1996).
68. A. Scholze, A. Wettstein, A. Schenk, and W. Fichtner, in "Proceedings of IWCE-5," Notre Dame, IN, 1996.
69. G. Klimek, R. Lake, R. C. Bowen, W. R. Frensley, and T. S. Moise, *Appl. Phys. Lett.* 76, 2539 (1995).
70. W. R. Frensley, *Rev. Mod. Phys.* 62, 745 (1990).
71. M. Luban and J. H. Luscombe, *Phys. Rev. B* 35, 9045 (1987).
72. M. Reed, in "Semiconductors and Semimetals" (R. K. Willardson, A. C. Beer, and E. R. Weber, eds.), Vol. 35. Academic Press, New York, 1992.
73. S. Datta, in "Cambridge Studies in Semiconductor Physics and Microelectronic Engineering" (H. Ahmed, M. Pepper, and A. Broers, eds.), Vol. 3. Cambridge University Press, 1995.
74. K. F. Berggren, T. J. Thornton, D. J. Newson, and M. Pepper, *Phys. Rev. Lett.* 57, 1769 (1986).
75. K. F. Berggren, G. Roos, and H. van Houten, *Phys. Rev. B* 37, 10118 (1988).
76. K. F. Berggren and D. J. Newson, *Semicond. Sci. Technol.* 1, 327 (1986).
77. A. A. Abrikosov, "Fundamentals of the Theory of Metals." North-Holland, Amsterdam, 1988.
78. F. Hirler, J. Smoliner, E. Gornik, G. Weimann, and W. Schlapp, *Appl. Phys. Lett.* 57, 16 (1990).
79. F. Brinkop, W. Hansen, J. P. Kotthaus, and K. Ploog, *Phys. Rev. B* 37, 6517 (1988).
80. V. Gudmundsson, A. Brataas, P. Grambow, B. Meurer, T. Kurth, and D. Heitmann, *Phys. Rev. B* 51, 17744 (1995).
81. H. J. Rundquist, *Semicond. Sci. Technol.* 4, 455 (1989).
82. T. J. Thornton, M. L. Roukes, A. Scherer, and P. P. Van de Gaag, *Phys. Rev. Lett.* 63, 2128 (1989).
83. H. Akera and T. Ando, in "Proceedings of the 20th International Conference on the Physics of Semiconductors" (E. M. Anastassakis and J. D. Joannopoulos, eds.), Vol. 3. World Scientific, Singapore, 1990.
84. W. Hansen, "Semiconductors and Semimetals" (R. K. Willardson, A. C. Beer, and E. R. Weber, eds.), Vol. 35. Academic Press, New York, 1992.
85. Y. Imry, in "Directions of Condensed Matter Physics" (G. Grinstein and G. Mazenko, eds.), Vol. 2. World Scientific, Singapore, 1986.
86. G. Bergmann, *Phys. Rev. B* 2, 2914 (1983).
87. S. Chakravarty and A. Schmid, *Phys. Rep.* 140, 193 (1986).
88. B. L. Altshuler and A. G. Aronov, *Pis'ma Zh. Eksp. Teor. Fiz.* 33, 499 (1981).
89. C. W. J. Beenakker and H. van Houten, *Phys. Rev. B* 38, 6544 (1988).
90. C. W. J. Beenakker and H. van Houten, *Phys. Rev. B* 38, 3232 (1988).
91. T. J. Thornton, M. Pepper, H. Ahmed, D. Andrews, and G. J. Davies, *Phys. Rev. Lett.* 56, 1198 (1986).
92. H. van Houten, C. W. J. Beenakker, B. J. van Wees, and J. E. Mooij, *Surf. Sci.* 196, 144 (1988).
93. B. L. Altshuler and A. G. Aronov, in "Electron–Electron Interactions in Disordered Systems" (A. L. Efros and M. Pollak, eds.). North-Holland, Amsterdam, 1985.
94. H. van Houten, B. J. van Wees, M. G. J. Heijman, and J. P. André, *Appl. Phys. Lett.* 49, 1781 (1986).
95. V. L. Gurevich and Y. A. Firsov, *Zh. Eksp. Teor. Fiz.* 40, 198 (1961) [*Sov. Phys. JETP* 13, 137 (1961)].
96. R. L. Peterson, in "Semiconductors and Semimetals" (R. K. Willardson and A. C. Beer, eds.), Vol. 10, p. 221. Academic Press, New York, 1975.
97. R. A. Stradling and R. A. Wood, *Solid State Commun.* 6, 701 (1968).
98. P. G. Harper, J. W. Hodby, and R. A. Stradling, *Rep. Prog. Phys.* 37, 1 (1973).
99. D. Schneider, D. Rürup, B. Schönfelder, and A. Schlachetzki, *Z. Phys. B* 100, 33 (1996).
100. D. Schneider, K. Fricke, J. Schulz, G. Irmer, and M. Wenzel, in "Proceedings of the 23rd International Conference on the Physics of Semiconductors" (M. Scheffler and R. Zimmermann, eds.), Vol. 1, p. 221. World Scientific, Singapore, 1996.
101. D. C. Tsui, T. Englert, A. Y. Cho, and A. C. Gossard, *Phys. Rev. Lett.* 44, 341 (1980).
102. M. A. Brummell, R. J. Nicholas, M. A. Hopkins, J. J. Harris, and C. T. Foxon, *Phys. Rev. Lett.* 58, 77 (1987).
103. M. A. Brummell, D. R. Leadley, R. J. Nicholas, J. J. Harris, and C. T. Foxon, *Surf. Sci.* 196, 451 (1988).
104. D. R. Leadley, R. J. Nicholas, J. Singleton, W. Xu, F. M. Peeters, J. T. Devreese, J. A. Perenboom, L. van Bockstal, F. Herlach, J. J. Harris, and C. T. Foxon, *Phys. Rev. Lett.* 73, 589 (1994).
105. P. Vasilopoulos, P. Warmenbol, F. M. Peeters, and J. T. Devreese, *Phys. Rev. B* 40, 1810 (1989).
106. P. Vasilopoulos, *Phys. Rev. B* 33, 8587 (1986).
107. J. R. Barker, *J. Phys. C* 5, 1657 (1972).
108. N. Mori, H. Murata, K. Taniguchi, and C. Hamaguchi, *Phys. Rev. B* 38, 7622 (1988).
109. N. Mori, H. Momose, and C. Hamaguchi, *Phys. Rev. B* 45, 4536 (1992).
110. J. Y. Ryu and R. F. O'Connell, *Phys. Rev. B* 48, 9126 (1993).
111. J. Y. Ryu and R. F. O'Connell, *Phys. Rev. B* 49, 10437 (1994).
112. J. Y. Ryu and S. D. Choi, *Phys. Rev. B* 44, 11328 (1991).

113. G. Ploner, J. Smoliner, G. Strasser, and E. Gornik, in "Proceedings of the 23rd International Conference on Physics of Semiconductors" (M. Scheffler and R. Zimmermann, eds.), Vol. 2, p. 1245. World Scientific, Singapore, 1996.

114. G. Ploner, J. Smoliner, G. Strasser, and E. Gornik, *Superlattices Microstruct.* 22, 249 (1997).

115. G. Ploner, J. Smoliner, G. Strasser, M. Hauser, and E. Gornik, *Phys. Rev. B* 57, 3966 (1998); G. Ploner, PhD thesis, Tu Vienna (1998).

116. G. Berthold, J. Smoliner, C. Wirner, E. Gornik, G. Böhm, G. Weimann, M. Hauser, C. Hamaguchi, N. Mori, and H. Momose, *Semicond. Sci. Technol.* 8, 735 (1993).

117. C. W. J. Beenakker, *Phys. Rev. Lett.* 62, 2020 (1989).

118. R. R. Gerhardts, D. Weiss, and K. von Klitzing, *Phys. Rev. Lett.* 62, 1173 (1989).

119. R. W. Winkler, J. P. Kotthaus, and K. Ploog, *Phys. Rev. Lett.* 62, 1177(1989).

120. P. Vasilopoulos and F. M. Peeters, *Phys. Rev. Lett.* 63, 2120 (1989).

121. P. H. Beton, E. S. Alves, P. C. Main, L. Eaves, M. W. Dellow, M. Henini, and O. H. Hughes, *Phys. Rev. Lett.* 42, 9229 (1990).

122. P. H. Beton, M. W. Dellow, P. C. Main, E. S. Alves, L. Eaves, S. P. Beaumont, and C. D. Wilkinson, *Phys. Rev. B* 43, 9980 (1991).

123. J. Kucera, P. Streda, and R. R. Gerhardts, *Phys. Rev. B* 55, 14439 (1997).

124. P. Streda and J. Kucera, *Superlattices Microstruct.* 22 (1997).

125. P. Streda and A. H. MacDonald, *Phys. Rev. B* 41, 11892 (1990).

126. A. Soibel, U. Meirav, D. Mahalu, and H. Shtriktman, *Phys. Rev. B* 55, 4482 (1997).

127. Y. Paltiel, D. Mahalu, H. Shtriktman, G. Bunin, and U. Meirav, *Semicond. Sci. Technol.* 12, 987 (1997).

128. J. H. Davies and I. A. Larkin, *Phys. Rev. B* 49, 4800 (1994).

129. G. Müller, P. Streda, D. Weiss, K. von Klitzing, and G. Weimann, *Phys. Rev. B* 50, 8938 (1994).

130. C. C. Eugster and J. A. del Alamo, *Phys. Rev. Lett.* 67, 3586 (1991).

131. C. C. Eugster, J. A. del Alamo, M. R. Melloch, and M. J. Rooks, *Phys. Rev. B* 48, 15057 (1993).

132. S. Luryi and F. Capasso, *Appl. Phys. Lett.* 47, 1347 (1985).

133. A. Zaslavsky, D. C. Tsui, M. Santos, and M. Shayegan, *Appl. Phys. Lett.* 58, 1440 (1991).

134. M. M. Dignam, R. C. Ashoori, H. L. Stoermer, L. N. Pfeiffer, K. L. Baldwin, and K. W. West, *Phys. Rev. B* 49, 3369 (1994).

135. S. Tarucha, Y. Hirayama, T. Saku, and T. Kimura, *Phys. Rev. B* 41, 5459 (1990).

136. S. Tarucha, Y. Hirayama, and Y. Tokura, *Appl. Phys. Lett.* 58, 1623 (1991).

137. G. W. Bryant, *Phys. Rev. B* 39, 3145 (1989).

138. G. W. Bryant, *Phys. Rev. B* 44, 3782 (1991).

139. J. Smoliner, E. Gornik, and G. Weimann, *Appl. Phys. Lett.* 52, 2136 (1988).

140. J. Smoliner, F. Hirler, E. Gornik, G. Weimann, M. Hauser, and W. Schlapp, *Semicond. Sci. Technol.* 6, 389 (1991).

141. J. Smoliner, W. Demmerle, G. Berthold, E. Gornik, G. Weimann, and W. Schlapp, *Phys. Rev. Lett.* 63, 2116 (1989).

142. W. Demmerle, J. Smoliner, G. Berthold, G. Weimann, and W. Schlapp, *Phys. Rev. B* 44, 3090 (1991).

143. L. Wang, P. H. Beton, N. Mori, L. Eaves, H. Buhmann, L. Mansouri, P. C. Main, T. J. Foster, and M. Henini, *Phys. Rev. Lett.* 73, 1146 (1994).

144. P. H. Beton, J. Wang, N. Mori, L. Eaves, P. C. Main, T. J. Foster, and M. Henini, *Phys. Rev. Lett.* 75, 1996 (1995).

145. N. Mori, P. H. Beton, J. Wang, and L. Eaves, *Phys. Rev. B* 51, 1735 (1995).

146. N. Mori, P. H. Beton, J. Wang, and L. Eaves, *Phys. Rev. B* 52, 1505 (1995).

147. B. Kardynal, E. H. Linfield, D. A. Ritchie, K. M. Brown, C. H. W. Barnes, G. A. C. Jones, and M. Pepper, *Appl. Phys. Lett.* 68, 826 (1996).

148. B. Kardynal, C. H. W. Barnes, E. H. Linfield, D. A. Ritchie, K. M. Brown, G. A. C. Jones, and M. Pepper, *Phys. Rev. Lett.* 76, 3802 (1996).

149. B. Kardynal, C. H. W. Barnes, E. H. Linfield, D. A. Ritchie, T. J. Nicholls, K. M. Brown, G. A. C. Jones, and M. Pepper, *Phys. Rev. B* 55, R1966 (1997).

150. J. P. Eisenstein, L. N. Pfeiffer, and K. W. West, *Phys. Rev. Lett.* 69, 3804 (1992).

151. J. P. Eisenstein, L. N. Pfeiffer, and K. W. West, *Surf. Sci.* 305, 393 (1994).

152. K. M. Brown, N. Turner, J. T. Nicholls, E. H. Linfield, M. Pepper, D. A. Ritchie, and G. A. C. Jones, *Phys. Rev. B* 50, 15465 (1994).

153. J. R. Oppenheimer, *Phys. Rev.* 13, 66 (1928).

154. J. Bardeen, *Phys. Rev. Lett.* 6, 57 (1961).

155. W. A. Harrison, *Phys. Rev.* 123, 85 (1961).

156. J. Smoliner, W. Demmerle, F. Hirler, E. Gornik, G. Weimann, M. Hauser, and W. Schlapp, *Phys. Rev. B* 43, 7358 (1991).

157. J. Wang, P. H. Beton, N. Mori, H. Buhmann, L. Mansouri, L. Eaves, P. C. Main, T. J. Foster, and M. Henini, *Appl. Phys. Lett.* 65, 1124 (1994).

158. G. D. Mahan, "Many Particle Physics," 2nd ed. Plenum Press, New York, 1990.

159. L. Zheng and A. H. MacDonald, *Phys. Rev. B* 47, 13547 (1993).

160. H. Grabert and M. Devoret, eds., "Single Charge Tunneling." Plenum Press, New York, 1991.
161. U. Meirav and E. B. Foxman, *Semicond. Sci. Technol.* 10, 255 (1996).
162. L. P. Kouwenhoven, C. M. Marcus, P. L. McEuen, S. Tarucha, R. M. Westervelt, and N. S. Wingreen, in "Mesoscopic Electron Transport" (L. L. Sohn, L. P. Kouwenhoven, and G. Schön, eds.). Kluwer Academic, Dordrecht, The Netherlands, 1997.
163. M. A. Reed, J. N. Randall, R. J. Aggarwal, R. J. Matyi, T. M. Moore, and A. E. Wetsel, *Phys. Rev. Lett.* 60, 535 (1988).
164. J. N. Randall, M. A. Reed, R. J. Matyi, and T. M. Moore, *J. Vac. Sci. Technol. B* 6, 1861 (1988).
165. J. N. Randall, M. A. Reed, and Y. C. Kao, *J. Vac. Sci. Technol. B* 8, 348 (1990).
166. K. Y. Lee, T. P. Smith III, H. Arnot, C. M. Knoedler, J. M. Hong, D. P. Kern, and S. E. Laux, *J. Vac. Sci. Technol. B* 6, 1856 (1988).
167. N. Kamata, K. Yamada, N. Miura, and L. Eaves, *J. Phys. Soc. Jpn.* 2120 (1993).
168. M. Boero and J. C. Inkson, *Phys. Rev. B* 50, 2479 (1994).
169. A. Sa'ar, J. Feng, I. Grave, and A. Yariv, *J. Appl. Phys.* 72, 3598 (1992).
170. S. Tarucha, Y. Hirayama, T. Saku, and T. Kimura, *Phys. Rev. B* 41, 5459 (1990).
171. A. Kumar, *Surf. Sci.* 263, 335 (1992).
172. D. C. Glattili, C. Pasquier, U. Meirav, F. I. B. Williams, Y. Jin, and B. Etienne, *Z. Phys. B* 85, 367 (1991).
173. L. P. Kouwenhoven, N. C. van der Maart, C. J. P. M. Harmans, and C. Foxon, *Adv. Solid State Phys.* 31, 329 (1991).
174. A. A. M. Staring, J. G. Williamson, H. van Houten, C. W. J. Beenakker, L. P. Kouwenhoven, and C. T. Foxxon, *Physica B* 175, 226 (1991).
175. T. A. Fulton and G. A. Dolan, *Phys. Rev. Lett.* 59, 109 (1987).
176. H. van Houten and C. W. J. Beenakker, *Phys. Rev. Lett.* 63, 1893 (1989).
177. C. W. J. Beenakker, *Phys. Rev. B* 44, 1646 (1991).
178. D. V. Averin and K. K. Likharev, in "Mesoscopic Phenomena in Solids" (B. L. Altshuler et al., eds.). Elsevier, Amsterdam, 1991.
179. L. G. Ingold and Y. V. Nazorov, in "Single Charge Tunneling and Coulomb Blockade Phenomena in Nanostructures" (H. Grabert and M. H. Devoret, eds.), p. 21. Plenum, New York, 1992.
180. A. T. Johnson, L. P. Kouvenhoven, W. Dejong, C. C. van der Maart, C. J. P. M. Harmans, and C. T. Foxxon, *Phys. Rev. Lett.* 69, 1592 (1992).
181. E. B. Foxman, L. P. McEuen, U. Meirav, N. S. Wingren, Y. Meir, P. A. Belk, N. R. Belk, M. A. Kastner, and S. J. Wind, *Phys. Rev. B* 47, 10020 (1993).
182. J. Weis, R. J. Haug, K. von Klitzing, and K. Ploog, *Phys. Rev. Lett.* 71, 4019 (1993).
183. R. C. Ashoori, H. L. Stormer, J. S. Weiner, L. N. Pfeiffer, S. J. Pearton, K. W. Baldwin, and K. W. West, *Phys. Rev. Lett.* 68, 3088 (1992).
184. R. C. Ashoori, H. L. Stormer, J. S. Weiner, L. N. Pfeiffer, S. J. Pearton, K. W. Baldwin, and K. W. West, *Phys. Rev. Lett.* 62, 2168 (1989).
185. R. H. Blick, T. Schmidt, R. Haug, and K. von Klitzing, *Semicond. Sci. Technol.* 11, 1506 (1996).
186. Y. G. Gobato, J. M. Berroir, and Y. Gouldner, *Solid State Commun.* 87, 513 (1993).
187. M. Tewordt, L. Martin-Moreno, T. J. Nicholls, M. Pepper, M. J. Kelly, V. J. Law, D. A. Ritchie, J. E. F. Frost, and G. A. C. Jones, *Phys. Rev. B* 46, 3948 (1992).
188. J. W. Sleight, E. S. Hornbeck, M. R. Desphande, R. G. Wheeler, M. A. Reed, R. C. Bowen, W. R. Frensley, J. N. Randall, and R. J. Matyi, *Phys. Rev. B* 53, 15727 (1996).
189. Z.-L. Ji, *Phys. Rev. B* 50, 4658 (1994).
190. H. C. Liu and G. C. Aers, *Solid State Commun.* 67, 1131 (1988).
191. S. Y. Chou, E. Wolak, and J. S. Harris, *Appl. Phys. Lett.* 52, 657 (1988).
192. B. Su, V. J. Goldmann, and J. E. Cunningham, *Phys. Rev. B* 46, 7644 (1992).
193. T. Schmidt, M. Tewordt, R. H. Blick, R. J. Haug, D. Pfannkuche, K. von Klitzing, A. Foster, and A. Luth, *Phys. Rev. B* 51, 5570 (1995).
194. M. Tewordt, L. M. Moreno, J. T. Nicholls, M. Pepper, M. J. Kelly, V. Law, D. A. Ritchie, J. E. F. Frost, and G. A. C. Jones, *Phys. Rev. B* 45, 14407 (1992); M. J. Kelly, V. Law, D. A. Ritchie, J. E. F. Frost, and G. A. C. Jones, *Phys. Rev. B* 45, 14407 (1992).
195. T. Schmidt, R. J. Haug, K. von Klitzing, A. Föster, and H. Lüth, *Phys. Rev. B* 55, 2230 (1997).
196. K. Nomoto, T. Suzuki, K. Taira, and K. Hase, *Phys. Rev. B* 55, 2523 (1997).
197. M. Tewordt, R. J. F. Hughes, L. Martin-Moreno, T. J. Nicholls, H. Asahi, M. J. Kelly, V. J. Law, D. A. Ritchie, J. E. F. Frost, G. A. C. Jones, and M. Pepper, *Phys. Rev. B* 49, 8071 (1994).
198. A. K. Geim, T. J. Foster, A. Nogaret, N. Mori, P. J. McDonnel, N. La Scala, P. C. Main, and L. Eaves, *Phys. Rev. B* 50, 8074 (1994).
199. J. W. Sakai, P. C. Main, P. H. Beton, N. La Scala Jr., A. K. Geim, L. Eaves, and H. Henini, *Appl. Phys. Lett.* 64, 2563 (1994).
200. P. H. Beton, H. Buhmann, L. Eaves, T. J. Foster, A. K. Geim, N. La Scala Jr., P. C. Main, L. Mansouri, N. Mori, J. W. Sakai, and J. Wang, *Semicond. Sci. Technol.* 9, 1912 (1994).
201. W. B. Kinard, M. H. Weichold, G. F. Spencer, and W. P. Kirk, *J. Vac. Sci. Technol. B* 8, 393 (1991).
202. L. Eaves, in "Physics of Nanostructures" (J. H. Davies and A. R. Long, eds.), p. 149. IOP Publishing, 1992.

203. P. C. Main, P. H. Beton, M. W. Dellow, L. Eaves, T. J. Foster C. J. G. M. Langerak, M. Henini, and J. W. Sakai, *Physica B* 189, 125 (1993).
204. M. W. Dellow, P. H. Beton, M. Henini, P. C. Main, L. Eaves, S. P. Beaumont, and C. D. W. Wilkinson, *Electron. Lett.* 27, 134 (1991).
205. N. Blanc, P. Gueret, R. Germann, and H. Rothuizen, *Physica B* 189, 135 (1993).
206. J. Smoliner, *Semicond. Sci. Technol.* 11, 1 (1996).